ARMY RESEARCH LABORATORY

ARL

Volume I: Select Papers

ARL Summer Student Research Symposium

NOTICES

Disclaimers

The findings in this report are not to be construed as an official Department of the Army position unless so designated by other authorized documents.

Citation of manufacturer's or trade names does not constitute an official endorsement or approval of the use thereof.

Destroy this report when it is no longer needed. Do not return it to the originator.

Army Research Laboratory

Adelphi, MD 20783-1197

Volume I: Select Papers

ARL Summer Student Research Symposium

REPORT DOCUMENTATION PAGE

1. REPORT DATE *(DD-MM-YYYY)*	2. REPORT TYPE	3. DATES COVERED (From - To)
August 2012	Final	

4. TITLE AND SUBTITLE	5a. CONTRACT NUMBER
Volume I: Select Papers	
	5b. GRANT NUMBER
	5c. PROGRAM ELEMENT NUMBER

6. AUTHOR(S)	5d. PROJECT NUMBER
ARL Summer Student Research Symposium	
	5e. TASK NUMBER
	5f. WORK UNIT NUMBER

7. PERFORMING ORGANIZATION NAME(S) AND ADDRESS(ES)	8. PERFORMING ORGANIZATION REPORT NUMBER
U.S. Army Research Laboratory 2800 Powder Mill Road Adelphi, MD 20783-1197	ARL-TM-2012

9. SPONSORING/MONITORING AGENCY NAME(S) AND ADDRESS(ES)	10. SPONSOR/MONITOR'S ACRONYM(S)
	11. SPONSOR/MONITOR'S REPORT NUMBER(S)

12. DISTRIBUTION/AVAILABILITY STATEMENT

Approved for public release; distribution unlimited.

13. SUPPLEMENTARY NOTES

14. ABSTRACT

The ARL Summer Student Research Symposium is an ARL Director's Award Program for all the students participating in various summer scholarship and contract activities across ARL. The goal of the program is to recognize and publicize exceptional achievements made by the students and their mentors in the support of Army science.

All college undergraduate and graduate students receiving research appointments and conducting summer studies at ARL are automatically enrolled in the symposium program. As an integral part of their summer study, all students are required to write a paper on their work which summarizes their major activity and its end product.

The program is conducted on two separate competitive levels: undergraduate and graduate. The format of the paper in both levels is the same. However, the evaluation will take into consideration the difference in the academic level of the students.

All students submitted their research paper for directorate review. Directorate judging panels selected one or two papers from each competition category for the laboratory-wide competition at the Summer Student Symposium on 9 August 2012.

Students selected by their directorate for competition participated in the one-day Summer Student Symposium on 9 August 2012. At the symposium the students presented their papers to the ARL Director and an ARL Fellows panel.

This volume of the Summer Student Symposium Proceedings contains the papers presented at the symposium.

15. SUBJECT TERMS

16. SECURITY CLASSIFICATION OF:			17. LIMITATION OF ABSTRACT	18. NUMBER OF PAGES	19a. NAME OF RESPONSIBLE PERSON
a. REPORT	b. ABSTRACT	c. THIS PAGE	UU	210	Vallen Emery
Unclassified	Unclassified	Unclassified			19b. TELEPHONE NUMBER *(Include area code)* (301) 394-3585

Contents

INTENTIONALLY LEFT BLANK.

Director's Foreword

The U.S. Army Research Laboratory (ARL) mission is to "Provide innovative science, technology, and analyses to enable full spectrum operations." As the Army's corporate laboratory, we provide the technological underpinnings critical to providing capabilities required by our current and future Soldiers.

Our nation is projected to experience a shortage of scientists and engineers. ARL recognizes the criticality of intellectual capital in generating capabilities for the Army. As the Army's corporate laboratory, addressing the projected shortfall is a key responsibility for us. We have, therefore, identified the nation's next generation of scientists and engineers as a key community of interest and have generated a robust educational outreach program to strengthen and support them. We have achieved many successes with this community. We believe that the breadth and depth of our outreach programs will have a significant positive effect on the participants, facilitating their journey toward becoming this Nation's next generation of scientists and engineers.

A fundamental component of our outreach program is to provide students research experiences at ARL. During the summer of 2012, we supported research experiences at ARL for over 175 undergraduate and graduate students. Each of these students writes a paper describing the results of the work they performed while at ARL. All of the papers were of high quality, but only a few could be presented at our student symposium. The abstracts for all papers prepared this summer are contained in this volume of the proceedings and they indicate that there were many excellent research projects with outstanding results. It is unfortunate that there was not enough time for us to have all of the papers presented. We would have enjoyed hearing them all.

We are very pleased to have hosted this outstanding group of students for the summer. It is our hope that they will continue their pursuit of technical degrees and will someday assist us in providing critical technologies for our Soldiers.

JOHN PELLEGRINO
Director (A)

INTENTIONALLY LEFT BLANK.

Introduction

The ARL Summer Student Research Symposium is an ARL Director's Award Program for all the students participating in various summer scholarship and contract activities across ARL. The goal of the program is to recognize and publicize exceptional achievements made by the students and their mentors in the support of Army science.

All college undergraduate and graduate students receiving research appointments and conducting summer studies at ARL are automatically enrolled in the symposium program. As an integral part of their summer study, all students are expected to write a paper on their work which summarizes their major activity and its end product.

The program is conducted on two separate competitive levels: undergraduate and graduate. The format of the paper in both levels is the same. However, the evaluation will take into consideration the difference in the academic level of the students.

All students submitted their research paper for directorate review. Directorate judging panels selected one or two papers from each competition category for the laboratory-wide competition at the Summer Student Symposium on 9 August 2012.

Students selected by their directorate for competition participated in the one-day Summer Student Symposium on 9 August 2012. At the symposium, the students presented their papers to an audience of ARL scientists and engineers, including the ARL Director and an ARL Fellows panel.

This volume of the Summer Student Symposium Proceedings contains the papers presented at the symposium.

INTENTIONALLY LEFT BLANK.

Computational & Information Sciences Directorate (CISD)

INTENTIONALLY LEFT BLANK.

U.S. Army Research Laboratory
SUMMER RESEARCH TECHNICAL REPORT

BlueHoc: Distributed Computing Over Bluetooth Ad-hoc Networks on Android-Based Mobile Devices

GREGORIO HIRAM HINOJOS
MENTOR: DAVID BRUNO
COMPUTATIONAL INFORMATION AND SCIENCES DIRECTORATE
ABERDEEN PROVING GROUND, MARYLAND

Contents

List of Figures

List of Tables

Abstract

The high demand and utility of mobile devices have necessitated advances in mobile technology. Researchers are trying to utilize the numerous mobile devices, which are readily available to solve parallelizable problems. This paper introduces BlueHoc, which allows distributed computing across mobile devices. BlueHoc enables Android-based mobile devices to form a Bluetooth ad-hoc network that can potentially behave as an HPC cluster. The architecture of BlueHoc is master-slave based, where the master can be connected with up to seven slaves. In addition, the architecture also allows for slaves to connect with up to six other devices, which enables them to form a limited ad-hoc network. Because the Android OS deviates from the Linux kernel and does not have full support for GNU libraries, we are not allowed to port existing Linux applications or libraries. This increases the complexity of our system to be used for complex computations. The experimental results of our system are based on the computation of a PI estimation algorithm, which is used to exploit the parallelism of our system.

Acknowledgments

Apart from my efforts, the success of any project depends largely on the encouragement and guidance of others. I take this opportunity to express my sincere gratitude to the people who have been influential to the successful completion of this research project. I would like to thank my mentors, Mr. David Bruno, Mr. Dale Shires, and Mr. Kenneth Renard. Without their encouragement and guidance, this project would not have been materialized. I would like to thank Mr. John Vines, Mr. Jordan Ruloff, and Curtis Tade for their help in this project. Finally, I am endlessly indebted to my wife and daughter for their understanding, encouragement, endless support, and patience when it was most required.

Student Bio

I'm currently a second-year graduate student at New Mexico State University, pursuing a master's degree in Electrical Engineering with a specialization in digital signal processing. My current research involves speaker diarization, where the objective is to segment an audio stream into homogenous segments where only one speaker is active and at the same time classify or label the speaker. In May 2011, I graduated with a dual degree in Electrical Engineering and Computer Science from New Mexico State University. Last summer I attended the Army High-Performance Computing Research Center (AHPCRC) Summer Institute at Stanford University. My research project involved wireless ad-hoc networks using the NS2 network simulator. I implemented different mobility models to reflect real-life scenarios and worked on parallelizing the simulations to decrease simulation time. My plans for the future are to pursue a career in research and development.

1. Introduction/Background

The synchronized use of the computing power from many machines for distributed computing has been highly researched over the past few years. This area of research has focused on using multiple autonomous computers communicating through a wired network. This project introduces a system that enables distributed computation across mobile devices communicating wirelessly via Bluetooth.

Mobile devices are perhaps the most pervasive computing devices available today. The high demand and utility of mobile devices have necessitated advances in mobile technology. The vast number of available devices presents significant computational resources that can be used to solve many parallelizable computations. Mobile device resources can be combined and leveraged to create a distributed infrastructure that is able to perform parallel computing from both mobile Soldiers and stationary operators in a tactical operations center (TOC).

The purpose of this project is to design a system that will utilize unused resources from mobile devices to perform parallel computations. This project aims to answer the important questions, "What computing capacity can I achieve from many Army connected devices?" and "What new capabilities can they bring to the Army operational domain?" It is not always feasible to build a High-Performance Computing (HPC) system out in the field or ensure its connectivity at all times. This project attempts to bring HPC closer to the Soldiers and makes it possible to build a HPC system from resources that are available and underutilized.

Bluetooth technology provides for dynamically linked mobile devices that can exploit the potential of wireless networks used in parallel computing. Bluetooth provides a low-power transmission mechanism that is commonly embedded in most mobile devices nowadays. The widespread nature of Bluetooth makes it an ideal technology for building ad-hoc networks to create a multiprocessor distributed infrastructure from mobile devices. Bluetooth offers a great means of wireless communication for mobile devices, and it is a low-power consumption protocol compared with other wireless communication protocol such as Wi-Fi. Bluetooth requires only 3% of the power required by Wi-Fi to perform the same task.

The target platform for this project is Android. Android, the most popular mobile platform on the market, is an open-source project; 68.1% of mobile devices shipped during the second quarter of 2012 use Android as their operation system. The prevalent and sophisticated nature of Android allows for the creation of countless applications with endless possibilities. Additionally, the Army is moving toward utilizing Android as their main operating system for mobile devices.

2. Experiment/Calculations

Message Passing Interface (MPI) is the standard for parallel programming on multiprocessor distributed systems. However, because Android deviates from the Linux kernel, Android does not fully support common Linux applications and libraries; consequently, MPI was not successfully ported to Android. As a result, an alternate approach to MPI was developed using the radio frequency communication (RFCOMM) protocol embedded in Bluetooth and fully supported by Android.

BlueHoc system architecture is master-slave, where the master can connect with a maximum of seven slaves, forming a piconet (figure 1). Bluetooth only supports eight active connections in a network.
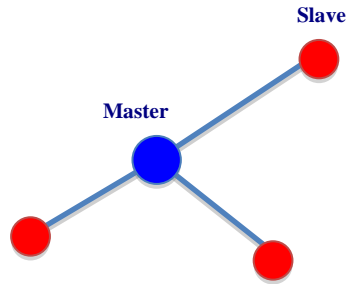

Figure 1. Piconet.

Additionally, the slaves can become secondary masters expanding the network forming a scatternet (figure 2); these devices will simultaneously play the master role in one piconet and the slave role in another.
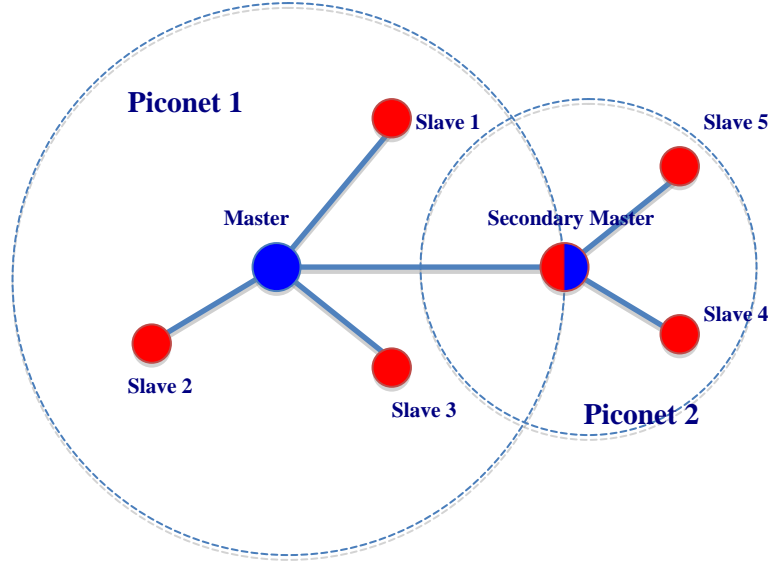
Figure 2. Scatternet.

The current architecture of BlueHoc is static, meaning that the slaves have to join the network and remain active throughout the work interval. The master waits for the slaves to join the network. After all the slaves joined, the master is able to submit job requests. The master submits job requests to the slaves by scattering the tasks among the slaves and gathering the computed results back to calculate a final result. Figure 3 illustrates the data flow of the BlueHoc system architecture.

Figure 3. BlueHoc Architecture.

3.   Results and Discussions

To investigate the metrics and results for BlueHoc, several important parameters for efficiency are applicable, such as time to solution, scalability, and whether the executed algorithm is

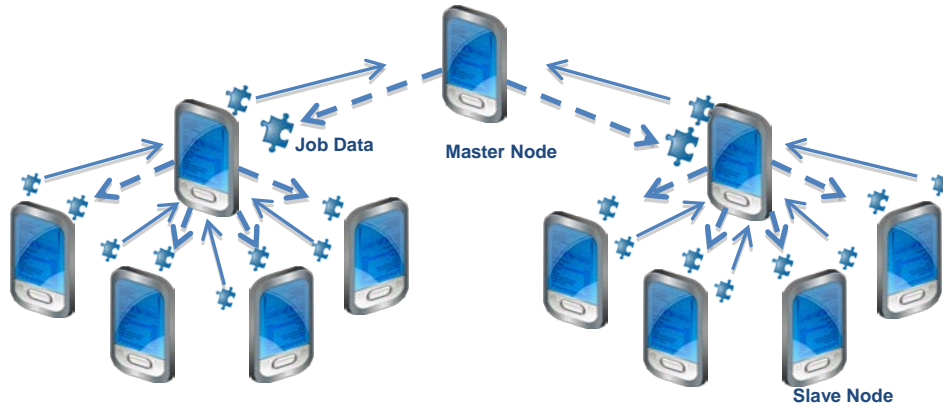computation or communication bound. However, due to the time constraints of a summer project, the initial parameters to consider are time to solution and scalability. The benchmarks presented are based on an algorithm to estimate PI in which the value of PI becomes more precise as the iteration count increases. The master divides the workload evenly and scatters it among the devices in the network. Each device computes its portion of the workload and reports the results back to the master; each device can work independently, as there are no data dependencies. Then, the master gathers the results and computes the final estimation of PI. Even though this algorithm is useless in a real-world application, it is intended to provide a high computational load and demonstrate the performance of the system.

The overall time to solution depends upon certain aspects of the system, including the speed of transmission and latency. Furthermore, having different devices with different characteristics introduces timing inefficiencies. Essentially, BlueHoc is as fast as the slowest device in the network.

Figure 4 illustrates the different execution times for different devices computing the same task. Table 1 shows the specifications for the devices used in the presented benchmarks.
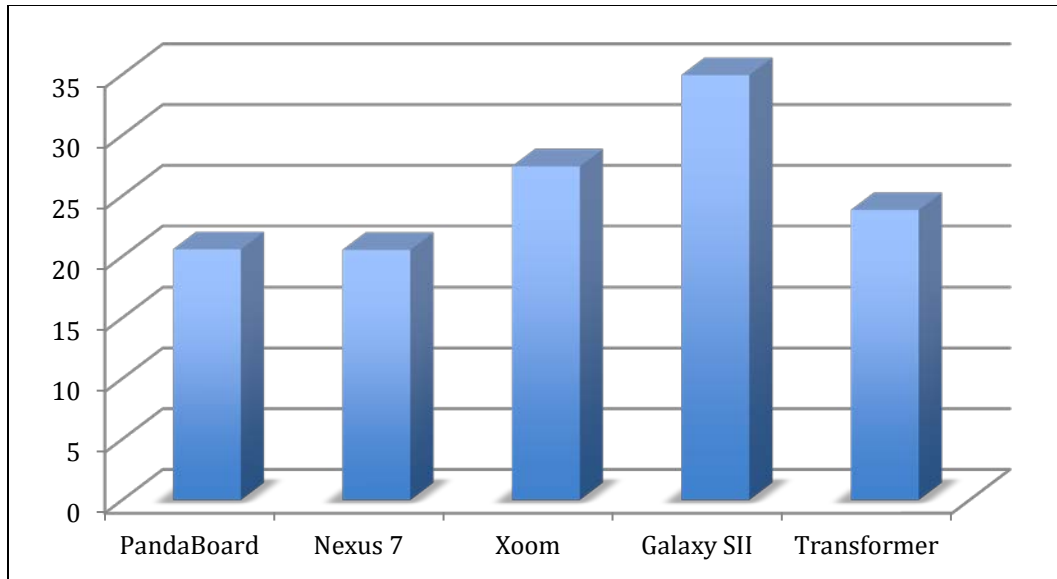
Figure 4. Execution time for different devices.

Table 1. Specification for different mobile devices.

Mobile Device	CPU
1. PandaBoard ES	Dual-core ARM Cortex-A9 @ 1.2 GHz
2. Nexus 7	Quad-core Tegra 3 @ 1.3 GHz
3. Samsung Galaxy SII	Dual-core ARM Cortex-A9 @ 1.2 GHz
4. Asus Transformer	Quad-core Tegra 3 T30L @ 1.2 GHz
5. Motorola Xoom	Dual-core Tegra 2 @ 1 GHz

14

For the presented benchmarks, two types of networks were used: homogeneous and heterogeneous. The heterogeneous network is formed using different devices; this simulates real-life scenarios, where the Soldiers will have different types of mobile devices with different characteristics. Figure 5 illustrates the execution times for different-sized heterogeneous networks versus the number of iterations executed by the algorithm.
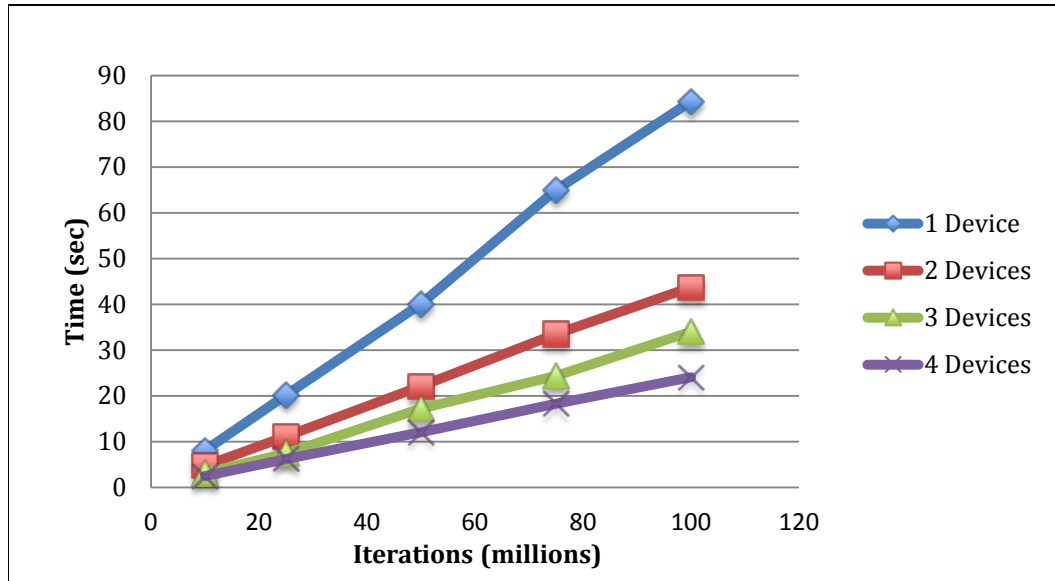
Figure 5. Heterogeneous Network.

In a perfect situation where all the Soldiers have the same type of device with identical characteristics, a homogeneous network can be formed. In this case, the results obtained are significantly better, as there are no time inefficiencies introduced from having different devices.

Figures 5 and 6 demonstrate that as the network size and processor count increases, the execution time decreases, approaching linear scalability in the heterogeneous case and achieving super linear scalability in the homogeneous case.

Figure 6. Homogenous Network.

Tables 2 and 3 numerically represent the results from figures 5 and 6, respectively.

Table 2. Execution Time (sec) for Different Size Heterogeneous Networks vs. Iterations (millions).

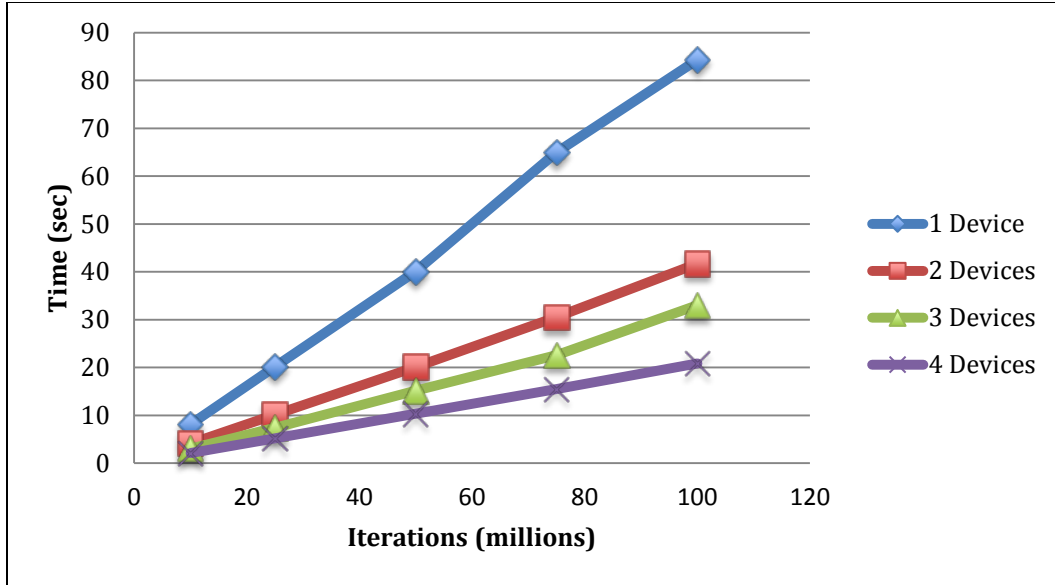| Iterations	1 Device	2 Devices	3 Devices	4 Devices
10	8.11	4.75	3.19	2.49
25	20.21	11.16	7.49	6.22
50	40.08	22.14	17.28	12.06
75	65.02	33.52	24.39	18.30
100	84.34	43.74	34.05	24.09

Table 3. Execution Time (sec) for Different Size Homogeneous Networks vs. Iterations (millions).

Iterations	1 Device	2 Devices	3 Devices	4 Devices
10	8.11	4.15	3.09	2.12
25	20.21	10.16	7.39	5.20
50	40.08	20.14	15.18	10.33
75	65.00	30.52	22.59	15.47
100	84.34	41.74	33.00	20.83

Tables 2 and 3 show that having a homogeneous versus a heterogeneous network could potentially make a large impact on the overall execution time of the system. As the workload increases and more devices are added to the network, the system having a homogeneous network will significantly outperform the system with the heterogeneous network. Executing 100 million

iterations of the PI estimation algorithm with four devices in the network and having a homogeneous network resulted in a 1.16 times faster solution.

4. Summary and Conclusions

Distributed computing using mobile devices has many advantages over traditional distributed computing for applications that use mobile data. The main advantages in computing using mobile devices are in physical location, flexibility, and "on person" computing. BlueHoc provides a multiprocessor-distributed infrastructure for mobile devices, providing an interface for managing data and executing computing jobs on a dynamic mobile network.

BlueHoc provides an effective solution for distributed computing across Android mobile devices and offers an alternate way to gain computational resources for the Army using already available resources that are being underutilized. By utilizing the low-power radio transmissions of Bluetooth, BlueHoc provides the capability to submit computational requests from one device, the master, to a dynamic mobile network without deteriorating the limited power resources needed for processing.

5. References

Chang, C. T.; Chang, C. Y.; Sheu, J. P. BlueCube: Constructing a Hypercube Parallel Computing and Communication Environment Over Bluetooth Radio Systems. in *Journal of Parallel and Distributed Computing*, 2006.

Gartrell, M.; Kelly, J.; Razgulin, S. BlueHydra: Distributed Computing on Mobile Bluetooth-Enabled Devices. Department of Computer Science, University of Colorado, Boulder, CO.

Marinelli, E. Hyrax: Cloud Computing on Mobile Devices Using MapReduce. School of Computer Science, Carnegie Mellon University, Pittsburgh, PA, 2009.

Reisinger, D. Android Smartphone Share Quadruples iOS in Q2. 8 August 2012; https://www.news.cnet.com.

Shepherd, R.; Story, J.; Mansoor, S. Parallel Computation in Mobile Systems Using Bluetooth Scatternets and Java. School of Informatics, University of Wales, Bangor, UK, 2005.

U.S. Army Research Laboratory

SUMMER RESEARCH TECHNICAL REPORT

Enhancing Static Malware Analysis for Android Platforms through Market Basket Analysis

ERIC VENTURINO
MENTOR: WILLIAM GLODEK
COMPUTATIONAL AND INFORMATION SCIENCES DIRECTORATE
ADELPHI, MD

Contents

List of Figures

List of Tables

Abstract

Mobile malware has an increasing presence on commercial mobile computing platforms. Between January 2011 and January 2012, malicious Android applications increased from 139 to 3,069 and malicious families increased from 10 to 37. The Army is deploying Android smart phones and tablets on the battlefield, which may be a target for malware. In our research, we attempt to improve static analysis techniques to determine if an Android application is malicious. Previous works have focused on permission combinations. We expand the search to a larger number of permission and intent combinations to find reliable indicators of potentially malicious activity. We separately mined 306 malicious and 1059 benign Android applications for information that pertained to native code, extra application files, permissions, and intent filter information. Market basket analysis, an analysis to find co-occurrence relationships, was used to examine indicator relationships. The results of market basket analysis from the malicious and benign data sets were compared. We then generated patterns of indicators that detected a high percentage of malware samples with a low false-positive rate. The results show that static analysis can be an effective tool to detect Android malware.

Acknowledgments

Student Bio

Eric Venturino is an undergraduate student entering his senior year at the University of Delaware with plans to graduate in spring 2013. Eric is currently pursuing a Bachelor's of Engineering degree in Electrical Engineering with a minor in Computer Science. In the past, Eric has worked with solar research groups at the University of Delaware. His current topics of interest are mobile security, microcontrollers, and electrical circuits. After graduation, Eric plans to pursue a master's degree in an electrical- or computer-related field of study.

1. Introduction/Background

The Android operating system (OS) has grown significantly since its inception in 2008; as of January 2012, Android holds 61% of the U.S. smartphone market (*5*). Its large user base has attracted malicious actors who have begun to develop Android malware designed to steal sensitive personal, financial, or business information. Android malware can also leverage technologies that are not found in traditional personal computers, such as GPS devices, to potentially access sensitive information. The growth of Android malware (*6*) is significant, and additional protective measures need to be improved.

All Android applications contain a list of requested permissions, such as CALL_PHONE, that is required for the application to function (*7*). Before installing an Android application, a user must acknowledge and grant these permissions. Android permissions are resistant to obfuscation techniques and act as a reliable data point to identify if an application is malicious in nature. Intents are messages received by applications that can listen to specific system events, such as USER_PRESENT. In addition to permissions and intents, embedded Android applications and native code[1] can be examined. Researchers at North Carolina State University have explored Android malware static analysis using sets of parameters but did not employ a statistical method to determine which parameters to examine (*2*).

This paper discusses our research of identifying malicious Android applications by statistical analysis of Android application parameters through market basket analysis (MBA). MBA is a data analysis technique that examines the co-occurrence of different parameters. The following four equations are used in MBA:

1. Support: The probability of parameters used together.

2. Confidence: The conditional probability of parameters.

3. Lift: The ratio of observed support to the support if the parameters were assumed independent. This measures the dependence of the parameters to each other.

4. Conviction: The complement of confidence with the parameters assumed independent to the complement of the observed confidence. This measures confidence effectiveness.

The values of the weights can indicate the relationships of our parameters in malicious and benign applications. In the following sections, we will discuss the experiment, results, and conclusions of this process.

---

[1] Native code allows developers to implement specific portions of an application's code in native-code languages such as C and C++. Many exploits utilize native code.

2. Experiment/Calculations

For our dataset, we gathered 306 Android malware samples from the public database *Contagio* (*8*) and 1039 benign Android applications from third-party stores. An md5 hash of each application was calculated to ensure there was no overlap between our malicious and benign application subsets. Each application was analyzed for permissions, intents, native code, and embedded Android application files. Permissions were found using Androguard[2] [9], and the other parameters were found by adding functionality to Androguard. We applied the above checking system to 80% of benign and 80% of malicious applications, reserving 20% for testing. Binary vectors for each application and their parameters were created and put into either a malicious or benign matrix.

2.1 Market Basket Equations

$$support(X_1,...,X_n) = prob(X_1 \cap ... \cap X_n) \quad confidence(X\,|\,(Y,Z)) = \frac{support(X,Y,Z)}{support(Y,Z)}$$

$$lift(X_1,...,X_n) = \frac{support(X_1,...,X_n)}{prob(X_1) \times ... \times prob(X_n)} \quad conviction(X\,|\,(Y,Z)) = \frac{1-support(X)}{1-confidence(X\,|\,(Y,Z))} \tag{1}$$

The two matrixes, malicious and benign, were used to find the MBA weights for a single parameter, two parameters, and three parameters. To increase the speed of this process, only parameters that occurred more than 12% of the time were used. After calculating the MBA weights for support, lift, confidence, and conviction, we sorted a list for each equation for parameter sets to prioritize the strongest indicators of malware from best to last. They were sorted primarily by the benign weights from low to high and secondarily by the malicious weights from high to low.

We constructed multiple filters by continuously adding the next prioritized parameter set in our list. Each time a filter was made, it was run against the remaining 20% of the applications, which were reserved for testing and therefore not used in our filter construction. True and false positive rates were calculated for every filter containing the parameter sets in the prioritized list. Filters were made for the weights of support, lift, confidence, and conviction. The experiment was repeated through five-fold cross validation for support, where the applications were sorted by their md5 hash. Five-fold cross validation was not performed on all four equation weights because their initial results showed their weights to be less effective than supports, and there was a time constraint for the summer.

---

[2] Androguard is an open source reverse engineering tool for Android.

3. Results and Discussion

Using support to identify effective parameter sets for finding unknown malware provided the best performance for all the market basket weights. Our support-based filters on average were able to detect 63% of the unknown malware with a 0% false positive rate. The best filter (figure 1) detected 72% of unknown malware with a 0% false positive rate. Also, increasing the parameters in the early filter stages increased the amount malware detected while maintaining a low false positive rate. This can be seen in figure 1, where a 77% true positive rate and a 1% false positive rate were achieved. (See table 1 for true positives at 0% and 1% false positives.)
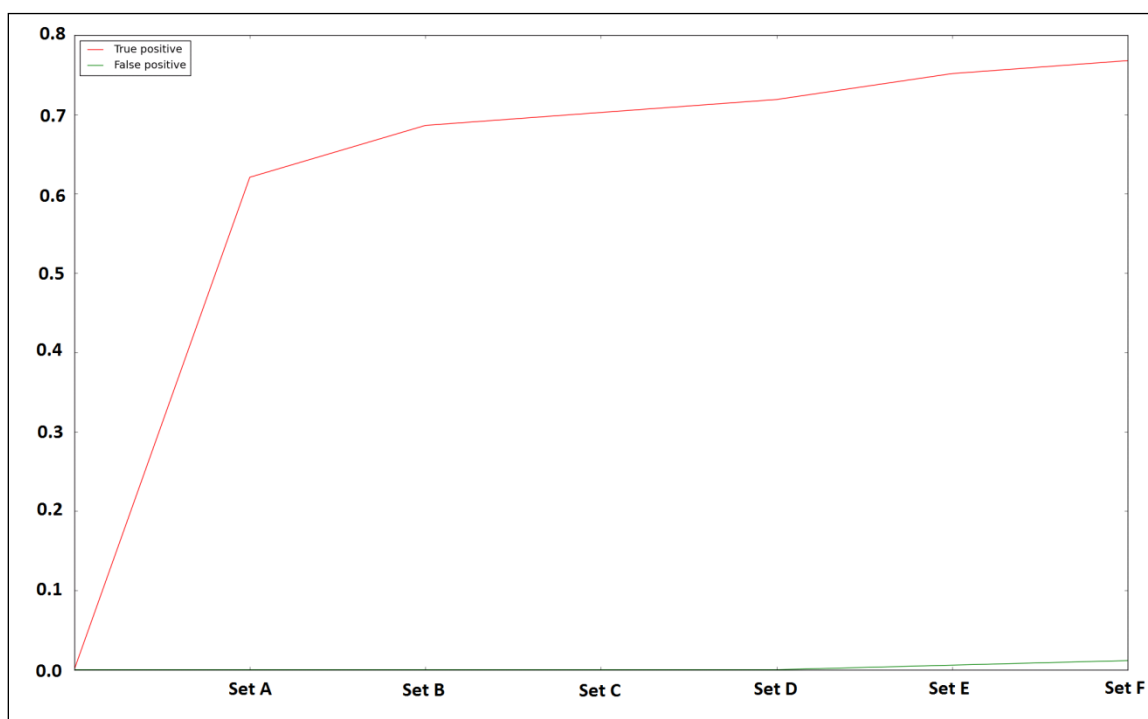

Figure 1. Fraction of applications (malicious and benign) caught by additive filters (best results).

Table 1. True positives at 0% and 1% false positives, respectively.

	Run #1	**Run #2**	**Run #3**	**Run #4**	**Run #5**	**Runs Averaged**
True positive at 0% false positive	55.6%	71.9%	55.6%	65.4%	67.0%	63.1%
True positive at 1% false positive	58.8%	76.8%	68.6%	70.2%	67.0%	68.3%

Certain parameter combinations were effective in detecting unknown malware, while others triggered false positives. The first parameter set in table 2 caught over 47% of unknown malware in all of the tests. This shows that combining parameters together instead of using single parameters can lower the false positives and maintain high true positives. The true and false positives of individual parameters (figure 2) are compared to when they are combined together in the filters (table 2). There were other high-prioritized parameter sets, which included parameters like INSTALL_PACKAGES, but were not effective in detecting additional malware. While they did not detect additional malware, they should still be left in the filter because they could detect different unknown malware not in our data set. The next effective parameter set in the table did not use SEND_SMS but used the intent USER_PRESENT. This shows that intents are effective in finding unknown malware, and that malware is missed when just searching for SMS permissions.

Table 2. Parameter sets with effect in best additive filter.

| True Positive	False Positive	Change in Apps Caught	Parameter 1	Parameter 2	Parameter 3
62.1%	0%	+62.1%	INTERNET	WRITE_EXTERNAL _STORAGE	SEND_SMS
68.7%	0%	+6.6%	INTERNET	WRITE_EXTERNAL _STORAGE	PHONE_STATE
70.3%	0%	+1.6%	SEND_SMS	ACCESS_NETWORK _STATE	USER_PRESENT
71.9%	0%	+1.6%	INTERNET	SEND_SMS	PHONE_STATE
71.9%	0.6%	-0.6%	USER_PRESENT	READ_PHONE_STATE	
75.2%	0.6%	+3.3%	INTERNET	SEND_SMS	SET_WALLPAPER
75.2%	1.2%	-0.6%	CALL_PHONE	SET_WALLPAPER	BOOT_COMPLETED
76.8%	1.2%	+1.6%	CALL_PHONE	RECEIVE_WAP_PUSH	
76.8%	1.7%	-0.5%	CALL_PHONE	Embedded .apk file	
76.8%	2.3%	-0.6%	GET_TASKS	READ_SMS	Embedded .apk file
76.8%	3.5%	-1.2%	CALL_PHONE	ACCESS_COARSE _LOCATION	BOOT_COMPLETED
76.8%	4.1%	-0.6%	READ_HISTORY _BOOKMARKS	ACCESS_COARSE _LOCATION	BOOT_COMPLETED
76.8%	4.6%	-0.6%	SET_WALLPAPER	ACCESS_COARSE _LOCATION	BOOT_COMPLETED
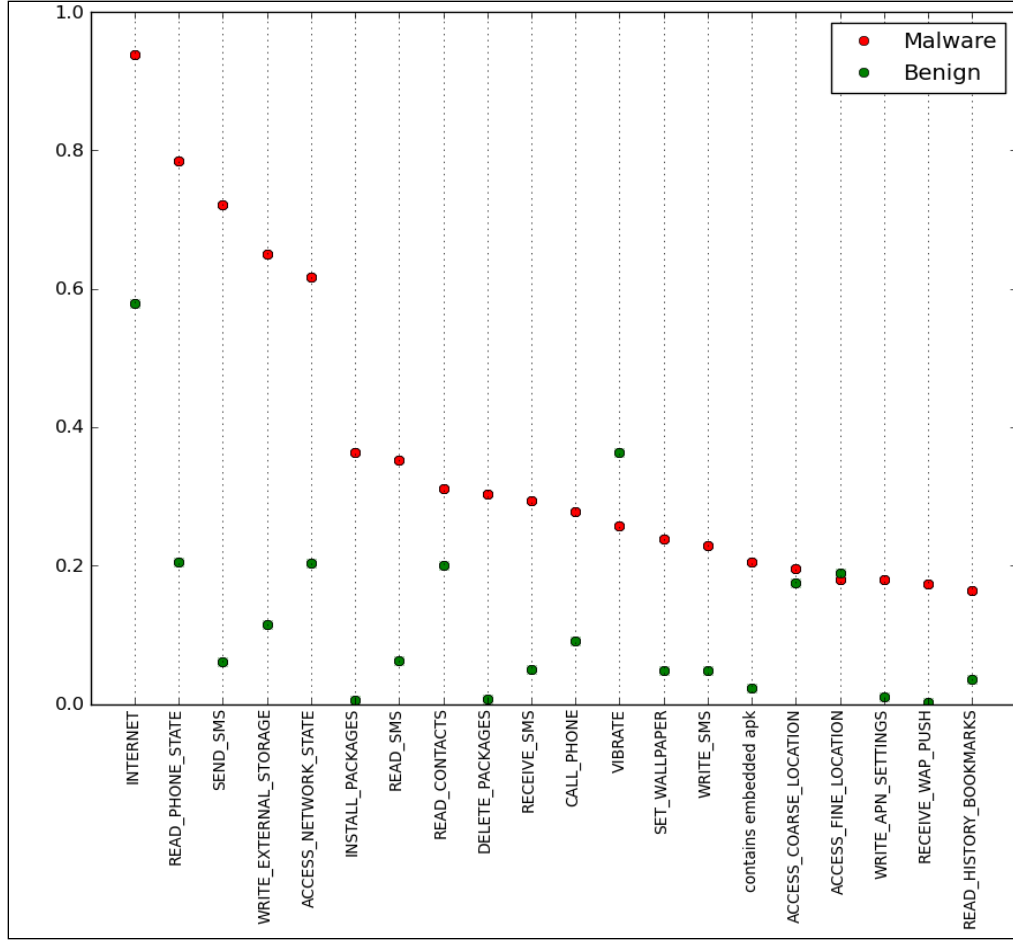
Figure 2. Top 20 permissions requested in malware.

Certain parameter combinations caused false positives. In the results, a set of only two parameters triggered false positives more often than a three-parameter set in the filter's early stages. More parameters in a set will result in more specific search and in a lower number of false positives. Table 3 shows that the method of looking for malware through parameter combinations is more effective when the malware has a higher number of parameters but would miss malware that use a small number of parameters. For example, malware with just SEND_SMS and INTERNET parameters would not be detected without increasing the false positive rate.

Table 3. Average number of parameters in best additive filter with 2% false positive.

	Average # Permissions	Average # Intents	Average # Apks Embedded	Average # Native Code
Malicious Apps (True Positive)	12.5	5.8	0.24	0.07
Benign Apps (False Positive)	10.4	1.2	0.45	0
Malicious Apps (False Negatives)	3.6	1.5	0.12	0.22
Benign Apps (True Negatives)	3.4	8.1	0.01	0.1

Specific parameters that triggered low false positives in combinations with other parameters were ACCESS_COARSE_LOCATION, BOOT_COMPLETED, and contain extra .apk. Though the false positive rates are not high, these indicators are not as strong as others that could be used. It could be possible that the benign set of data contained malware because there are many variants of Android malware that may not have been in our malware data set, and some parameter combinations that caused false positives seem suspicious. For example, in one, a false positive result was triggered by INTERNET, SEND_SMS, and SET_WALLPAPER.

Another interesting result of this analysis was the ineffectiveness of the presence of native code containment as compared to other parameters. While native code containment does appear in malware for exploits, it often appears in benign applications for legitimate purposes as well. These legitimate purposes can be used in benign applications that exploit the phone so the user can have more control or applications where native code will allow for things like faster speeds. Native code by itself does not seem to be a strong indicator of malware, but signatures for specific exploits could be.

While MBA support was beneficial for detecting malware, the other weights did not work as well. This can be attributed to the fact that support is the probability of the given parameters being in an application. The next best performing MBA weight was the confidence since it is also evaluated the probability of a parameter. Lift and conviction were not as strong as indicators because the lift and conviction are examining the dependence of the support and confidence results, respectively. Examining the dependence of parameters is useful when trying to find which parameters are being used together often in one set of data. However, when there are two sets of data, in our case malicious and benign, it is not as useful since we were trying to find parameter combinations that were strong indicators of malware but not benign applications.

4. Summary and Conclusions

This paper discussed using MBA to examine Android applications for malicious indicators. Our method found 63% of unknown malware while having a 0% false positive. This analysis shows that statistically examining Android applications for parameters can be useful for finding unknown malware, and that static analysis of Android applications can be highly effective when using the correct parameter searches.

In the future, it would be best to focus less on two parameter sets and focus on parameter sets with three or more parameters. It will be important to expand parameters beyond our four categories. These new parameters might include information relating to pending intents, reflection code, obfuscation, encryption, certain function calls, and the extra parameters inside embedded Android application files. These changes will allow for more specific searches and keep a low false positive rate. Also, for more optimized results, changing the cutoff to other cutoffs besides 12% would be helpful. This might help discover malware that has a unique set of parameters that occur less frequently than parameter sets for common schemes such as premium SMS fraud.

In addition to these changes in our method, it will be important to obtain Android applications from Google play where there may be less of a chance there is malware [10] and also to use a larger set of malicious and benign applications to better calculate the market basket weights. In addition to other future ideas for this process, it would be useful to go beyond known Android malware data sets and apply the filtering of parameter sets to Android application stores and on Android devices. By doing this, we could discover unknown malware and apply new learned knowledge to our system.

5. References

1. Android Malware Families Nearly Quadruple From 2011 to 2012.
    http://www.zdnet.com/blog/security/android-malware-families-nearly-quadruple-from-2011-to-2012/12171.

2. Zhou, Y.; Wang, Z.; Zhou, W.; Jiang, X. *Hey, You, Get Off of My Market: Detecting Malicious Apps in Official and Alternative Android Markets*, Department of Computer Science, North Carolina State University, 2012.

3. Enck, W.; Ongtang, M.; McDaniel, P. *On Lightweight Mobile Phone Application Certification. Department of Computer Science and Engineering*, The Pennsylvania State University, 2009.

4. Hastie, T.; Tibshirani, R.; Friedman, J. H. *The Elements of Statistical Learning: Data Mining, Inference, and Prediction*; Springer: New York, 2009.

5. Droid Life. http://www.droid-life.com/2012/05/07/androids-market-share-balloons-to-61-in-the-u-s-during-q1-ios-drops-to-29/.

6. Android Malware Numbers Explode to 25,000 in June 2012. http://www.zdnet.com/android-malware-numbers-explode-to-25000-in-june-2012-7000001046/.

7. Manifest.permissions.http://developer.android.com/reference/android/
    Manifest.permission.html#CALL_PHONE

8. Contagio Mobile. http://contagiominidump.blogspot.com/.

9. Androguard. http://code.google.com/p/androguard/.

10. F-Secure. Mobile Threat Report Q1 2012. www.f-secure.com/weblog
    /.../MobileThreatReport_Q1_2012.pdf. 2012.

Human Research & Engineering Directorate (HRED)

INTENTIONALLY LEFT BLANK.

U.S. Army Research Laboratory

SUMMER RESEARCH TECHNICAL REPORT

Assessment of Screening Obscuration Module Technology

JUAN KELLY

MENTOR: LAMAR GARRETT

HUMAN RESEARCH AND ENGINEERING DIRECTORATE

ABERDEEN PROVING GROUND, MARYLAND

Contents

List of Figures

List of Tables

Abstract

The Screening Obscuration Module (SOM) produces a cloud of obscurants in the visual spectrum. The SOM was developed to protect Soldiers from enemy observation and fire by providing them with the capability to conceal themselves and their equipment in open terrain. Two vendors, each with different conceptual designs, created SOM prototypes. The prototypes were assessed in mounted and dismounted configurations during developmental tests, and early user evaluations to obtain operational feedback. Post-test questionnaires, informal interviews, and observation/comment cards were used to collect feedback. Among the data collected during these test events were demographics, anthropometric measurements, and New Equipment Training feedback. The data were used to determine how well the SOM prototypes met key performance requirements, and to identify design changes required to improve the usability, survivability, reliability, and effectiveness of the system. This report focuses on the Technological Development Phase Testing conducted to assess the ability of the two vendors' SOM designs to operate in a mounted and dismounted environment.

Acknowledgments

Student Bio

The fall 2012 semester marks my junior year at Morgan State University as an Industrial Engineering major. My summer work with the U.S. Army Research Laboratory has been my first research opportunity related to my course of study. After graduating with a bachelor's degree, I plan to attend graduate school so that I am prepared for industry when I start my career as an engineer.

1. Introduction/Background

The Screening Obscuration Module (SOM) is a generator module prototype that produces an obscuring cloud in the visual spectrum. Obscurant clouds reduce target-to-background contrast, making the target more difficult to detect, observe, and engage. To protect Soldiers from enemy observation and fire, the SOM is intended to conceal the individual, manned and unmanned vehicles, and dismounted personnel in open terrain.

The primary objective of the SOM is to provide enhanced protection for combat/maneuver vehicles. SOM will support maneuvers contributing to a unit's ability to move away from or to positions of advantage with respect to the enemy and defeat or disrupt enemy forces' intelligence to conduct accurate targeting on U.S. forces. The SOM program focuses on replacing current technology using smoke pots with a medium-area screening obscuration device.

Currently, medium-area screening obscuration capabilities are limited to smoke pots containing hexachloroethane (HC). Such smoke pots have the following limitations:

- Harmful vapors are produced.

- Not designed for use on manned and unmanned platforms.

- Not capable of turning off after ignition.

- Resupply is logistically cumbersome.

The SOM will address these problems to increase the usability and safety of the system. To this end, two vendors created SOM prototypes, each with a different conceptual design. One vendor used a fuel burner/heater-based fog oil vaporizer, which heats the fog oil directly, whereas the other vendor used a mini-turbine engine–based fog oil generator that heats the air and injects cold fog oil into it.

1.1 Test Objectives

Testing sought to address the following objectives:

- Gather Soldier feedback for prototype assessment in the mounted and dismounted positions to obtain operational feedback, including ease of setup, ease of use, and maintainability of the SOM.

- Collect anthropometric measurements in standing and seated positions to determine what percentile of the population was represented by the test population. The anthropometric measurements that were taken were stature, weight, hand circumference, hand breadth, hand length, sitting height, and thumb tip reach. This paper contains an example calculation

41

for the stature measurement as well as what percentile of the population this measurement represented.

- Identify the presence of hazards during transportation, setup, operation, and tear-down of the SOM.

1.2 Test Location

Testing took place at Aberdeen Proving Ground Edgewood Area, MD. Data collection events included the following:

- NET feedback

- Mission CONOPS feedback

- Post-test feedback

1.3 Participants

Ten participants ($N = 10$) participated in the test event. All 10 were members of the target audience: Military Occupational Specialty 74D – Chemical Specialists. Following is a summary of some of the demographic data, which provides insight into the characterization of the subject population:

- Age: *Range* = 20–40 years (*M* = 25.10, *SD* = 6.10)

- Time in Service: *Range* = 1 year, 11 months–12 years, 2 months (*M* = 4.64, *SD* = 3.53)

- Rank: E-3 = 10%, E-4 = 50%, E-5 = 10%, E-6 = 30%

- Stature Calculation: *Range* = 26.3, *Min* = 157.6, *Max* = 183.9, *M* = 169.77, *SE* = 3.14, *SD* = 9.94

- Stature %: *Range* = 65, *Min* = 25, *Max* = 90, *Mean* = 55, *SE* = 7.71, *SD* = 24.38

2. Experiment/Calculations

The purpose of collecting the anthropometric measurements was to determine how well the participants' measurements represented the 5th to 95th percentile for the male and female military population. In order to understand the correlation between the participant sample and the Army population, we needed to calculate the percentile that each Soldier represented (table 1 and figure 1). A description of the calculation method is as follows:

Calculating the sample's 100th percentile:

1. Order the *n* observations from smallest to largest.

2. Determine the product *np (observations x percentile).*

- If *np* is not an integer, round it up to the next integer and find the corresponding ordered value.

- If *np* is an integer, say *K*, calculate the mean of the Kth and the $(K+1)^{st}$ ordered observations.

Therefore, we look at the Kth observation = 9th observation = 182.90 (71.00 in), and (K + 1) observation = 10th observation = 183.90. The mean of the 9th and 10th observations is 183.40. So, we identify that 183.40 cm for the stature is a 90th percentile observation in our sample.

Table 1. Example calculation of stature percentile.

Anthropometric Data (Stature in cm)	Anthropometric Data (Stature in inches)	Percentile
157.60	62.00	25
159.50	63.00	35
161.50	63.60	45
162.80	64.10	55
165.20	65.00	65
169.90	66.00	25
174.40	67.00	45
180.00	69.00	75
182.90	71.00	90
183.90	72.00	90

n = 10, p = .90, np = 9.00
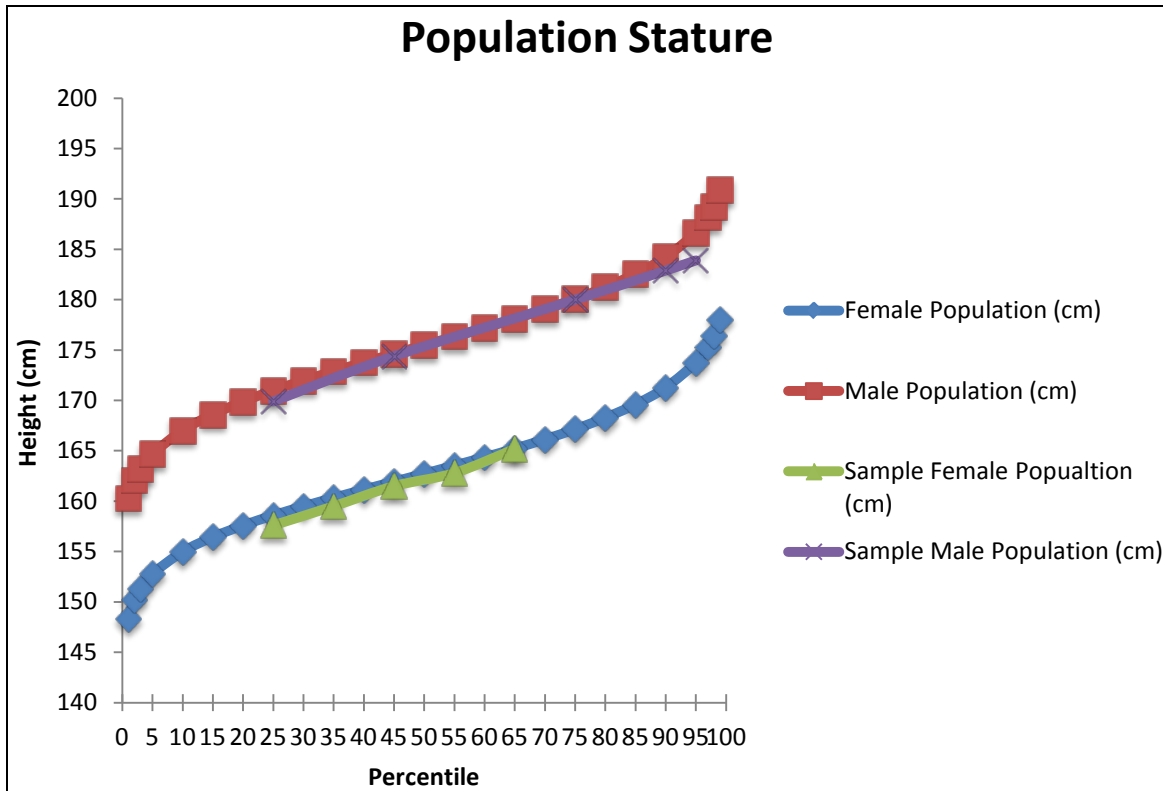
Figure 1. Population stature.

3.   Results and Discussion

Collecting data throughout the early user evaluation (NET Feedback, Mission CONOPS Feedback, and Post-test Feedback) enabled us to thoroughly evaluate the two prototype systems under test and collect ease of setup, ease of use, and maintainability data. We identified critical risk factors, specific system feature attributes that Soldiers found effective, and those that require improvement for each system.

Participant demographics and anthropometric measures provided the data to determine that all of the Soldiers were representative of the current military population within the 5th to 95th percentile for male and female values.

The NET and post-test questionnaires used a five-point rating scale. In order to qualify as an acceptable rating, 85% of the participants must have assigned a rating of good ("4") or excellent ("5") to the survey item under evaluation. If the item did not meet the 85% acceptability target, one-on-one interviews were held to examine the reasoning behind the "low" ratings. During these interviews, we obtained Soldier recommendations so that they could be considered when mitigating design and training issues.

Overall, NET received unfavorable evaluation ratings (84% or lower). The Soldiers were more satisfied with the training provided by Vendor 2 than that provided by Vendor 1. However, both vendors still need to improve upon material presentation to the Soldiers. It is possible that problematic aspects of the systems experienced during training may have influenced the Soldiers' perception of training.

We obtained Soldier feedback after they used the equipment. Issues were identified for each system. For example, the following two issues were identified by Soldiers:

- "It takes too long to mount the SOM onto the HMMWV, therefore endangering the Soldiers being rescued as well as those rescuing others." (Vendor 1 issue)

- "[The] smoke screen seemed to cover more area faster. [The] smoke is lower to the ground and thicker." (Vendor 2 issue)

Results reflect Soldier perceptions of the SOM Soldier-system interaction. Several issues were identified after both systems were used. The following issues, which should be mitigated in future prototype designs, were identified:

- SOM generated noise levels in excess of the maximum allowable levels prescribed in MIL-STD-1474D. To mitigate this issue, Soldiers were provided combat earplugs to correct the noise issues and protect them when standing within 0.8 m (2.5 ft) of Vendor 1 and within 17.7 m (58 ft) of Vendor 2 when the SOM was mounted or dismounted.

- A faster way to access and replace the battery is needed.

- Battery pack needs an indicator to determine battery usage/remaining batter life.

- Core module, which currently has one strap for both systems, should have two straps to balance the weight.

- Carrying issues for mixed-gender weight-lifting limits.

- The SOM fog oil and fuel containers exceeded the weight limit guidelines outlined in MIL-STD-1472G.

- Fog oil was discharged to the vehicle's exterior after system shutdown. (Vendor 1)

- Unable to use wirelessly because the tether was not working for the remote control unit. (Vendor 2)

- Fog oil leaked from the exhaust when the SOM was turned on its side. (Vendor 2)

4. Summary and Conclusion

Overall, testing of the prototypes was very successful. Soldiers provided excellent operational feedback and identified many issues that would negatively impact mission performance. Soldiers stated that they preferred a design that would be simple yet effective. Both systems require additional improvements prior to conducting operational testing, such as:

- A thermal barrier coating to reduce mini-turbine exhaust temperature, size, and weight reduction.

- A remote control unit that self-charges multiple SOM systems.

- System self-charging while in use.

- A second battery to increase mission time.

Safety precautions should be taken into consideration prior to operating the SOM systems, such as wearing hearing protection during dismounted operation. It is recommended that this could be addressed in the vendors' operating manuals.

5. References

Ahearn, W. P.; Clatterbaugh, J. E. *Detailed Test Plan Technology Feasibility Test*, Jan 2012.

Johnston, V. F. *Testing and Evaluation Master Plan*, 20 Sep 2011.

Maneuver Center of Excellence Mounted & Dismounted Requirements Directorates and Maneuver Center of Excellence Combating Weapons of Mass Destruction -Requirements Directorate Requirement Determination Division, *Screening Obscuration Module Tactics, Techniques, and Procedures,* May 2012.

U.S. Army Evaluation Center, *Screening Obscuration Module - Technology Development Phase,* Jan 2012.

INTENTIONALLY LEFT BLANK.

U.S. Army Research Laboratory

SUMMARY RESEARCH TECHNICAL REPORT

Testing and Validating a Novel Method to Assess Muscle Fatigue via Surface Electromyography

MATTHEW SHERIDAN TENAN
MENTOR: HARRISON PHILIP CROWELL
HUMAN RESEARCH AND ENGINEERING DIRECTORATE
ABERDEEN PROVING GROUNDS, MD

Contents

List of Figures

Abstract

Determination of dismounted Soldier muscular fatigue is of paramount importance to Army operations. The median frequency (MPF) of the surface electromyogram (EMG) is a reliable method of determining muscle fatigue in isometric conditions, but not dynamic movement. Recent research indicated that rectified frequency spectrum more accurately reflects the firing rates of the muscle fibers; therefore, the rectified median frequency (rMPF) may prove more valid for fatigue determination than MPF. This study tested the hypothesis that both MPF and rMPF would decrease throughout a fatiguing isometric exercise. This study tested 17 subjects during an isometric knee extension held at 25% maximal force production. MPF and rMPF were calculated at the start of exercise and at 10% intervals until task failure. Both MPF and rMPF were found to significantly decrease across the task ($p<0.05$). Further, while MPF and rMPF were shown to be significantly different from each other at each stage ($p<0.05$), the pattern of change across the isometric task was similar. Thus, this study demonstrates the potential utility of rMPF in determination of muscle fatigue. Future studies should investigate whether rMPF outperforms MPF as an indicator of muscular fatigue in dynamic tasks and can be used in operationally relevant tasks.

Acknowledgments

Student Bio

Matthew S. Tenan, MA ATC, received a B.S. in Athletic Training/Exercise Science from Ithaca College (2007) and an M.A. in Exercise Physiology from the University of North Carolina at Chapel Hill (2009). He is currently working to complete his third year of Ph.D. study at the University of Texas at Austin in the Neuromuscular Physiology Laboratory. Presently, he has three peer-reviewed publications and five published abstracts. His current research interests are nervous system interactions with the neuroendocrine system and the neurophysiology of fatigue.

1. Introduction/Background

Muscle fatigue in the dismounted Soldier decreases the Soldier's ability to perform operationally relevant tasks and may lead to increased rates of injury (*1*). Operationally defining muscle fatigue as the inability to maintain a prescribed force (*2*) is problematic with Soldier research because isolating specific muscle forces cannot be performed within a task that involves multiple muscle groups. Surface electromyography (EMG), which measures the global electrical activity of the muscles underlying a surface electrode (*3*), may be vital to the functional assessment of muscular fatigue in Soldiers.

As a time-series measurement, EMG can be decomposed into a frequency power spectrum via a fast Fourier transform. The decrease in the median frequency of this power spectrum (MPF) is a validated method to gauge muscular fatigue in isometric conditions (*4*). Previous studies utilizing MPF in dynamic exercise have determined this metric is highly variable and an inconsistent metric for assessing muscle fatigue (*5*, *6*). A recent modeling study determined that in a coherence analysis, which examines the spectral properties of two independent power spectrums, the rectified form of EMG most accurately reflects the depolarization rates of the underlying muscle fibers (*7*). Therefore, a rectified median frequency (rMPF) may be a more consistently valid metric for fatigue determination than MPF.

The purpose of this study was to determine if MPF and rMPF respond similarly during an isometric fatiguing task. If the two metrics respond the same in isometric fatigue, further studies should compare rMPF and MPF in dynamic fatiguing conditions to determine if rMPF is a more consistently valid metric.

2. Experiment/Calculations

2.1 Participants and Data Collection

Seventeen men (n=10) and women (n=7) between the ages of 18 and 35 participated in this study. The women were all tested in the early follicular phase of their menstrual cycle. Participants were excluded from the study if they had any history of neurologic, cardiovascular, endocrine, or metabolic disorders. Any histories of surgery, immobilizations, arthritis, or chronic injury to the dominant leg were also factors for disqualification. Additionally, the female participants must have been hormonal contraception naïve for at least 6 months prior to testing. All participants gave their informed consent in accordance with the Helsinki Declaration.

All data collection was performed in the climate-controlled Neuromuscular Physiology Laboratory at the University of Texas at Austin. Participants were instructed to not participate in

any strenuous physical activity 48 h prior to their study visit. They were not permitted to participate if they consumed alcohol or caffeine less than 8 h prior to their visit.

Participants were seated in an adjustable chair with the dominant hip and knee fixed at 90º. The waist and dominant thigh were immobilized with pads and straps. Next, the participant performed a light warm-up consisting of 12 dynamic submaximal knee extensions. The dominant ankle was then strapped to a padded restraint attached to the strain gauge (Entran Sensors & Electronics, Fairfield, NJ). The participant was instructed to perform a maximal isometric contraction (MVC) of the knee extensor muscles for 3 s. MVCs were performed until three MVCs of commensurate values were obtained. The three MVCs were averaged and used in the calculation for the endurance task.

After the participant completed the MVCs, the skin was lightly abraded and cleaned with 70% isopropyl alcohol, and two passive surface electrodes were placed on the vastus medialis in approximation with the muscle fiber pennation for EMG detection. The interelectrode distance was 100 mm. The EMG signal was then amplified 100 times (Coulbourn Instruments, Whitehall, PA) and sampled at 1024 Hz. A ground electrode was placed on the contralateral patella.

Once the equipment had been appropriately applied to the participants, they were instructed to maintain a knee extension force of 25% MVC until instructed to stop. Visual feedback was provided on a monitor, which displayed their force production. The test was terminated (task failure) when the participant was unable to maintain 20% of MVC for 2 s or when force tremor oscillations exceeded 5% MVC within a 1-s period.

2.2   Data Reduction

The data were first divided into 2-s (2048 sample) increments at the start of force maintenance and every decile until task failure. The raw EMG data segments were band-pass filtered at 8–500 Hz using a fourth-order recursive Butterworth filter. One set of raw EMG data were then full-wave rectified and low-pass filtered at 100 Hz using a fourth-order recursive Butterworth filter. The power spectrums for the two signals were then calculated via FFT using Welch's method with 50% overlapping Hanning windows. The MPF and rMPF were defined as the frequency that divides the spectrum into areas of equal power for their respective waveform.

2.3   Statistical Analysis

All data reduction was performed in SAS (version 9.2, Cary, NC). A two-way mixed model ANOVA was utilized with Dunnett corrections for multiplicity. Global α was set at $p < 0.05$.

3. Results and Discussion

3.1 Results

There was a significant effect for the rectification process of the signal (p<0.0001) as well as a significant effect of time (p<0.0001); however, there was no significant interaction for rectification and time together (p=0.5281). Post hoc comparisons for MPF and time determined that MPF was significantly lower than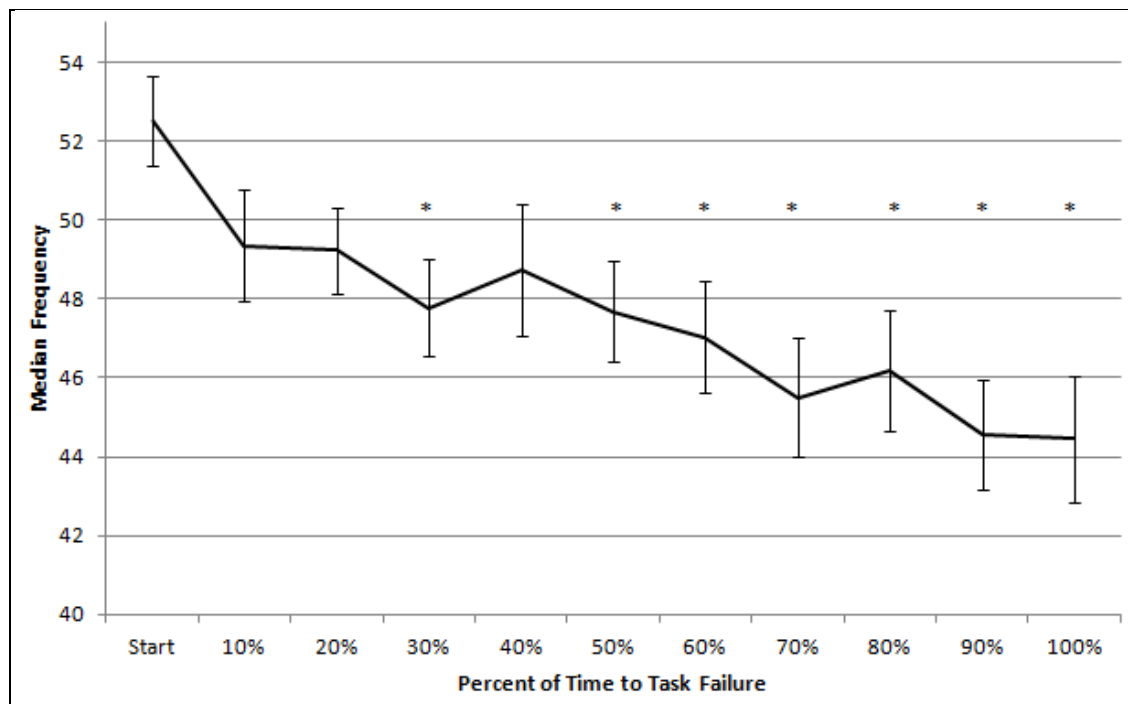 start at 30% of time to task failure (p=0.0237) (figure 1). The post hoc comparisons for rMPF and time revealed that rMPF was significantly lower than start at 90% of time to task failure (p=0.0032) (figure 2).

Figure 1. The mean MPF across the endurance task. (Error bars indicate standard error from the mean. Asterisks (*) indicate times at which MPF is significantly different (p<0.05) from MPF at the start of the trial.)
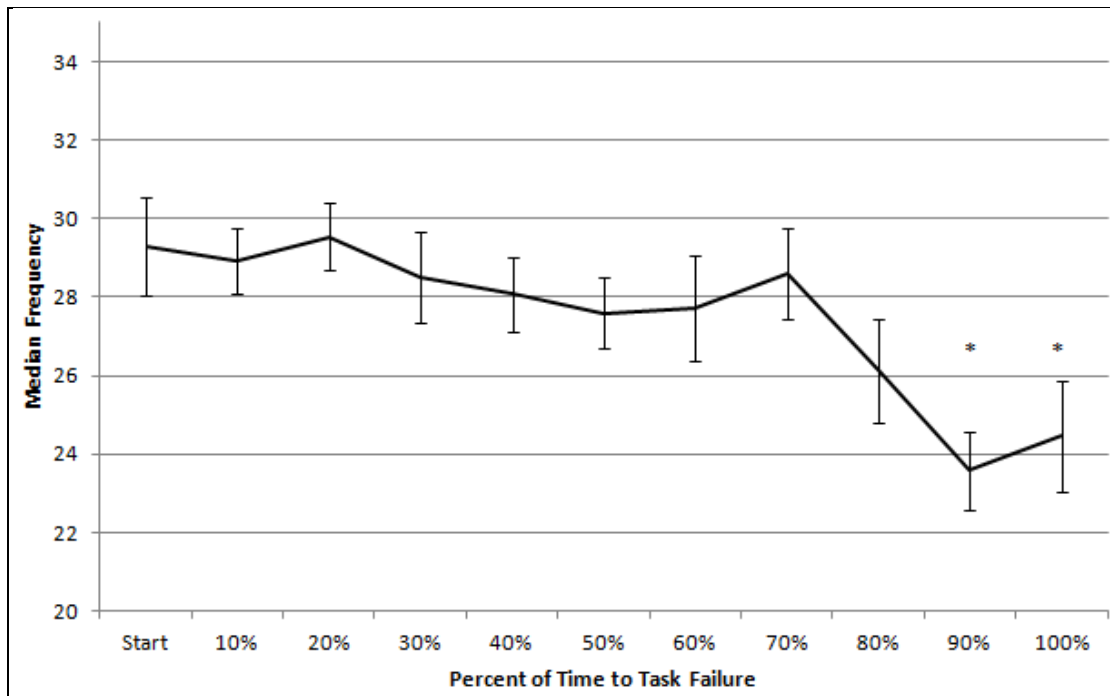
Figure 2. The mean rMPF across the endurance task. (Error bars indicate standard error from the mean. Asterisks (*) indicate times at which rMPF is significantly different (p<0.05) from rMPF at the start of the trial.)

3.2 Discussion

This study confirms previous reports of decreases in MPF across an isometric fatiguing exercise. MPF was significantly lower than start at 30% of the time to task failure and, with the exception of a slight increase at 40%, remained significantly different for the duration of the exercise. The present data indicate that changes in MPF may be useful in gauging levels of fatigue (i.e., some fatigue, heavy fatigue, etc.) in isometric exercise. rMPF, on the other hand, showed significant decreases from start at 90% of task failure, which persisted through eventual task failure. It should be noted that if not for the multiple-comparison adjustments, rMPF at 80% would have been significantly lower than the starting rMPF. Therefore, a decrease in rMPF may indicate if the muscle is at an unsustainable level of work or near task failure. While MPF may represent a continuous gradation of fatigue, rMPF may represent a binary outcome (i.e., is the muscle fatigued: yes/no) in isometric conditions.

MPF in dynamic conditions has not proven consistently valid for measuring fatigue. If future research can confirm that rMPF decreases near task failure in dynamic exercise, it will be a useful assessment of Soldier muscle fatigue. Determining what muscle is fatigued during prolonged load carriage, for example, will lead to more appropriate exercise training programs, rucksack design, and Soldier assistive technologies.

4. Summary and Conclusions

rMPF appears to be a valid analogue of MPF in isometric exercise. Both signal metrics show significant decreases across an isometric task to failure. Further research needs to apply these metrics in fatiguing tasks that are operationally relevant for Soldiers. If rMPF proves to be a more consistently valid metric than MPF in dynamic exercise, it should be utilized for the assessment of Soldier muscle fatigue in field studies.

5. References

1. Mair, S. D.; Seaber, A. V.; Glisson, R. R.; Garrett, W. E. The Role of Fatigue in Susceptibility to Acute Muscle Strain Injury. *The American Journal of Sports Medicine* **1996**, *24*, 137–143.

2. Edwards, R.H.T. Biochemical Bases of Fatigue in Exercise Performance: Catastrophe Theory of Muscular Fatigue. in *Biochemistry of Exercise*, Knuttgen, H.G., ed., Human Kinetics, 1983.

3. Farina, D.; Merletti, R.; Enoka, R. M. Extraction of Neural Strategies from the Surface EMG. *Journal of Applied Physiology* **2004**, *96*, 1486–1495.

4. Viitasalo, J.; Komi, P. V. Signal Characteristics of sEMG During Fatigue. *European Journal of Applied Physiology* **1977**, *37*, 111–121.

5. Tenan, M. S.; McMurray, R. G.; Blackburn, B. T.; McGrath, M.; Leppert, K. The Relationship Between Blood Potassium, Blood Lactate, and Electromyography Signals Related to Fatigue in a Progressive Cycling Exercise Test. *Journal of Electromyography and Kinesiology* **2011**, *21*, 25–32.

6. Gerdle, B.; Larsson, B.; Karlsson, S. Criterion Validation of Surface EMG Variables as Fatigue Indicators using Peak Torque: a Study of Repetitive Maximum Isokinetic Knee Extensions. *Journal of Electromyography and Kinesiology* **2000**, *10*, 225–232.

7. Boonstra, T. W.; Breakspear, M. Neural Mechanisms of Intermuscular Coherence: Implications for the Rectification of Surface Electromyography. *Journal of Neurophysiology* **2012**, *107*, 796–807.

Sensors and Electron Devices Directorate (SEDD)

INTENTIONALLY LEFT BLANK.

U.S. Army Research Laboratory
SUMMER RESEARCH TECHNICAL REPORT

Synthesis and Characterization of Boron-based Additive for Novel Electrolyte Systems of Lithium-ion Batteries

WALLACE DERRICOTTE
MENTORS: ARTHUR VON CRESCE AND KANG XU
SENSORS AND ELECTRON DEVICES DIRECTORATE
ADELPHI, MD

Contents

List of Figures

List of Tables

Abstract

Essential to the chemistry of lithium-ion batteries is the formation of a solid electrolyte interface (SEI) on the surface of carbon-based anodes. Additives are used to alter the chemistry of the SEI and how it interacts with the lithium ion transport process. Boron- and silicon-based additives are of particular interest due to their respective reactivity and possibility to form soluble complexes in solution. The additives are synthesized from commercially available boron trichloride (BCl_3), silicon tetrachloride ($SiCl_4$), and perflouro-t-butanol. Upon lithiation, the perflouro-t-butyl alkoxide can participate in an addition reaction with BCl_3 and $SiCl_4$, adding at the chlorine sites on each compound. Upon synthesis, the compounds will undergo a series of chemical characterization and electrochemical characterization. Chemically they will be classified using boron/fluorine nuclear magnetic resonance (NMR), electrospray mass spectroscopy, and Fourier transform infrared (FTIR) spectroscopy. Electrochemically, the compounds will be tested as additives in battery cells using the industry standard electrolyte (ethylene carbonate [EC]: ethyl methyl carbonate [EMC]/30:70), a graphite anode, and copper-based cathode material. The batteries will undergo multiple cycles to determine how well they perform through extended use.

1. Introduction

Lithium-ion batteries have become an industry standard in rechargeable power source technology. Lithium gained attention for two reasons: first, it is the most electronegative of all metals (~3.0 V vs. SHE), allowing it to have a high cell voltage when coupled with certain cathode materials; second, it is the lightest metal (0.534 g cm^{-3}), making it an anode with high specific capacity (3.86 Ahg^{-1}). Lithium-ion battery technology is also desired by the rechargeable battery industry because of the reversibility of its redox chemistry. Lithium can be transported back and forth, reducing both the cathode and anode reversibly.

The standard lithium-ion battery consists of an anode (negative electrode), which is generally graphite or some other carbonaceous material, a cathode (positive electrode) composed of phosphates or oxides, and an electrolyte. (See figure 1 for a schematic of the transfer of lithium.) The electrolyte is a system composed of a solvent and a salt that work in tandem to allow the flow of ions while at the same time insulating electric charge.
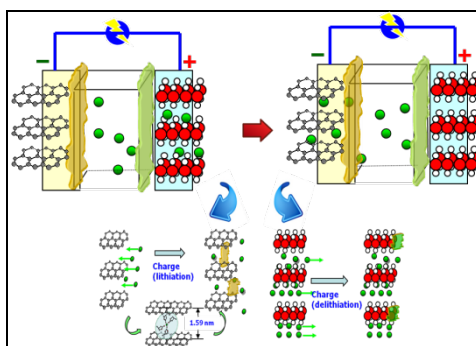

Figure 1. Basic schematic showing the transfer of lithium inside a lithium-ion battery cell. Lithium is shown traveling from the positive electrode to the negative electrode.

Over the past decade, chemists have begun to focus their attention on the electrolyte and the key role it plays in the performance of lithium-ion batteries. A good electrolyte must follow a few key criteria: it must be able to sufficiently dissolve salts, it should have low viscosity, it should not interact chemically or electrically with other cell components, and it should remain a liquid in a wide range of temperatures. Through extensive experimentation, scientists have found that the most acceptable electrolyte is a solution of carbonates. These compounds work well for this system because they don't contain an active proton, rendering them chemically inert in the heavily reducing and oxidizing environment. Also, carbonates contain a polar carbonyl group allowing them to dissolve sufficient amounts of lithium salts. Normal electrolyte solutions of carbonates consist of a cyclic carbonate and an acyclic carbonate. The cyclic compounds tend to have a high polarity and high viscosity, while the acyclic compounds are weakly polar and less viscous. Cyclic carbonates generally have a dipole moment >4.0 D; by comparison, water (which

is considered a good solvent because of its polar properties) has a dipole moment of 1.85 D. The cyclic compounds also have more intramolecular strain and form conformations that allow for better molecular dipole alignment, the more open/flexible structures of the acyclic compounds allow for a mutual cancellation of the dipoles. The industry standard electrolyte is a 30:70 solution of ethylene carbonate (EC) and ehtylmethyl carbonate (EMC) with $LiPF_6$ as an electrolyte solute. (See table 1 for EC and EMC structure and characterization data.)

Table 1. Structure and characterization data for EC and EMC. Notice the difference in the dielectric constant (ε) and the dipole moment.

Solvent	Structure	M. Wt	$T_m/{}^\circ C$	$T_b/{}^\circ C$	η/cP 25 °C	ε 25 °C	Dipole Moment/debye	$T_f/{}^\circ C$	d/gcm^{-3}, 25 °C
EC		88	36.4	248	1.90, (40 °C)	89.78	4.61	160	1.321
EMC		104	-53	110	0.65	2.958	0.89		1.006

In the lithium-ion battery environment, lithium forms a solvation shell with the surrounding solvent molecules as it is dissolved. As the battery cycles, the potential drops along the cell and the lithium-solvent complex migrates into the graphite sheets and begins the intercalation process. As intercalation begins, the graphite sheets expand to accommodate the lithium-solvent complex. When the lithium molecules are reduced, these graphite sheets collapse back to almost their original spacing. The solvent molecules that are decomposed in this process react on the surface and form a film around the anode. This film is commonly referred to as the solid electrolyte interface or SEI (figure 2). It prevents further decomposition of solvent molecules by acting as a barrier; however, the film is also permeable to lithium ions, allowing it to conduct ions. The fact that the SEI is acting as a barrier for solvent protection and an ionic conductor is key to the reversibility of the lithium-ion battery system. The SEI generally forms on the surface of graphite as the potential drops below about 1 V, its mechanism is widely known and accepted. At higher voltages, a passivation layer also forms on the cathode, which serves a similar purpose to the film formed on the anode. However, its formation mechanism is poorly understood.
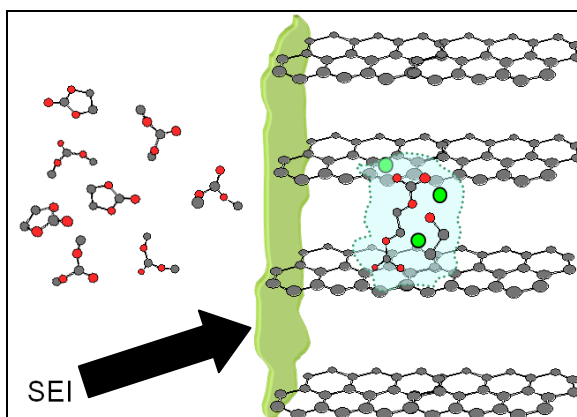

SEI

Figure 2. SEI on the surface of a graphite anode. Solvent molecules are decomposing in the graphite sheets following the intercalation process.

Studying the SEI and its effect on the lithium-ion battery system has been at the forefront of the field for years now. Manipulating the passivation films on both electrodes and figuring out ideal conditions to form durable and stable SEI are paramount to the progression of lithium-ion technology. Chemical additives used in liquid electrolytes can alter the chemistry of the SEI on the surface of each electrode. These additives have been proven to promote more stable SEI formation and drastically improve battery performance, especially at higher voltages.

One of the previous compounds used to manipulate cathode SEI chemistry was hexafluoro isopropyl phosphate (HFiP). As shown in figure 3, without any additives, after 80 cycles the battery loses 0.5 mAh of capacity. However, when HFiP is added, after 80 cycles the battery loses <0.1 mAh of capacity. From this study it is clear that HFiP has a beneficial effect on the stability of the battery system. Because of its ability to form a more stable and durable SEI on the cathode, the battery loses less capacity over time. The fully fluorinated version of this phosphate, perfluoro-t-butyl phosphate, outperformed HFiP in certain systems.
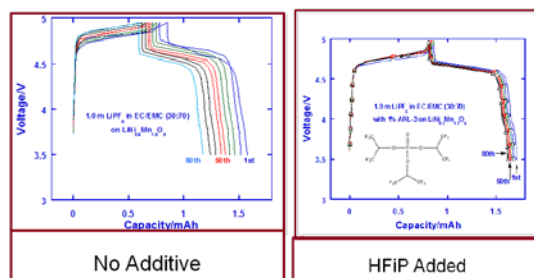
Figure 3. Battery cycling data of the standard electrolyte without an additive and with HFiP added. Notice the drastic difference in capacity lost after 80 cycles.

Boron-based additives have shown promise as SEI-promoting additives and, similar to the phosphates, form more stable SEI on the surface of both electrodes. Previous boron compounds tested were lithium bis(oxalate) borate (LiBOB) and lithium difluoro (oxolato) borate (half BOB) (figure 4).
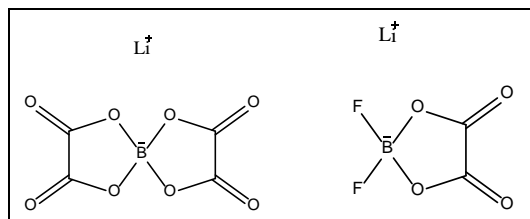

Figure 4. Structures for LiBOB (left) and half BOB (right).

2. Methods

After scientists found success using phosphate additives to promote more beneficial SEI formation, the idea came about to combine components from phosphorus systems with known boron compounds to test if such an arrangement could also help the development of the SEI. For this experiment, it is desired to combine the borate core from the boron compounds and the fluoroalkyl ligands from the phosphate compounds. In principle, this would make a fully fluorinated borate compound.

The synthesis of the compound began with 0.64 mol of perfluoro-t-butanol (figure 5), which created the fluoroalkyl ligands for the final compound. Diethyl ether was added and used as a solvent throughout the process. In order to form lithium perfluoro-t-butoxide, 151.6 g of LiH was added to the alcohol. The LiH was added cautiously in a closed vessel because of the volatile and exothermic nature of this reaction. The ionic interaction between lithium and the fluorinated alkyl group is weak; when the opportunity arises, the electron-rich oxygen will attempt to form a covalent bond. So to take advantage of that scenario, BCl_3 was slowly introduced into the reaction mixture. As the alkoxide reacts with BCl_3, the chlorines react with the lithium associated with the alcohol, forming insoluble lithium chloride (LiCl) and yielding the final borate product. Figure 6 shows the synthesis of perfluoro-t-butyl borate.
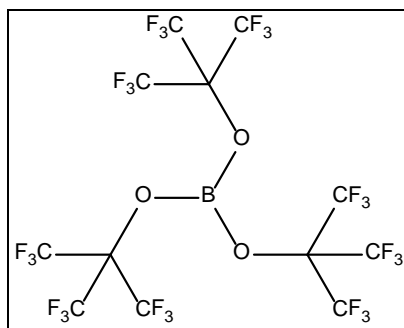
Figure 5. Structure of the target compound perfluro-t-butyl borate. The compound combines the borate core from the boron compounds with the fluroalkyl ligands from the phosphates.
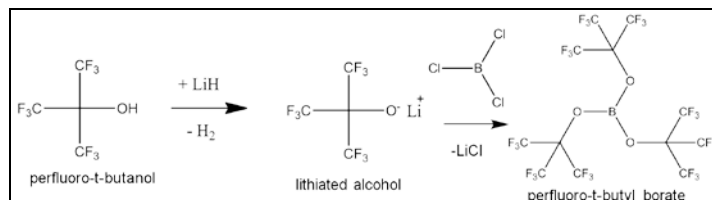

Figure 6. Synthesis map detailing the synthesis of perfluoro-t-butyl borate.

Once synthesized, the product was purified. First, there was an abundance of the solid side product LiCl, which was removed via vacuum filtration using a Büchner funnel. The filtrate contained the desired product and was prepped for further purification. This filtrate contained diethyl ether that was used as the inert reaction solvent during the lithiation process. In order to drive off the ether, the solution was distilled. The melting point of perfluoro-t-butyl borate is believed to be close to that of the ether (~34.6 °C), so the heating was done in a closed environment to prevent losing the desired product. Once the solvent was distilled, the remaining product was sublimated to obtain the highest purity. At least two sublimations of the final compound are ideal; however, due to particularly low yields (<1%), this was not possible.

Once the product had undergone the necessary purification steps, it was characterized using standard techniques including FTIR, mass spectrometry, boron/fluorine nuclear magnetic resonance, and differential scanning calorimetry. Also, 5 mM of the sample was placed in the standard industry electrolyte and went through rigorous battery testing.

3. Results

The compound was first characterized using FTIR (figure 7). The bond stretches that are of particular interest are C–F (1000–1400 strong), B–O (1154 strong), C–O (1000–1300 strong). All of the bonds of interest have representation in the IR spectra, and there is heavy activity in the 1000–1400 region where all of these bond stretches are located. In particular, there is a peak at 1160 that is close to the wave number indicative of B–O. The presence of these bonds in the IR spectra alludes to the expected final compound. However, possible contaminants were considered as well. The most likely contaminant is unreacted BCl_3—the B–Cl bond typically shows activity around 980. FTIR shows a strong peak around 980, thus implying some BCl_3 contamination. Another possible contaminate is boron reacting with fluorine; however, the FTIR shows no significant evidence of B–F (2300–2400 weak) contamination. Although an unexpected contamination presented itself, the peak at 3600 is indicative of a B–OH bond. This occurred because the sample was transported out of a dry environment and into the atmosphere in order to run the FTIR. During this transportation process, the compound must have hydrolyzed with water in the atmosphere, resulting in the boron hydroxyl bond.
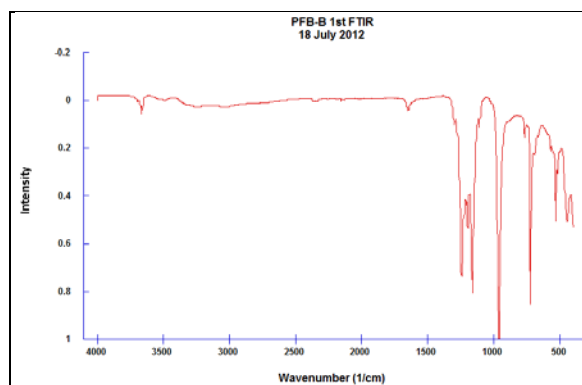
Figure 7. FTIR data for the compound yielded from the first synthesis.

A second synthesis of the compound was performed; however, there was a key difference in the procedure. For the first synthesis, distillation was used as a means of safely driving off the solvent without losing product. During the second synthesis, this process was used again; however, instead of only driving off the solid, there were also clear crystals that appeared in the receiving flask. The distillation was halted, and the product in the receiving flask (distillate) was sublimated independently from the compound in the reaction flask (sublimate). Both of these compounds were characterized separately through FTIR and directional scanning calorimetry (DSC).

FTIR for the distillate is comparable to that of the product from the first synthesis (see data in figure 8). Activity between 1000–1400 is indicative of all of the bonds of interest in the compound. However the peak at 980 is still present, meaning there is still significant unreacted BCl_3 in the final product. What is unique to the spectra of the distillate is a peak at 1400.
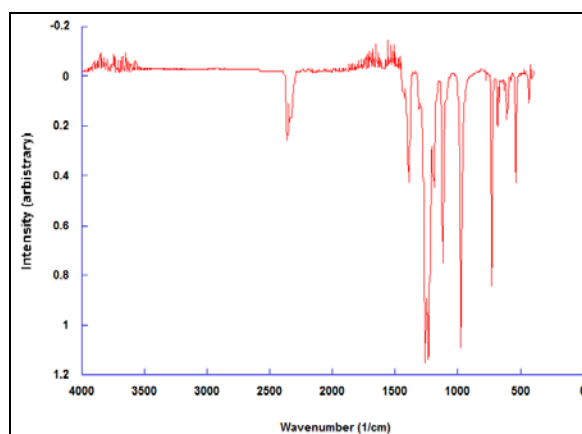
Figure 8. FTIR data for the distillate.

DSC data for the distillate shows a distinct melting point at 26°C (figure 9). This property is encouraging because it is similar to HFiP. However, mild melting at around 8 °C indicates that there are some impurities that have a different melting point than $B(PFB)_3$. The compound also has a supercooling property, which is evident from its strong freezing peak at –2 °C.
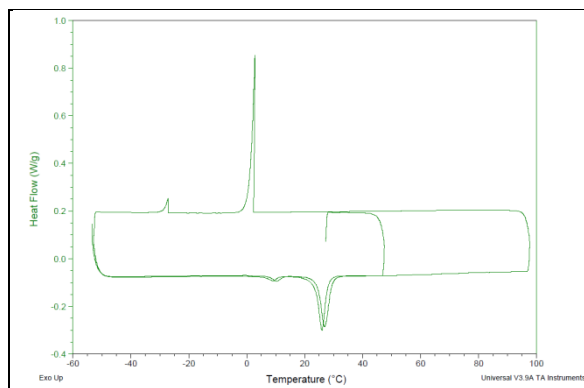
72

Figure 9. DSC data for distillate.

FTIR data for the sublimate is again comparable to the first synthesis, including the impurities (figure 10). However, this compound does not show the same peak at 1400 that was present in the distillate.
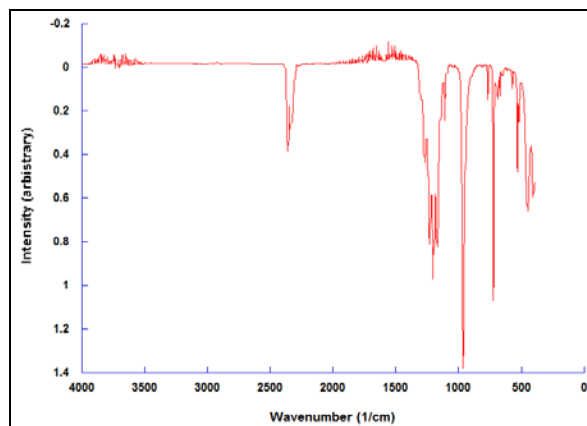

Figure 10. FTIR data for the sublimate.

DSC data for the sublimate suggests that this compound is entirely different from the distillate (figure 11). There is a small heat change at about 10 °C, but nothing appears at 26 °C where the distillate showed an intense melting point. It also does not have the same supercooling property present in the distillate, further suggesting that these compounds are not the same.

73
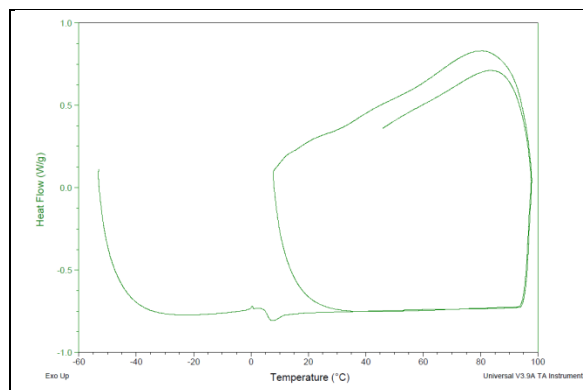
Figure 11. DSC data for the sublimate.

Mass spectrometry was done on the distillate with acetonitrile as the solvent. Figure 12 shows that quite a few peaks appear on the spectra. While it is not possible to assign explicit formulas to each fragment peak, there are explanations for the three most intense peaks on the spectra (figure 13).
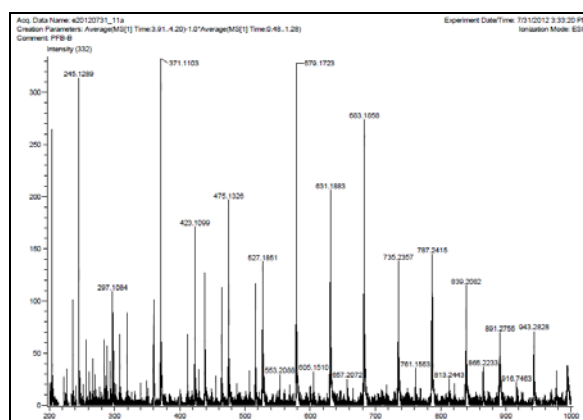
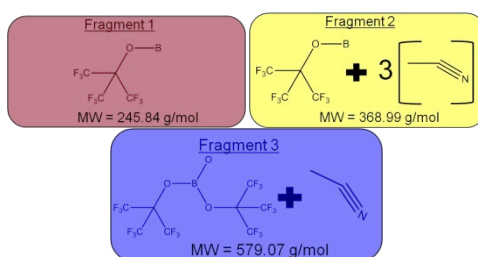

Figure 12. Mass spectra of the distillate.

Figure 13. Explainable fragments for FTIR.

The molecular weight of fragment 1 corresponds perfectly with the peak at 245. Fragment 2 has this same structure coupled with 3 moles of acetonitrile; if this fragment were to interact with two protons, then it perfectly explains the peak at 371. Fragment 3 is very encouraging because it includes the entire borate core with two fluoroalkyl ligands. This means that the borate core is

definitely intact in this compound, and that despite the contamination, the target compound is present in this product.

Despite impurities, the battery was tested to see how well it retains capacity during typical charge/discharge life cycle testing. The battery holds up well; the cycling data for the additive is shown in figure 14 and compared to the standard electrolyte with no additive. Although the additive begins with a lower capacity and does not demonstrate a better capacity for 100 cycles compared to the standard, the cell with the additive degrades less over time. Its capacity holds up well past 200 cycles, while the standard electrolyte rapidly loses capacity. Keeping in mind that this compound is very impure, this early battery data is encouraging.
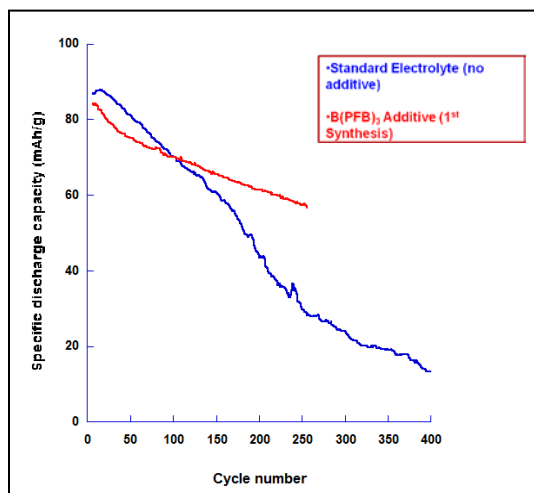
Figure 14. Battery test data of the product from the first sublimation.

4.   Conclusion

This preliminary work with $B(PFB)_3$ was intended to answer two main questions: Can we synthesize the compound, and if so, does it work in a battery? The latter question can be answered affirmatively. Battery test data shows that the additive does increase the battery's ability to maintain capacity over multiple cycles. However, the first question still remains to be answered. Although initial spectroscopy is fairly promising, the synthesis is unlike any additive seen previously. The spectra continue to be marred by unreacted BCl_3 and other contaminants. The process is also plagued by very low yields. These could be natural problems with this reaction; if so, the decision will have to be made whether this additive performs well enough in batteries to outweigh its synthetic issues. From initial battery tests, $P(PFB)_3$ has indicated that it performs well enough to warrant cleaning up the synthetic technique in order to see if these problems can be rectified.

INTENTIONALLY LEFT BLANK.

U.S. Army Research Laboratory

Electrochemical Characterization of Riboflavin-Enhanced Reduction of Trinitrotoluene

JAMES J. SUMNER AND KEVIN CHU
MENTORS: ARTHUR VON CRESCE AND KANG XU
SENSORS AND ELECTRON DEVICES DIRECTORATE
ADELPHI, MD

Communication

Electrochemical Characterization of Riboflavin-Enhanced Reduction of Trinitrotoluene

James J. Sumner [1],* and Kevin Chu [1,2]

[1] United States Army Research Laboratory, RDRL-SEE-O, 2800 Powder Mill Road, Adelphi, MD 20873, USA; E-Mail: kevin.chu.ctr@mail.mil

[2] Department of Biomedical Engineering, Washington University, Saint Louis, MO 63130, USA

* Author to whom correspondence should be addressed; E-Mail: james.j.sumner4.civ@mail.mil; Tel.: +1-301-394-0252; Fax: +1-301-394-0310.

Abstract: There is great interest in understanding trinitrotoluene (TNT) and dinitrotoluene (DNT) contamination, detection and remediation in the environment due to TNT's negative health effects and security implications. Numerous publications have focused on detecting TNT in groundwater using multiple techniques, including electrochemistry. The main degradation pathway of nitrotoluenes in the environment is reduction, frequently with biological and/or photolytic assistance. Riboflavin has also been noted to aid in TNT remediation in soils and groundwater when exposed to light. This report indicates that adding riboflavin to a TNT or DNT solution enhances redox currents in electrochemical experiments. Here AC voltammetry was performed and peak currents compared with and without riboflavin present. Results indicated that TNT, DNT and riboflavin could be detected using AC voltammetry on modified gold electrodes and the addition of riboflavin affected redox peaks of TNT and DNT. Poised potential experiments indicated that it is possible to enhance reduction of TNT in the presence of riboflavin and light. These results were dramatic enough to explain long term enhancement of bioremediation in environments containing high levels of riboflavin and enhance the limit of detection in electrochemically-based nitrotoluene sensing.

Keywords: trinitrotoluene; dinitrotoluene; reduction; riboflavin; bioremediation; AC voltammetry

1. Introduction

There is great interest in understanding trinitrotoluene (TNT) and dinitrotoluene (DNT) contamination, detection and remediation in the environment due to TNT's negative health effects as well as security implications [1,2]. Current protocols used for field analysis include colorimetric and immunoassay techniques that require skilled technicians collecting samples and processing them in a controlled environment for the best results [3,4]. The protocols are not particularly sensitive as they are only designed to detect the drinking water health advisory level of 2,000 ppm however, these procedures are costly to implement due to the fact they take significant amounts of time as samples must be collected in the field and transported to a laboratory for analysis. Electrochemistry offers and interesting alternative to other methods as instruments are traditionally low-cost, rugged, and easily engineered to be portable. Modern blood glucose monitors are an excellent example of these characteristics. Nitroaromatics have been studied using electrochemistry extensively over the past few years with multiple published techniques to analyze DNT and TNT with limits of detection near 10 ppb [5-10]. While this is of interest, to compete with high performance liquid chromatographic techniques for analysis of environmental samples of nitroaromatic compounds the limit of detection needs to be decreased by another one to four orders of magnitude [11-13].

Remediation is another large area of interest when studying nitroaromatics in the environment. Techniques studied have included bioremediation, photocatalysis and electrochemistry [14-19]. Riboflavin, or vitamin B2, has been reported to aid in TNT reduction in remediation experiments set to simulate soils and groundwater [20-22]. These experiments employed riboflavin spiked into reaction vessels exposed to sunlight or broadband UV/visible light sources. This exposure to light as well as riboflavin was required to have a significant enhancement of TNT reduction. While the electrochemical characterization of riboflavin has been examined to a lesser extent, recent publications validate the electrochemistry studied here [23,24]. The enhancement of the electrochemical signal of riboflavin could also be useful in studying this coenzyme composition for its effects on metabolism, nutrition and as a photosensitive agent [24,25].

It was postulated that TNT redox activity should be able to be enhanced by adding riboflavin and exposing it to a broad band light source. This would be useful to understand mechanisms in the simulated environmental samples reported in the remediation literature [20-22] as well as provide a means to increase the sensitivity of electrochemically-based sensors for nitroaromatics.

Experiments were performed using AC voltammetry and comparing peak currents with and without riboflavin as well as exposure to broadband light. Results indicated that DNT, TNT and riboflavin could be detected independently using AC voltammetry on self-assembled monolayer (SAM), modified gold electrodes. The exposure of nitroaromatic analytes to riboflavin and light affected redox peaks of TNT and DNT. Poised potential experiments were also performed in the presence of riboflavin and light to demonstrate that it is possible to enhance reduction of TNT over time. These results were dramatic enough to help explain long term enhancement of remediation of TNT in environments containing high levels of riboflavin as well as a way to enhance the limit of detection of electrochemically-based TNT sensors.

2. Experimental Section

2.1. Materials and Instrumentation

The electrolyte was sodium perchlorate, obtained from Aldrich, prepared as a 1 M aqueous solution. Stocks of the analytes 2,4,6-trinitrotoluene (Chem Service, West Chester, PA, USA) and 2,4-dinitrotoluene (Sigma-Aldrich, St. Louis, MO, USA) were prepared at a concentration of 10,000 ppm in acetonitrile. Those stocks and riboflavin (Sigma-Aldrich, St. Louis, MO, USA) were diluted in the electrolyte in concentrations from 10 to 1,000 ppb for analysis. Thiol-terminated alcohols (mercaptobenzoic acid, cystamine, mercaptoethanol, mercaptopropanol and mecaptohexanol, all from Aldrich) for self-assembled monolayer (SAM) formation on the gold electrodes were prepared as 1 mM ethanolic solutions. Electrodes were voltammetrically stripped prior to SAM formation using 0.5 M sulfuric acid diluted from concentrated stock obtained from Fisher and then they were polished sequentially with 1.0, 0.3 and 0.05 micron alumina, sonicating after each polishing step. All water was purified using a Barnstead EasyPure RF to 18 MΩ cm.

The electrochemical cell was a three electrode configuration using a 2 mm diameter SAM-modified gold disk electrode as the working electrode, Ag/AgCl reference electrode, and platinum wire counter electrode all obtained from CH Instruments (Austin, TX, USA). All electrochemical experiments were carried out using a CH Instruments model 660a electrochemical workstation. Broadband light was provided by a 75 W 120 V halogen bulb placed 30 cm from the electrochemical cell.

2.2. Methods

SAM-modified electrodes were prepared by voltammetric stripping and polishing of the electrode followed by soaking in a 1 mM ethanolic solution of the respective mercapto-alcohol overnight. Most procedures used AC voltammetry at 10 Hz with a potential sweep between 0.3 V and −0.8 V. The sweep was performed as 4 mV steps with a measurement time of 2 s per step. A background scan of each electrode was performed in order to verify SAM formation before the addition of TNT or riboflavin. Either TNT or riboflavin was titrated into the electrochemical cell at concentrations from 10 to 1,000 ppb and ac voltammetric sweeps were performed at least three times to insure a stable response. The final experiments on each electrode involved introducing 10–1,000 ppb of the analyte to the solution not previously present (either the TNT or riboflavin) to evaluate any enhancement. In experiments with light exposure, the electrochemical cell was illuminated only during the voltammetric sweep.

Removing the polymer generated by the reduction of nitroaromatics from the modified working electrode was much easier than bare electrodes however it was still a multistep process. It required electrochemical stripping in 0.5 M H_2SO_4 sweeping from 0 V to 1.0 V using cyclic voltammetry. After electrochemically stripping the electrode, it was polished sequentially using 1 μm, 0.3 μm, and 0.05 μm alumina sonicating between each step and prior to placing in the ethanolic mercaptohexanol solution for preparation of a fresh SAM.

3. Results and Discussion

3.1. Electrochemistry of TNT, DNT and Riboflavin

The reduction mechanism of the nitroaromatics, TNT and DNT has been described in previous work [5,7,19]. Both species tend to use the electron deficient nitrogen groups as electron acceptors and upon applied potential will be reduced from nitro, to hydroxylamine and subsequently to amine functionalities. The reaction sequence in Scheme 1 is based on the work of Grigoriants *et al.* described in [7] and agrees with the recent literature [5,19]. This figure shows this reduction of TNT as a three step process to describe the three redox peaks generated in the voltammetry.

> **Scheme 1.** Schematic of the reduction of TNT as a three step process explaining the three peaks generated in voltammograms.
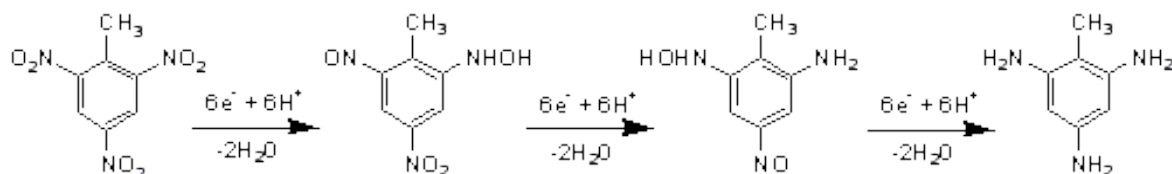
When TNT or DNT are reduced and aromatic amines are formed it is possible to further reduce these species to azides. These aromatic azides can then polymerize onto the electrode surface [26-28]. This polymerization blocks the electrode surface and makes obtaining reproducible results difficult as well as makes the surface very difficult to clean. To prevent this issue the working electrode was modified with a self-assembled monolayer. The intent of this monolayer was not only to make the surface easier to clean after nitroaromatic analysis but also to provide a broader potential window in which to scan the gold working electrode. Several monolayers were examined including mercaptobenzoic acid, cystamine, mercaptoethanol, mercaptopropanol and mercaptohexanol. Mercaptohexanol was the only monolayer which packed well enough to protect the electrode surface, however, due to the length it was necessary to run ac voltammetry at very low frequencies (1 to 10 Hz) in order to not outpace the electron transfer kinetics.

All subsequent data shown was collected using a mercaptohexanol modified gold working electrode. Figure 1 shows the ac voltammetry of neat aqueous preparations of (a) TNT, (b) DNT and (c) riboflavin. The frequency was 10 Hz, amplitude 25 mV and the sweep was performed in 4 mV steps. Each analyte was examined independently by first interrogating with a blank followed by titrations to yield total concentrations of 10, 100, and 1,000 ppb in aqueous 1 M sodium perchlorate. Each scan plotted represents an average of three voltammetric sweeps. In this study, when there was no exposure to riboflavin or light, TNT showed three significant redox peaks at 1,000 ppb without background subtraction. DNT was more sensitive showing two distinct redox peaks at 100 ppb. Riboflavin did not exhibit redox activity until concentrations reached 1,000 ppb with a sharp peak at ~−0.45 V, the dominate structure in these scans of riboflavin is a background peak due to the SAM-modified electrode.

Figure 1. AC voltammograms of the electrode response to titrations of (**a**) TNT, (**b**) DNT and (**c**) riboflavin. The plots show a blank, 10 ppb, 100 ppb and 1,000 ppb of each analyte in 1 M sodium perchlorate electrolyte with a mercaptohexanol SAM-modified working electrode.
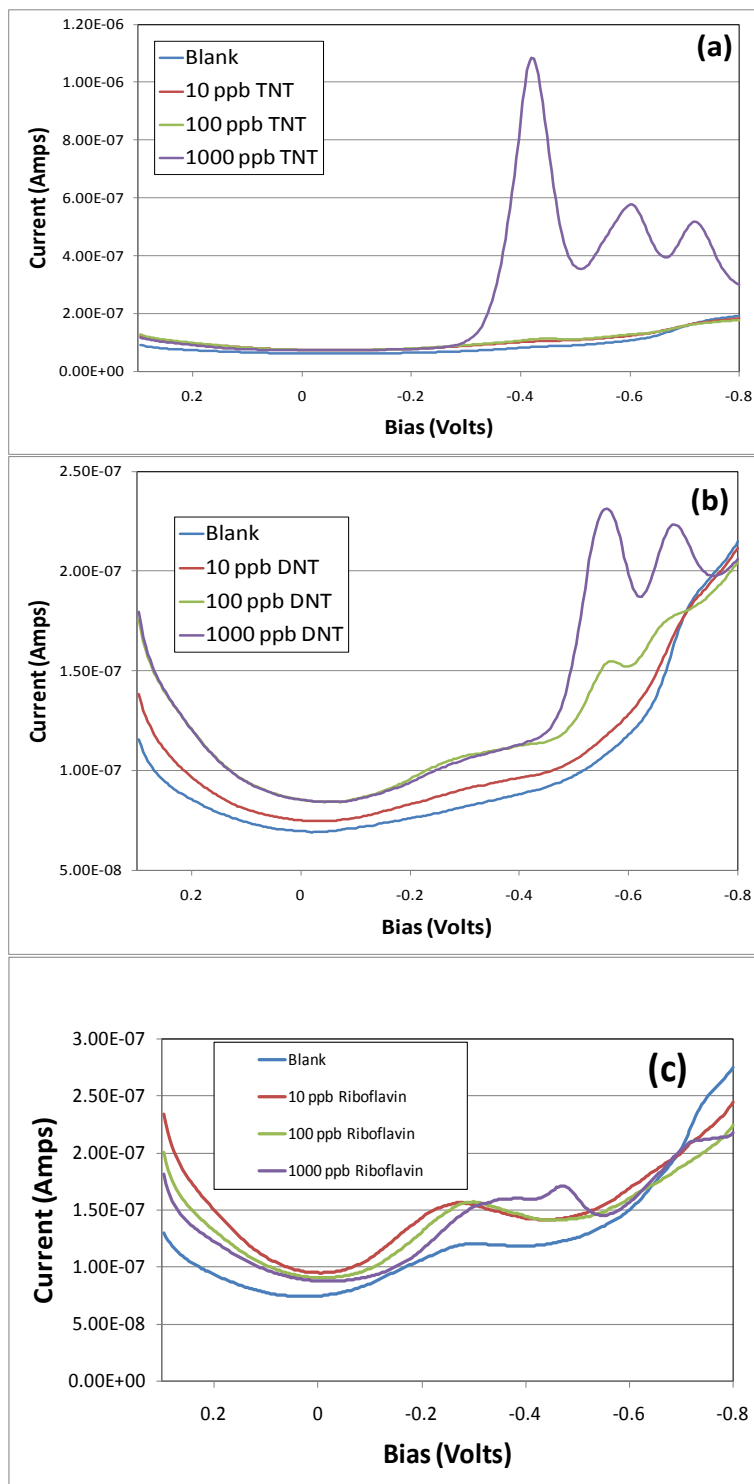
3.2. The Effects of Riboflavin on the Electrochemistry of TNT and DNT

With reports in the literature describing riboflavin-enhanced reduction of TNT in simulated ground water and soils [20-22] it was postulated that the effect on electrochemistry should be evaluated.

Reports also indicated that the reduction of TNT was further enhanced by exposure to light. A complicating factor to the analysis of enhanced reduction of TNT in this system is that first redox peak for TNT and the redox peak for riboflavin appear at a very similar bias *versus* Ag/AgCl however, Figure 2 demonstrates this enhancement for both (a) TNT and (b) DNT with riboflavin present. These example scans show a titration of TNT or DNT from 0 to 1,000 ppb with the electrochemical cell exposed to light as well as having the working electrode pretreated in a solution of 1,000 ppb riboflavin in 1 M sodium perchlorate. This pretreatment was achieved simply by performing ac voltammetric scans in the presence of riboflavin prior to exposure to TNT or DNT. Note that three distinct redox peaks can now be seen at concentrations of 10 ppb of TNT without background subtraction. While the DNT does not show increased peak currents there appears to be a shift to combine the riboflavin peak with some contributing electrons from the first DNT peak which could explain reported enhanced reduction in environmental samples.

Figure 2. AC voltammograms of the electrode response to the analytes (a) TNT (0–1,000 ppb) exposed to 1,000 ppb riboflavin and (b) DNT (1,000 ppb) with and without exposure to 1,000 ppb riboflavin. Note that the DNT only produced 2 redox peaks while the 1,000 ppb riboflavin exposed DNT produces a significantly larger peak at ~0.45 V than that of TNT or riboflavin alone.
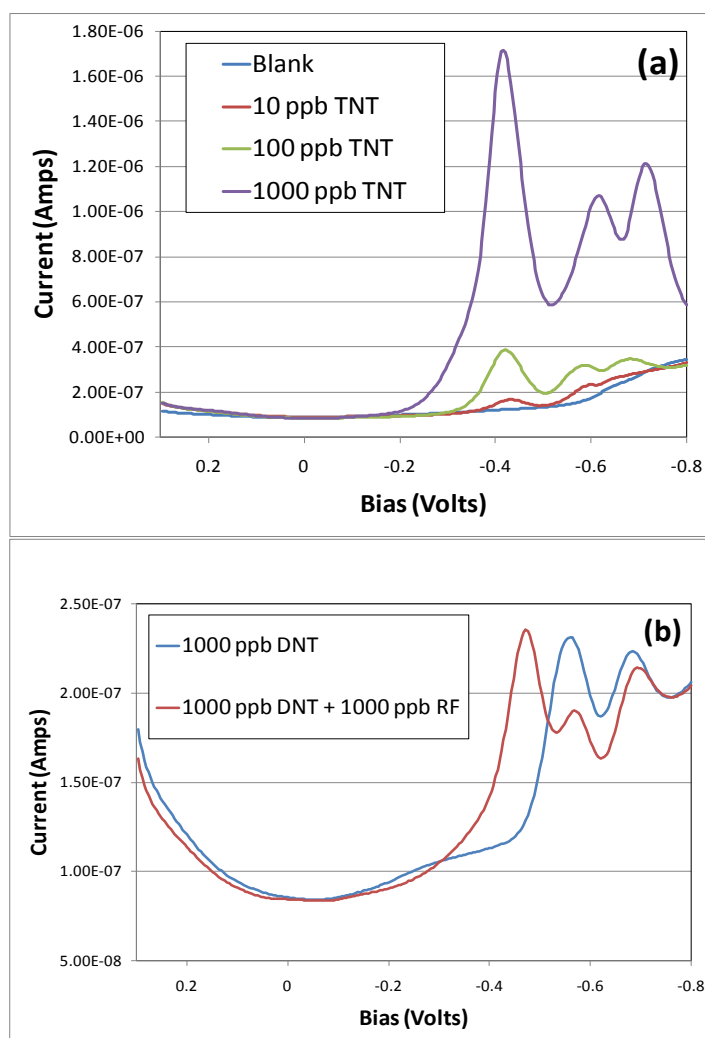
Figure 3 shows the ac voltammograms of the electrode response to TNT while controlling exposure to riboflavin and light. Each scan is an average of three separate experiments. While each of these scans included equal concentrations of TNT and riboflavin, 1,000 ppb each, there were two main differences. One was whether the electrochemical cell was exposed to light or not and if the electrode was first pretreated with riboflavin or if the riboflavin and TNT were added simultaneously.

Figure 3. AC voltammograms are presented of electrode response based on exposure to light and electrode pretreatment with riboflavin. These samples all contained both 1,000 ppb TNT and 1,000 ppb riboflavin. Traces marked with RF were pretreated by running three ac voltammograms with 1,000 ppb riboflavin before exposure to TNT. Samples were also measure either in a closed faraday cage to block light or exposed to light. The lowest peak current at ∽−0.45 V is TNT not exposed to light nor pretreated with riboflavin ("Dark"). The highest peak current is exposed to light and pretreated with riboflavin ("Light, RF").
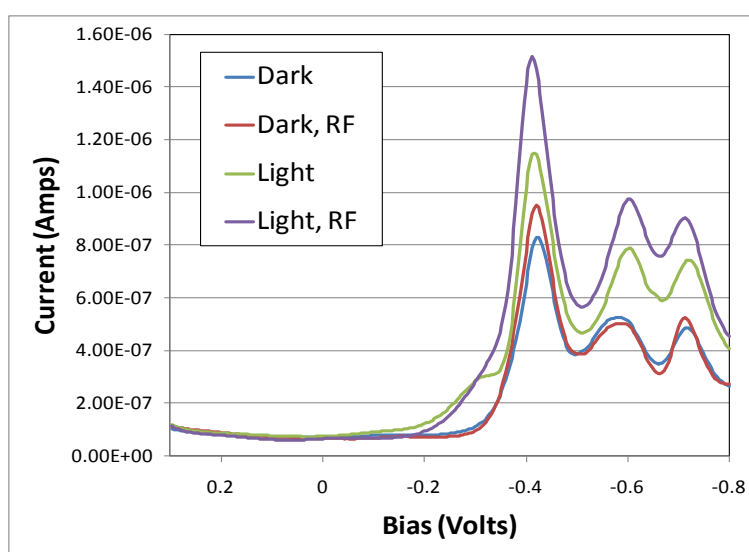
In the data indicated with the labels "RF" in Figure 3, the electrodes were first exposed to 1,000 ppb riboflavin and the ac voltammograms swept three times prior to the addition of 1,000 ppb TNT. The other two data series were exposed to TNT and riboflavin simultaneously. Note that the samples exposed to light and pretreated with riboflavin showed a significant enhancement over measurements performed in a similar matter to previous reports (the trace labeled "Dark"). Figure 4 shows this enhancement and its reproducibility by plotting the average and standard deviation of six independent experiments for both the fully enhanced ("Light, RF") and the control ("Dark"). The shoulder on the voltammogram labeled "Light" appears to be due to riboflavin.

Poised potential experiments were performed to determine if irreversible reduction of the TNT in the electrochemical cell could be achieved with the assistance of riboflavin. The total volume of electrolyte was reduced to 2 mL in these experiments and each potential was held for 10 min followed by collecting an AC voltammogram. Figure 5 shows an example of this experiment. While the first redox peak showed only a slight change in total current the two subsequent peaks were diminished to an increasingly greater extent. Without riboflavin present all three redox peaks decreased by less than 10% under the poised potential experimental conditions.

Figure 4. This bar graph compares the reproducibility and enhancement of redox currents of TNT (at the peak current near −0.4 Volts) when exposed to light and riboflavin pretreatment. These are an average and the error bars show a standard deviation of six replicate electrodes. The enhancement is about 60% with the normal sensor having a peak current of 0.88 (σ = 0.12) microamps and the enhanced at 1.45 (σ = 0.11) microamps.
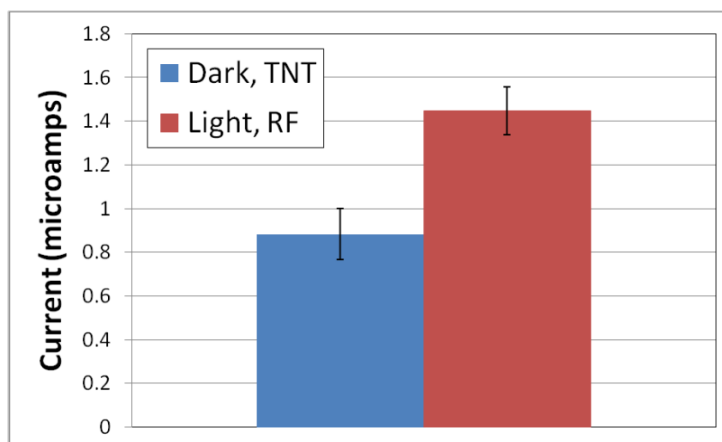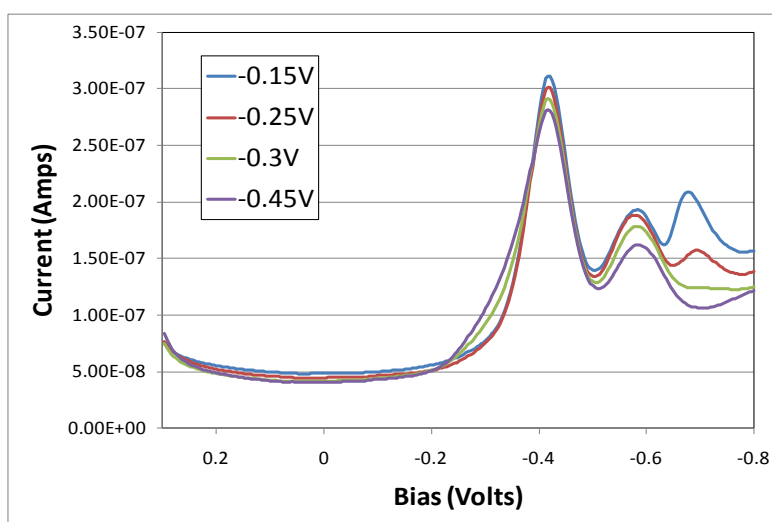

Figure 5. AC voltammograms collected after holding poised potential for 10 min at −0.15, −0.25, −0.30 and −0.45 V. Note that while the first redox peak had little change in peak current the two subsequent peaks were much more significantly affected.

4. Conclusions

This data suggests that riboflavin aids in the reduction of TNT, and thus makes TNT easier to detect and remediate in aqueous environments. While reproducibility can be a challenge, problems can be mitigated using mercaptohexanol, SAM-modified working electrodes. Exposing riboflavin working electrodes to broadband light enhanced redox peaks by 60% over the techniques similar to those previously reported. Further work is necessary to verify that these results would translate to environmental samples. It is possible that there would be compounds in the real world samples that could interfere with the electrochemistry. This data indicates that riboflavin, under these conditions, is capable of transferring electrons to nitroaromatics. Since the redox potential of riboflavin is significantly

closer to zero volts, the energy required to reduce the riboflavin and thus reduce the nitroaromatic is significantly less. These results were dramatic enough to explain long term enhancement of bioremediation for nitro aromatics in the environment containing high levels of riboflavin as well as enhance the limit of detection in electrochemically-based TNT sensing.

Acknowledgments

References

1. Holtoff, E.L.; Stratis-Cullum, D.N.; Hankus, M.E. A nanosensor for TNT detection based on molecularly imprinted polymers and surface enhanced raman scattering. *Sensors* **2011**, *11*, 2700-2714.

2. Houston, J.G.; Lotfu, G.R. Dietary exposure of flathead minnows to the explosives TNT and RDX and to the pesticide DDT using contaminated invertebrates. *Int. J. Environ. Res. Public Health* **2005**, *2*, 286-292.

3. Crockett, A.B.; Craig, H.D.; Jenkins, T.F.; Sisk, W.E. *Field Sampling and Selecting On-Site Analytical Methods for Explosives in Soil*; Report #EPA/540/S-97/501; United States Environmental Protection Agency: Las Vegas, NV, USA, 1996.

4. Crockett, A.B.; Craig, H.D.; Jenkins, T.F. *Field Sampling and Selecting On-Site Analytical Methods for Explosives in Water*; Report #EPA/600/S-99/002; United States Environmental Protection Agency: Las Vegas, NV, USA, 1999.

5. Bozic, R.G.; West, A.C.; Levicky, R. Square wave voltammetric detection of 2,4,6-trinitrotoluene and 2,4-dinitrotoluene on a gold electrode modified with self-assembled monolayers. *Sens. Actuat. B* **2008**, *133*, 509-515.

6. Marinovic, V.; Marinovic, S.; Jovanovic, M.; Jovanovic, J.; Strbac, S. The electrochemical reduction of trinitrotoluene on a platinum wire modified by chemisorbed acetonitrile. *J. Electroanal. Chem.* **2010**, *648*, 1-7.

7. Grigoriants, I.; Markovsky, B.; Persky, R.; Perelshtein, I.; Gedanken, A.; Aurbach, D.; Filanovsky, T.; Felner, I. Electrochemical reduction of trinitrotoluene on core-shell tin-carbon electrodes. *Electrochem. Acta* **2008**, *54*, 690-697.

8. Goh, M.S.; Pumera, M. Graphene-based electrochemical sensor for detection of 2,4,6-trinitrotoluene (TNT) in seawater; the comparison of single-, few-, multilayer graphene nanoribbon and graphite microparticles. *Anal. Bioanal. Chem.* **2011**, *399*, 127-131.

9. Chen, T.W.; Sheng, Z.H.; Wang, K.; Wang, F.B.; Xia, X.H. Determination of explosives using electrochemically reduced graphene. *Chem. Asian J.* **2011**, *6*, 1210-1216.

10. Fu, X.C.; Chen, X.; Wang, J.; Liu, J.H.; Huang, X.J. Amino functionalized mesoporous silica microspheres with perpendicularly aligned mesopore channels for electrochemical detection of trace 2,4,6-trinitrotoluene. *Electrochem. Acta* **2010**, *56*, 102-107.

11. Hilmi, A.; Luong, J.H.T.; Nguyen, A.L. Determination of explosives in soil and ground water by liquid chromatography-amperometric detection. *J. Chromatogr. A* **1999**, *844*, 97-110.

12. Bratin, K.; Kissenger, P.T.; Briner, R.C.; Bruntlett, C.S. Determination of nitroaromatic, nitramine, and nitrate ester explosive compounds in explosive mixtures and gunshot residue by liquid chromatography and reductive electrochemical detection. *Anal. Chem. Acta* **1981**, *130*, 295-311.

13. Woltman, S.J.; Even, W.R.; Shlin, E.; Weber, S.G. Chromatographic detection of nitroaromatic and nitramine compounds by electrochemical reduction combined with photoluminescence following electron transfer. *Anal. Chem.* **2000**, *72*, 4928-4933.

14. Lenke, H.; Achtnich, C.; Daun, G.; Knackmuss, H.J. Bioremediation of TNT-contaminated soil. *Environ. Sci. Pollut. Control Ser.* **2000**, *22*, 561-578.

15. Palaniswamy, D.K.; Sorial, G.A.; Maloney, S.W. Electrochemical reduction of 2,4,6-trinitrotoluene. *Environ. Eng. Sci.* **2004**, *21*, 203-218.

16. Doppalapudi, R.B.; Sorial, G.A.; Maloney, S.W. Electrocehmical reduction of simulated munitions wastewater in a bench-scale batch reactor. *Environ. Eng. Sci.* **2002**, *19*, 115-130.

17. Actnich, C.; Lenke, H.; Klaus, U.; Spiteller, M.; Knackmuss, H.J. Stability of immobilized TNT derivatives in soil as a function of nitrogroup reduction. *Environ. Sci. Technol.* **2000**, *34*, 3698-3704.

18. Hwang, H.M.; Slaughter, L.F.; Cook, S.M.; Cui, H. Photochemical and microbial degradation of 2,4,6-trinitrotoluene (TNT) in a freshwater environment. *Bull. Environ. Contam. Toxicol.* **2000**, *65*, 228-235.

19. Schmelling, D.C.; Gray, K.A.; Kamat, P.V. Role of reduction in the photocatalytic degradation of TNT. *Environ. Sci. Technol.* **1996**, *30*, 2547-2555.

20. Yang, X.; Zhao, X.; Hwang, H.M. Phototransformation of 2,4,6-trinitrotoluene: Sensitized by riboflavin under different irradiation spectral range. *J. Hazard. Mater.* **2007**, *143*, 271-276.

21. Zeng, K.; Hwang, H.M.; Zhang, Y.; Cook, S. Assesing cytotoxicity of photosensitized transformation products of 4,4,6-trinitrotoluene (TNT) and atrizine with freshwater microbial assemblages. *Environ. Toxicol.* **2004**, *19*, 490-496.

22. Cui, H.; Hwang, H.M.; Cook, S.; Zeng, K. Effect of photosensitizer riboflavin on the fate of 2,4,6-trinitrotoluene in a freshwater environment. *Chemosphere* **2001**, *44*, 621-625.

23. Malinauskas, A. Electrochemical study of riboflavin adsorbed on a graphite electrode. *Chemija* **2008**, *19*, 1-3.

24. Zhang, H.; Zhao, J.; Liu, H.; Wang, H.; Liu, R.; Liu, J. Application of poly (3-methylthiophene) modified glassy carbon electrode as riboflavin sensor. *Int. J. Electrochem. Sci.* **2010**, *5*, 295-301.

25. Hagen, J.A.; Kim, S.N.; Bayraktaroglu, B.; Leedy, K.; Chavez, J.L.; Kelley-Loughnane, N.; Naik, R.R.; Stone, M.O. Biofunctionalized zinc oxide field effect transistors for selective sensing of riboflavin with current modulation. *Sensors* **2011**, *11*, 6645-6655.

26. Yousef, U.S.; Abdel-Azzem, M. A cyclic voltammetric and coulometric study of a modified electrode prepared by electrooxidative polymerization of nickel complex of 1,5-diaminonapthalene in acetonitrile. *Pol. J. Chem.* **1998**, *72*, 2583-2596.

27. Abdel-Azzem, M.; Yousef, U.S.; Pierre, G. A cyclic voltammetric and coulometric study of a modified electrode prepared by electrooxidative polymerization of 1,5-diaminonapthalene in aqueous acidic medium. *Eur. Polym. J.* **1998**, *34*, 819-826.

28. Abdel-Azzem, M. Electrooxidative oligomerization of 1,5-diaminonapthalene in acetonitrile medium. *J. Electroanal. Chem.* **1996**, *417*, 163-173.

Survivability/Lethality Analysis Directorate (SLAD)

INTENTIONALLY LEFT BLANK.

U.S. Army Research Laboratory
SUMMER RESEARCH TECHNICAL REPORT

Target Modeling for the U.S. Army Research Laboratory

MATTHEW SCHULZ
MENTOR: SCOTT HORNUNG
SURVIVABILITY/LETHALITY ANALYSIS DIRECTORATE
ABERDEEN PROVING GROUND, MARYLAND

Contents

List of Figures

Abstract

This paper documents and explains the experiences and knowledge I have accrued through my work at the Army Research Laboratory (ARL) while assigned to the Ground Mobile Branch (GMB) of the Survivability/Lethality Analysis Directorate (SLAD). This Branch is tasked with the role of providing modeling and simulation support through the ballistic analysis of current and future vehicular systems. This role has traditionally been accomplished using three-dimensional (3-D) BRL computer-aided design (CAD) target geometries and the MUVES vulnerability model. SLAD provides analysis results that impact vehicle evaluation and assessment, which can lead to modifications. These modifications ultimately increase the survivability of a particular system. I was assigned to SLAD's Target Modeling Team (TMT) and directly supported the development of target geometries. To achieve this, I participated in the vehicle measurement process using modern metrology equipment, produced component-level target geometries through a variety of CAD packages, and aided the geometry conversion process through part reconstruction and part facetization. This report details my efforts and the insights I have gained while serving as a target modeler for the GMB.

Student Bio

Mr. Schulz is a senior at the University of Maryland, Baltimore County, pursuing a B.S. in Mechanical Engineering. He has worked with the Ground Mobile Branch's Target Modeling Team for 3 years through both the Student Temporary Employment Program (STEP) and the Student College Experience Program (SCEP). Over the course of his employment as a target modeler, Mr. Schulz has produced a variety of visualization tools for post-event investigations and supported the collection of basic data for computer-aided design (CAD) target models from vehicle assets. Additionally, he has performed work in converting between various CAD formats and constructing and finalizing CAD target geometries for use in MUVES analyses. Upon graduation, Mr. Schulz hopes to utilize his engineering background by becoming a U.S. Army Research Laboratory civilian employee.

1. Introduction

The Survivability/Lethality Analysis Directorate's (SLAD's) Ground Mobile Branch (GMB) provides modeling and simulation support through building computer-aided design (CAD) representations and providing analysis results for current and future vehicular systems. This goal is accomplished using high-fidelity CAD target geometries and the MUVES-S2 (referred to as MUVES) vulnerability model. MUVES is a suite of programs designed to aid in predicting vehicle vulnerability by incorporating vehicle models, penetration algorithms, and a wide variety of other data relating to both the threat and target's performance. The results generated from the MUVES analyses impact vehicle assessment and evaluation, which can lead to design modifications that are intended to increase vehicle and crew survivability.

Because of the nature of GMB's mission and limited test-shot opportunities, emphasis is placed on analysis, which means much effort is devoted to developing the inputs necessary for quality MUVES analyses. The Target Modeling Team (TMT) develops and maintains the target geometry necessary to tie MUVES' vulnerability equations to the vehicle's geometry. (It should be noted that the U.S. Army Ballistics Research Laboratory Computer-Aided Design [BRL-CAD] is the only geometry format currently supported for MUVES analysis. All geometry that will be used in MUVES analyses must be either constructed natively in BRL-CAD or converted after construction on a commercial CAD package.)

GMB is currently involved in remodeling the M2A3 Bradley target geometry. I have participated directly in this project through my work on the TMT. My contributions include converting and reconstructing geometry through facetization and rebuilding techniques, aiding the reverse-engineering process by utilizing metrology equipment and techniques, and constructing component-level target geometries through a variety of CAD packages.

2. Methods, Assumptions, and Procedures

2.1 Target Modeling Introduction

Target modeling refers to the process of generating or preparing CAD models for use in MUVES and/or other analyses. The process for developing or preparing target models will vary according to situation. If the TMT is provided with geometry from either the vendor or an existing model in the target library, the process may be as straightforward as running the geometry through a conversion process or other preparations and updates as the analyst's needs dictate. If the geometry does not exist or the benefits of upkeep are outweighed by the benefits of rebuilding the model, the process will include reverse-engineering, as the geometry must be made "in-house."

The main tools used to develop target geometries are various CAD packages. Typically, modelers and vendors will have their own preferred package in which to model (*1*). The variety introduced by these preferences makes familiarity with all commonly used packages a necessity—the TMT uses approximately six different CAD packages over the course of standard operations with major packages including ProE, Rhino, Spaceclaim, and BRL-CAD.

2.2 Geometry Conversion

The largest part of the TMT's work deals with geometry conversion (the importing or exporting of geometries from one CAD format to another) and the difficulties it invokes. The ability to successfully and quickly perform these conversions is critical to GMB's mission because of the wide variety of CAD formats encountered by the TMT—as explained previously, this variety stems from a combination of target modelers using a variety of packages and the variety introduced though vendor-provided CAD. One consequence of converting geometry is that the TMT tends to develop two target models simultaneously: one in the commercial CAD package it is being modeled in (for use in various types of analyses) and one in BRL-CAD (for use in MUVES) as the commercial CAD parts are converted in. Unfortunately, the conversion process must be performed on a case-by-case basis. While generalizations may be made about what types of geometry will and will not present problems, the methods for resolving them are not always apparent.

Our primary conversion technique is part facetization. The purpose of facetization is to bring geometry in a commercial format into a form that BRL-CAD can read. When parts are facetized, the existing format, generally Non-Uniform Rational B-Splines (NURBs) for commercial CAD packages, is modified in such a way that it becomes a Bag of Triangles (BoTs) format. Essentially, this type of conversion replaces the existing geometry with a mesh of interlocking triangles.

Facetization, while generally fast, is not without drawbacks. The most commonly encountered issue is known as an overlap, and the source of the problem is explained through the "bolt analogy." In figure 1a, a simple bolt running through a generic solid cutout is displayed in its native format. A close-up of the bottom of this cutout is shown in figure 1b, which displays how the edge of the bolt and the edge of the solid meet perfectly. When this geometry is facetized, the edges no longer meet at the same points. Figure 2a displays the converted image of figure 1a, and figure 2b shows the converted image of figure 1b. The triangular mesh that replaces the original wireframe of the models cannot replicate the perfect circle that was originally modeled—the error this introduces causes certain sections of the bolt and the solid to overlap and occupy the same volume. Other common issues include model hierarchy and placement failing to be preserved and parts no longer meeting with flush edges, the former being inherent to the conversion process and the latter another consequence of the triangle mesh. All of the issues that the facetization process generates must be addressed before the geometry can be used as a MUVES input.
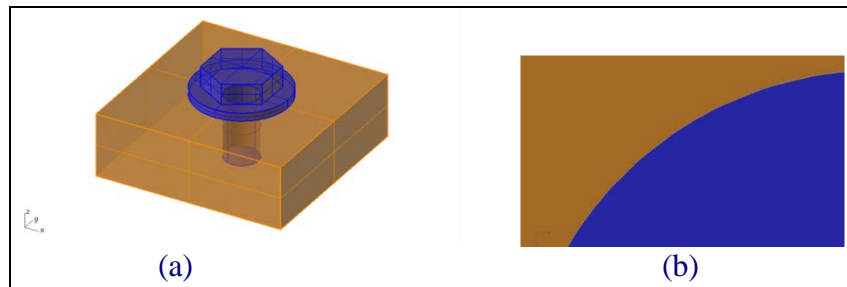
Figure 1. (a) A bolt going through a solid cutout in native format. (b) Close-up of the interface between the bolt and the bottom face.
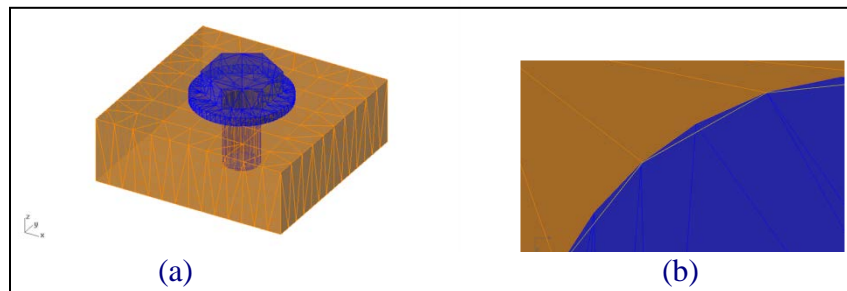

Figure 2. (a) Facetized geometry from figure 1a. (b) Facetized geometry from figure 1b. The line running through the blue section demonstrates the overlap between the solid's and bolt's volumes.

Another difficulty in facetizing parts is the difficulty in predicting when a part will fail to facetize—generally, such failures tend to result when the input geometry possesses complex surfaces, tight edges, or other difficult features. When these failures occur, there are only two options: either rebuild the part natively on the commercial model to facilitate better facetization or rebuild natively on the BRL-CAD model. Parts with sufficiently complex geometry will typically be rebuilt on the commercial model with simpler geometry because of the difficulty of modeling complex shapes natively in BRL-CAD.

A final issue with converting geometry from one format to another is accounting for any geometry changes that occur through modeling or modification to existing geometry—commercial format changes can be facetized to preserve symmetry in the BRL-CAD model, but no such method exists for exporting BRL-CAD geometry into commercial formats. If the BRL-CAD model is modified such that the change must be reflected in the commercial model, the only means of exporting that geometry is in a BOTs format. Most modern CAD packages have little to no means of interacting with geometry in this form, which means the imported geometry can be used for little more than a rough guide for size, shape, and basic dimensions. Because of the amount of work involved with the reconstruction conversion technique, it is generally undesirable because it adds more time to the conversion process than facetization for an equivalent transfer.

3. Reverse-Engineering Process

In any instance where required geometry either does not exist or is outdated (where updating would not be feasible), the TMT will reverse-engineer target geometry from existing vehicle assets. In order to begin this process, the intent of use for the target model must be identified; the type of analysis that is being performed will dictate how and what data will be collected. Radar signature analyses require highly accurate surface representations and may not need measurements involving plate thicknesses or internal part geometry as a MUVES ballistic vulnerability analysis would. In the previous comparison, the data collected for a radar signature analysis would likely take on the form of point-cloud data (an extremely dense collection of points derived from laser-based measurements), and the MUVES analysis would see data collected in the form of surface and edge curve data. Typically, the requirements of the GMB fall under the latter category.

The TMT uses a variety of tools and processes to both ease and shorten the data collection phase of reverse-engineering. Our primary tool in collecting data is known as a scanning arm (a Faro Arm® in this case), displayed in figure 3. It has a variety of heads and tips that are used to collect various types of data—laser "painting" heads scan surfaces as point cloud data and a variety of probe tips collect individual points and edges, stored respectively as points and splines (*2*). Target modelers will only collect the metadata and geometry necessary to develop a target model; any redundant or unnecessary data are ignored by utilizing the symmetry of the vehicle as much as possible. To overcome the physical limitations of the scanning arm, the TMT identifies a series of global reference points across a vehicle with a second machine, a theodolite (Sokkia® Total Station). With the theodolite, the entire set of reference points can be captured as one data set. This allows any data set the scanning arm collects to properly align and match up to the other data sets by providing a common coordinate system.

Figure 3. Faro Arm scanning device.
The mobile head captures
geometry in a coordinate system
relative to the immobile base.

A complete example of the data collection results is shown in figure 4. The lines displayed make up the edge and point data for the rear side of a Special Operations Command Mine-Resistant Ambush-Protection All-Terrain Vehicle (SOCOM MATV). As discussed previously, the sparse appearance of the splines results from collecting only the data necessary for completing the target geometry.
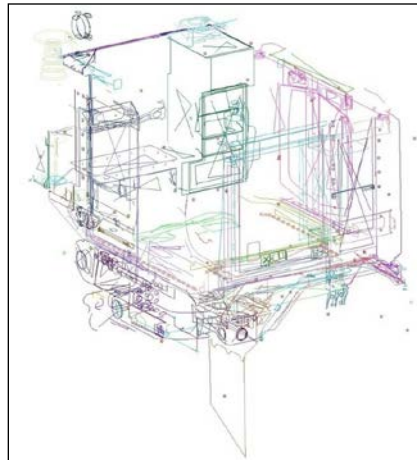
Figure 4. All of the basic geometry captured
in the data collection process for the
SOCOM MATV modeling project.

4. Target Geometry Construction

GMB places much emphasis on developing high-fidelity CAD models to ensure the geometries used in MUVES analyses do not introduce unnecessary error by improperly representing target geometry.

The final product of the data collection process provides the rough geometric data that is necessary for constructing target models. In order to use this data, target modelers first isolate individual components (figure 5) from the rest of the captured data. As captured, the data is generally rough and tainted both by human and machine error—to account for this, and ease the modeling process, the data is conditioned, a process that normalizes (recreate captured curves by hand to remove roughness) and projects the data to planar regions. To ensure this promotes accuracy in the model, the target modeler will use both the measured (captured data) and ideal values for any geometry being conditioned. Conditioned curves are projected into a 3-D environment to produce basic solids and surfaces that, in turn, can be used to build more complicated geometry through Boolean logic and surface tools (figure 6). Completed models are segregated into layers according to criticality trees and engineer/analyst recommendations.
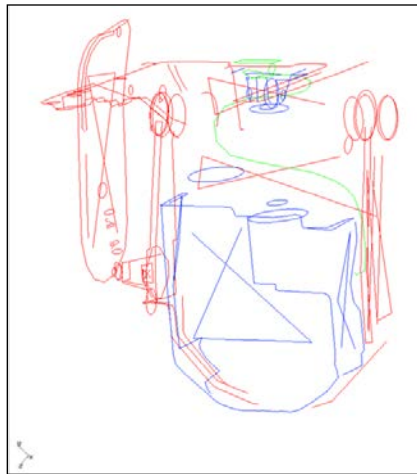
Figure 5. The isolated data for a TOW missile launcher; the missile box at the top is not displayed.
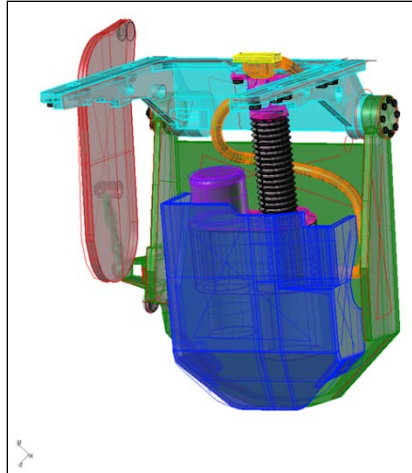
Figure 6. A complete target model for the
isolated data displayed in figure 5.
Each color denotes a different layer
in the model hierarchy.

5.   Conclusion

My experiences over the course of the summer dealt with the various facets of the target modeling process—the theory behind why we create target models, their use, and how we develop a usable product from them. Most of my time was devoted to developing target geometries of the M2A3 Bradley for use in MUVES analyses; this was done by converting and facetizing geometry, collecting data from M2A3 assets with metrology equipment, and developing target models.

Through practical application of skills, I have furthered my proficiency in multiple CAD packages, increased my ability to capture vehicle geometry with metrology equipment, and expanded my ability to create deliverable products at all stages of the target modeling process. In previous years, my focus was primarily to learn new skills and acquire the necessary abilities to develop target geometries without aid from full-time target modelers. This year, I was able to operate independently from the start, hence my focus shifted primarily to the development of quality products. Such high-caliber works will ensure that correctly developed target descriptions and high-quality products lead to accurate analyses of vehicle survivability.

6. References

1. Baker, J. U.S. Army Research Laboratory, Survivability/Lethality Analysis Directorate, Aberdeen Proving Ground, MD. Private Communication, Target Modeling/CAD packages, June 2012.

2. Reynolds, F. U.S. Army Research Laboratory, Survivability/Lethality Analysis Directorate, Aberdeen Proving Ground, MD. Private Communication, Data Collection/Metrology, June 2011.

INTENTIONALLY LEFT BLANK.

Vehicle Technology Directorate (VTD)

INTENTIONALLY LEFT BLANK.

U.S. Army Research Laboratory

SUMMER RESEARCH TECHNICAL REPORT

Wall Climbing Micro Ground Vehicle (MGV) Research

IAN BRYANT
MENTOR: DR. MARK BUNDY
VEHCILE TECHNOLOGY DIRECTORATE
ABERDEEN PROVING GROUNDS, MD

Contents

List of Figures

List of Tables

Abstract

The desire to remove Soldiers from high-risk situations like reconnaissance, and maintenance of buildings and infrastructure has spawned the idea of wall-climbing robots. Such robots use techniques ranging from magnets to gecko pads in order to climb vertical and inverted surfaces. The focus of this project is to run a comparison analysis of different vortex adhesion base plates, which would result in an improvement on the fundamental design of a robotic wall climber. This study includes initial experimentation into the use of inverted wing-inspired base plates to create adhesion forces on the robot. Experimentation on known technology (flat plate with full shroud) has the ability to generate low pressures between the wall and the robot. The use of this base plate in a robot design allowed the vehicle to hold roughly seven times its own weight—about 4.25 lbs. A working platform was used as a control subject to compare the new base plate designs. Through extensive experimentation of the inverted wing base plates, I found that they create downward forces. Preliminary results have indicated that channeling this airflow to the impeller from the inlets will eliminate turbulent airflow that disrupts the vortex.

Acknowledgments

Student Bio

I am entering my junior year at Iowa State University, working towards a degree in aerospace engineering. I entered this degree program with the intention of pursuing a professional career in aerodynamic or propulsion systems. Two years into the program, I still have this ambition, but as I proceed through the rest of my student career, I might find a new interest to pursue. Either way, my ultimate goal is to be part of a team that researches and designs vehicles capable of more effective space flight.

1. Introduction/Background

Great interest has arisen for the development of wall climbing robots over the last decade. Inspiration for this development came from the need to take Soldiers out of potentially dangerous situations. Some robots, such as TALON and Telemax, have already been developed for high risk missions, such as explosive ordinance disposal and fire rescue. Other uses for these robots are cleaning and maintenance, inspection of aircraft and buildings, and surveillance operations. (Sadegh and Xiao, 2007). However, these robots do not have the ability to navigate very steep or vertical surfaces, so they are limited to the areas consisting of relatively flat surfaces and mild inclines.

Several techniques have been used to develop wall climbing robots. The four primary techniques are (1) magnetic attraction, (2) vacuum suction, (3) bio-mimetic techniques, such as gecko pads, and (4) adhesion forces generated by aerodynamic principles, also called vortex adhesion (Sadegh and Xiao, 2007). Each technique has its advantages and disadvantages. For example, magnets are capable of generating large attractive forces, but are limited to ferrous surfaces. Vacuum suction, such as in suction cups, also has the ability to create large adhesion forces, but will only work on flat and smooth surfaces. Gecko pads have the ability to climb almost any surface, granted that the surface is perfectly clean. Vortex adhesion does not require a perfect seal like vacuum suction, and has the ability to travel over more porous surfaces, such as brick and concrete. The issue with this technique, however, is that when larger voids are encountered, the skirting technique is compromised.

This project uses the vortex method along with Bernoulli's Principle as the primary means of adhesion. In this experiment, the robot is designed to be roughly 6×6 sq in. This size is desirable because of the availability of commercial-off-the-shelf (COTS) equipment. A robot of this size should be able to navigate over moderate gaps commonly found on buildings and infrastructure. In an attempt to increase the efficiency of airflow under the robot, different styles of base plates are used. Typically, flat bases with skirting are used in this kind of robot, but these plates do not optimize the airflow. In this experiment, a known flat plate technology is used as the base line or control, while plates with an inverted airfoil shape are tested for improved performance. It is believed that the inverted wing shape will allow for smoother airflow and will create a lower pressure vortex between the wall and the robot. In theory, a lower pressure will generate a larger adhesion force to the wall.

2. Equations and Terms

2.1 Equations

$$\psi = \frac{\Gamma}{2\pi}\ln r \quad \text{(Vortex Streamfunction)} \tag{1}$$

$$v_\theta = -\frac{\Gamma}{2\pi r} \quad \text{(Tangential velocity of a vortex)} \tag{2}$$

$$\frac{v^2}{2} + \frac{P}{\rho} = constant \text{ (Bernoulli's equation)} \tag{3}$$

$$\frac{d\eta_c}{dx} = B_0 + \sum_{n=1}^{\infty} B_n \cos(n\theta) \text{ (Fourier Series Solution)} \tag{4}$$

$$\frac{x}{c} = \frac{1}{2}(1 - \cos\theta) \text{ (Conversion Factor)} \tag{5}$$

$$C_l = 2\pi(\alpha - (B_0 - \frac{B_1}{2})) \text{ (Lift Coefficient)} \tag{6}$$

$$Thrust = (\rho_{air} * v^2 * A)_i - (\rho_{air} * v^2 * A)_o \tag{7}$$

$$Q = v * A \text{ (Volumetric flow)} \tag{8}$$

2.2 Scientific Terms

Pressure: psi (Pa)

Ambient Pressure: psi (Pa)

Voltage: Volts

Normal Force: lb_f (N)

Dragging Force: lb_f (N)

Lift Coefficient: dimensionless

Angle of attack: radians

Thrust: lb_f (N)

Density: slug/in^3 (kg/m^3)

Volumetric Flow: in^3/s (m^3/s)

3. Design Methodology

The central component of this robot is the vortex generated to create a low pressure system between the robot base and the wall or ceiling. A centrifugal impeller is placed over a central inlet hole to pull air from under the robot and generate the vortex. The impeller is designed with 10 backward facing and inclined vanes with a slight taper towards the end of each vane (figure 1).

Figure 1. Impeller.

Typical vortex generating robots have a means of containing the vortex underneath the robot. To do this, a 68-gauge polyester sheet is placed around the edges of the base plates to help contain the vortex. This material is chosen because it will conform to minor contours apparent in some surfaces.

A new design concept involving the use of inverted wing designs to create downward forces on the robot will be tested. This concept is similar to the one used in Formula 1 racing cars to create more downward forces on the car while it is driving. For preliminary experimentation, an inverted airfoil shape similar to that of a NACA 8303 is applied to both rectangular and circular base shapes. Internal vanes similar to a NACA 8504 are also included in the design shown in figures 2 and 3. Figures 4 and 5 show the same plates without internal vanes. The primary wing has a theoretical lift coefficient of 2.23, while the vanes have a theoretical lift coefficient of 2.42. These coefficients are found at 9.27° and 18.6°, respectively. Theoretically, these plates should create downward forces acting on the robot, which could possibly eliminate the necessity of a shroud.
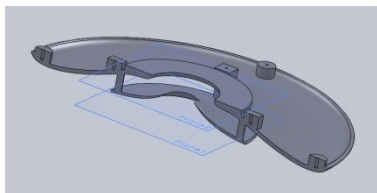

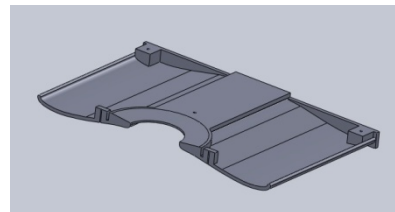
Figure 2. Circular airfoil plate with vanes.　　Figure 3. Rectangular airfoil plate with vanes.
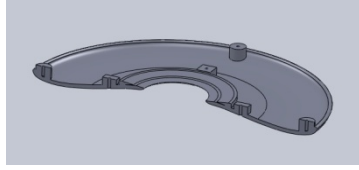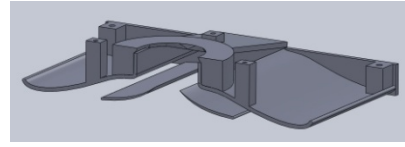
Figure 4. Circular airfoil plate, no vanes.

Figure 5. Rectangular airfoil plate, no vanes.

To create an additional force on the robot, a thrusting cone (figure 6) is incorporated into the preliminary design of the control platform. This concept is used on the City Climber robot from the City College of New York to redirect exhaust air from the impeller back in an axial direction (Sadegh and Xiao, 2007). The redirected air should create a downward force on the robot helping it adhere to the wall. (NOTE—while the cone provided 3 g of force, it was not enough to counteract the 10 g of weight added by our cone.)
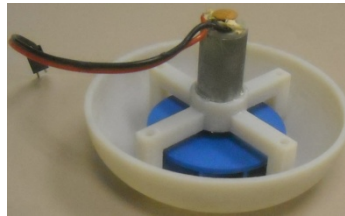

Figure 6. Redirection cone assembly.

For a perching device, a simple "L" shaped hook is mounted to the robot so it may hang onto ledges climbing. Figure 7 shows the perching hook holding the control plate to a ledge while the impeller is off.

The drive system consists of two wheels placed at the center of the plate. This setup allows for easy mobility and quick turning through the use of differential steering. Both perching and drive systems are controlled by a handheld Spektrum transmitter.
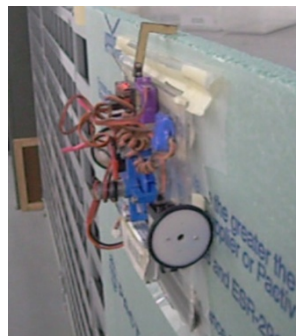

Figure 7. Active perching device.

4. Fabrication

The experimental plates, impeller, and motor mount for the robot were prototyped on an Objet 260v 3D printer using a VeroGray material. Later, both the impeller and the motor mount were printed on a Fortus 400mc 3D printer using ABS plastic. The impeller was later printed out of a more durable ULTEM (polytherimide) plastic. The control plate was cut from a thin acrylic sheet by a Universal VersaLaser cutting machine.

5. Experimentation

To assess the performances of the experimental bases, each plate is placed on top of a testing platform, as seen in figure 8. The platform uses a 5 in-D-4 V Low Pressure Sensor (figure 9) in conjunction with a power source and voltmeter to take pressure readings. When 4 V is supplied to the sensor, it can read up to ± 5 in of H_2O of pressure change. In this experiment, measurements are taken with increasing shroud coverage at ride heights ranging from 0 in to 9/64 in at 1/64-in intervals. To convert voltages into pressure, refer to the conversion equation in appendix C. A Berkley 50 lb/23 kg electronic scale is then used to verify the data obtained from the sensor. This same scale is then used to collect data on the driving force of the robot. The driving force test is conducted on both a horizontal and vertical surface.

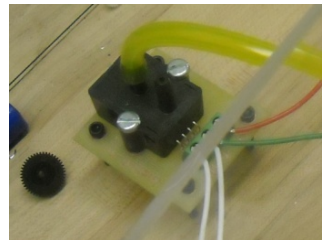Figure 8. Low pressure testing platform.   Figure 9. 5 inch D-4V Low Pressure Sensor.

6. Results and Discussion

Figure 10 is a graph displaying the results of a force capacity test on the baseline platform. Increasing the voltage input to the motor shows an increase in maximum force load with a maximum force of 4.25 lbs. Due to time constraints, the same test could not be performed on the experimental plates; however, force loading tests are scheduled for the near future.
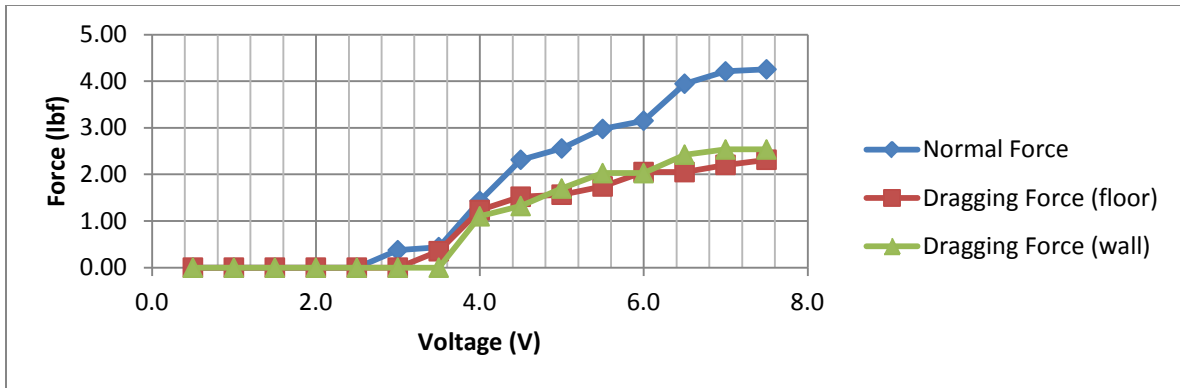
Figure 10. Effect of voltage on the carrying and dragging capacity for the flat plate control subject at full shroud. The weight of the robot is included in the normal force.

Figures 11 and 12 show the control plate during operation on both a brick wall and an inverted surface.
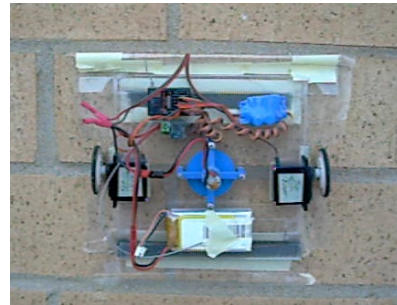

Figure 11. Control plate on an inverted surface.   Figure 12. Control plate on a brick wall.

As shown in figures 13–17, every plate has equivalent pressure differentials at zero ride height, regardless of the amount of shroud coverage present on the robot. This result may be attributed to the fact that a near perfect seal is formed at zero ride height. However, even a slight change in ride height appears to quickly change these results. Looking at the results in figure 14, the rectangular vaned plate appears to show similar trends to those of the control plate, where the other plates do not appear to show similar trends.
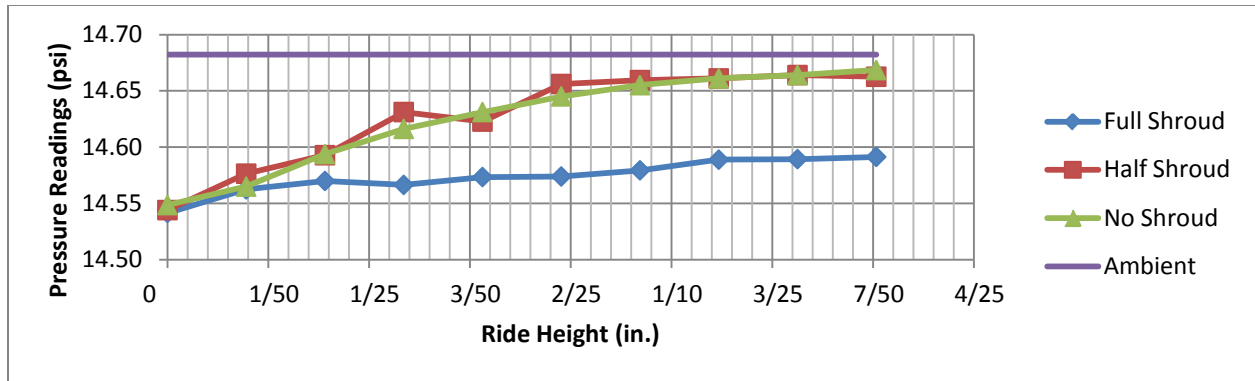
Figure 13. Effects of ride height on pressure for the flat plate control subject of varying shroud coverage.
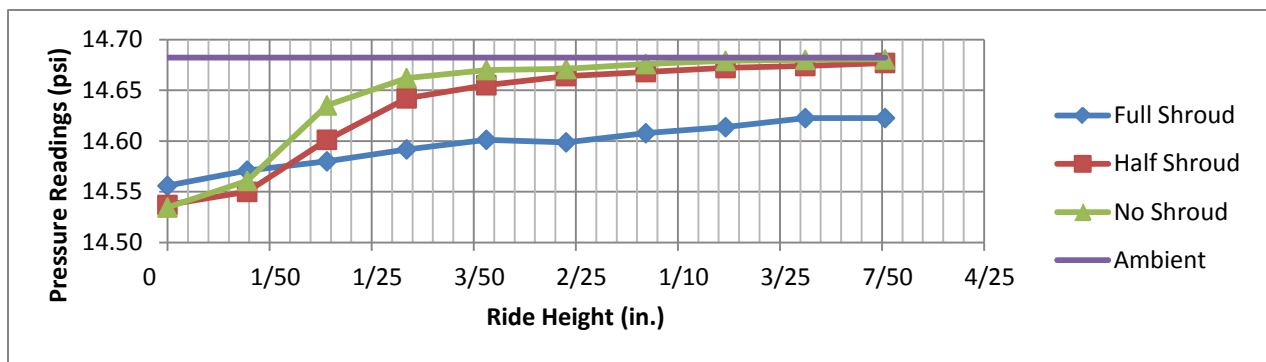

Figure 14. Effects of ride height on pressure for a rectangular and vaned plate of varying shroud coverage.
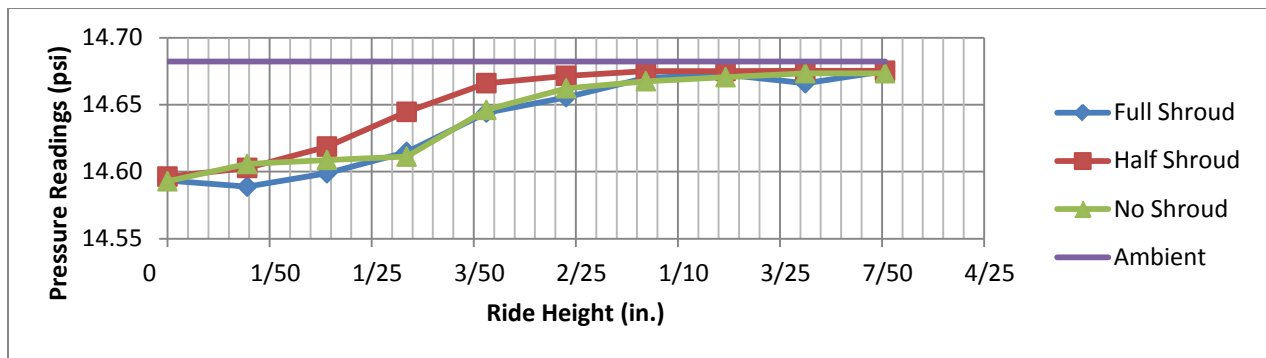

Figure 15. Effects of ride height on pressure for a rectangular and un-vaned plate of varying shroud coverage.
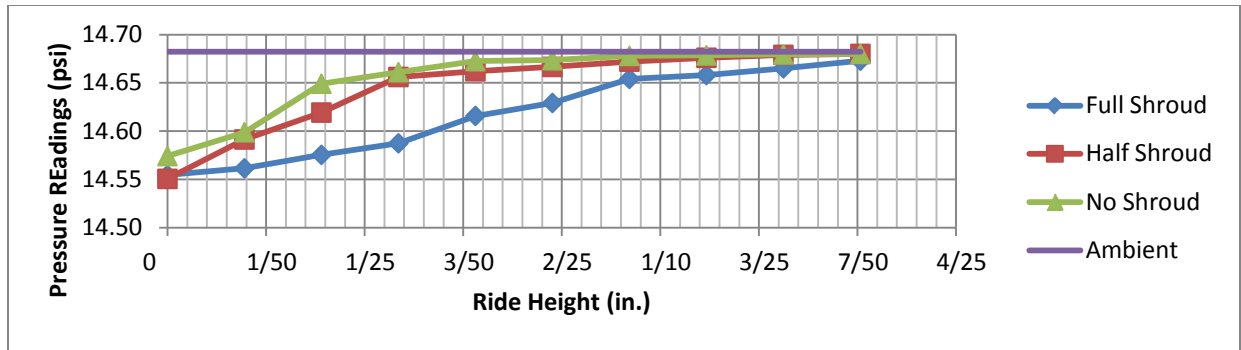
Figure 16. Effects of ride height on pressure for a circular and vaned plate of varying shroud coverage.
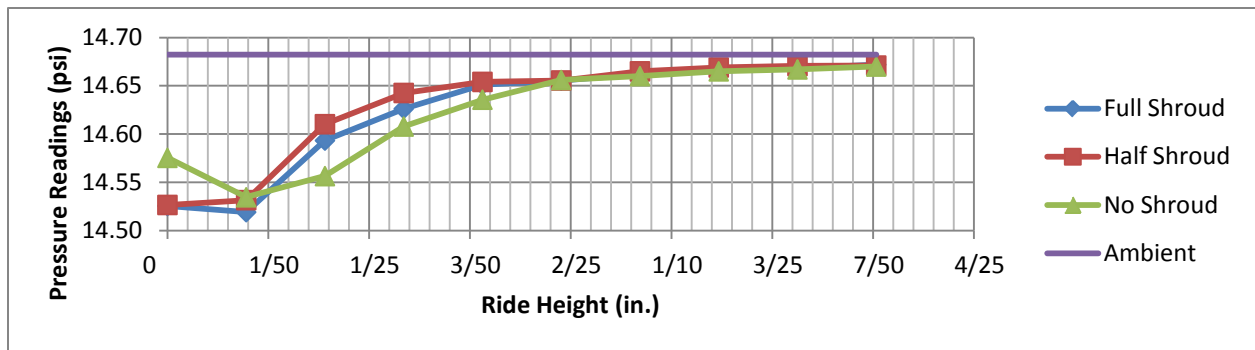

Figure 17. Effects of ride height on pressure for a circular and un-vaned plate of varying shroud coverage.

Pressure field tests are conducted to assess the differences between the rectangular vaned plate and the control plate. The results of this experiment are shown in figures 18 and 19. Comparing the two figures, the rectangular vaned plate is showing a region of relatively high pressure towards the sides of the base, where the control plate has much lower pressures distributed more evenly. The region of high pressure is believed to be an area of turbulent airflow. In an attempt to reduce the turbulent airflow, a rectangular vaned plate with internal channeling to direct the airflow was fabricated. The new plate and results are displayed in figures 20 and 21. According to the results shown in figure 21, the new plate is showing a more even distribution of pressures on the same magnitude as the control plate. Figure 22 shows the channeled plate design operating on an inverted surface.
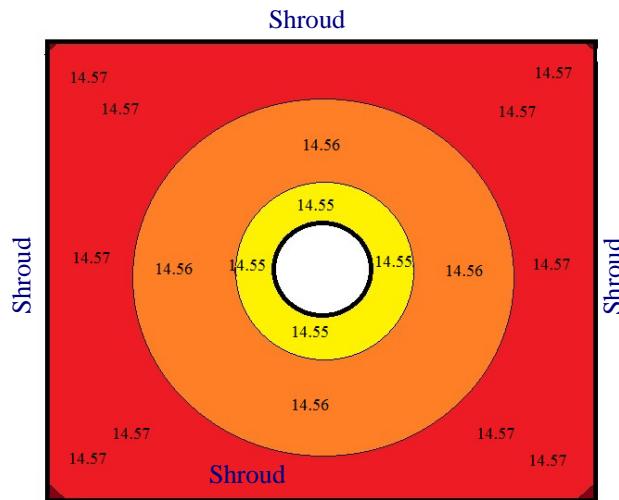
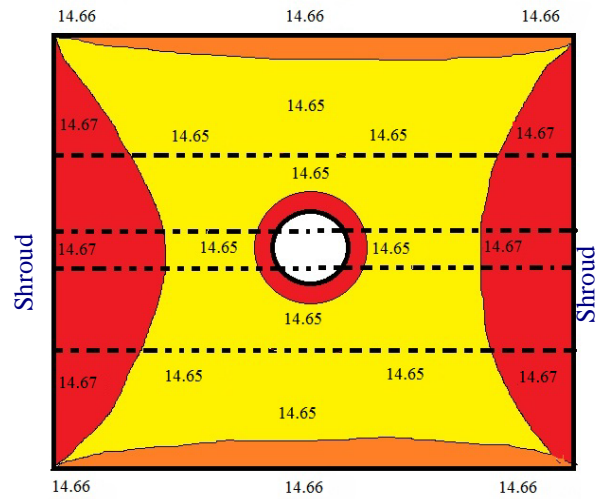Figure 18. Pressure field test of control plate.

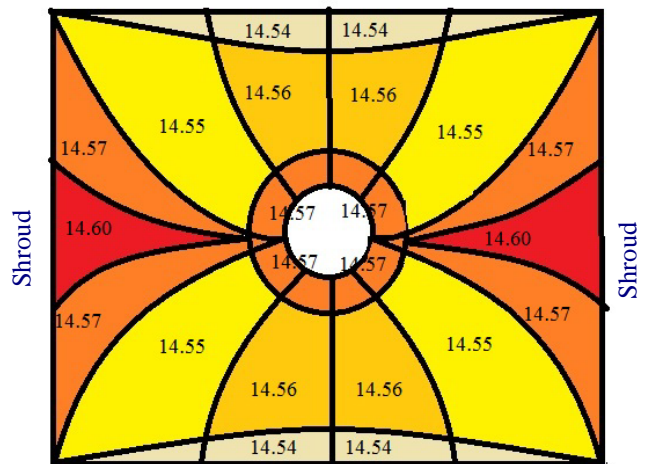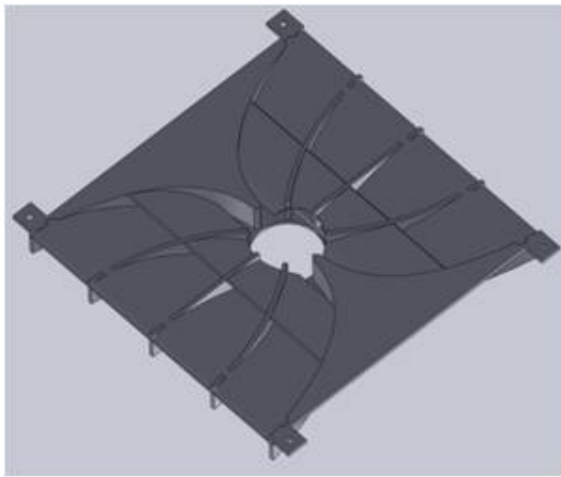Figure 19. Pressure field test of rectangular vaned plate.

Figure 20. Rectangular vaned plate with internal channels.

Figure 21. Pressure field test of channeled plate design.

Figure 22. Channeled plate on an inverted surface.

7. Summary and Conclusion

Observation shows that gap distance between the impeller and base plate is critical to performance. The closer the impeller is to the plate, the better the impeller will perform. The results obtained from the control plate conclude that battery voltage can be lowered and still maintain enough force to adhere the robot to the wall. It may be possible to incorporate an electronic speed controller that can replace the electronic switch in order to vary motor speed, which should vary the vacuum under the robot.

After reviewing the results, it is clear that the rectangular vaned plate with channeling is currently the most effective experimental design to be tested. It shows the closest trends with half-shrouding to those seen in the control plate with complete shroud coverage. Channeling the airflow under the rectangular vaned plate has yielded pressures on the same magnitude as the control plate.

8. Future Work

Due to some constraints, many parts of the robot could not be examined or improved. One part is impeller optimization. Right now, a generic impeller based off of previous designs is used; impeller optimization, however, could increase the performance of the robot. Airfoil optimization is also planned for future experiments. The inverted wing design is a proven application, so finding the most efficient airfoil design would also improve performance of the robot. Channeling the airflow has also been proved to work, so future experiments involving this technique are currently being considered. Right now, the robot is limited to a single surface. To reach a second surface, the robot has to be removed from one surface and placed on the next. Adding a second platform that adds a degree of freedom would allow the robot to transfer between surfaces. The perching and drive mechanisms currently in place are restricted to certain situations at the moment, and will be developed further to allow for a wider range of situations. To increase operation time in the field, plans for the incorporation of solar cells have been made. Lastly, during experimentation, it was noticed that the robots base would bend and sometimes deform during operation. Therefore, detailed structural analysis of the plates will be performed to determine areas that need more support. Since speed can be varied, an electronic pito tube can be implemented to control the electronic speed controller to maintain the appropriate vacuum under the robot.

9. References

1. Alinejad, J.; Hosseinnejad, F. Aerodynamic Optimization In the Rotor of Centrifugal Fan Using Combined Laser Doppler Anemometry and CFD Modeling. *World Appl. Sci. Journ* **2012**, *17*, 10.

2. Clarage Engineering Data. *Fan Performance Characteristics of Centrifugal Fans*, ED-2400, Pulaski, TN, 2000.

3. Damangir, E.; Montazerin, N. *Joint Impeller/Scroll Sizing of Squirrel Cage Fans Using Alternative Non-dimensional Head and Flow Rate Coefficients,* Amirkabir University of Technology, Teheran Iran.

4. Hill, P.; Peterson, C. *The Centrifugal Compressor*; In Mechanics and Thermodynamics of Propulsion*, 2nd ed.; Addison-Wesley, 1992.

5. Kinoue, Y.; Shiomi, N.; Setoguchi, T. *Design and Experimental Studies of Radial-Outflow Type Diagonal Flow Fan*, AICFM_TM_031, IIT Madras, Chennai, India, 2011.

6. Lee, Y.; Ahuja, V.; Hosangadi, A.; Slipper, M. E.; Mulvihill, L. P.; Birkbeck, R.; Coleman, R. M. Impeller Design of a Centrifugal Fan with Blade Optimization. *Inter. Journ. Of Rotat. Mach.* **2011**, 2011.

7. McPherson, M. J. Fans. In *Subsurface Ventilation Engineering.*

8. McPherson, M. J. Introduction to Fluid Mechanics. In *Subsurface Ventilation Engineering.*

9. Munson, Bruce Roy; Young, Donald F.; Okiishi, T. H. *Fundamentals of Fluid Mechanics*. 4th ed. New York: Wiley, 2002, Print.

10. Rababa, K. *The Effect of Blades Number and Shape on the Operating Characteristics of Groundwater Centrifugal Pumps,* Tafila Technical University, Tafila, Jordan.

11. Samarbakhsh, S.; Alinejad, J. *Experimental and numerical analysis of eight different volutes with the same impeller in a squirrel-cage fan,* Amirkabir University of Technology, Teheran Iran.

12. Xiao, J.; Sadegh, A. *City-Climber: A New Generation Wall-Climbing Robots*; The City College, City University of New York USA, 2007.

Appendix A. Vortex Theory

A vortex is a series of concentric circular streamlines with a stream function defined by the following equation:

$$\psi = \psi(r), \tag{9}$$

where ψ is the stream function and r is the radius. This means that the stream function is only dependent on the radius of the vortex. Taking this equation and solving for the Laplace Equation ($\nabla^2\psi = 0$), it is found that the stream function can be defined as:

$$\psi = C_1 \ln r, \tag{10}$$

where C_1 is a constant. With this definition of the stream function, the tangential velocity (v_θ) and radial velocity (v_r) can be found. Since a vortex is made out of multiple circular streamlines, there is no component of radial velocity. The tangential velocity is found in the following way:

$$v_\theta = -\frac{\partial\psi}{\partial r} = -\frac{C_1}{r}. \tag{11}$$

A key component of a vortex is its circulation (Γ) which is always constant along a streamline. Defining circulation around an arbitrary curve, it is found that:

$$\Gamma = \oint_C \vec{v}d\vec{s}. \tag{12}$$

Taking equation 12 and defining the curve as a circle of radius r, the integral becomes:

$$\Gamma = -\int_0^{2\pi} v_\theta r d\theta. \tag{13}$$

By substituting equation 11 into equation 13 and solving for the constant C_1, it is found that the constant equals:

$$C_1 = \frac{\Gamma}{2\pi}. \tag{14}$$

Taking this value for the constant and substituting it back into equations 10 and 11, the streamfunction and tangential velocity of a vortex are found to be:

$$\psi = \frac{\Gamma}{2\pi}\ln r \tag{15}$$

$$v_\theta = -\frac{\Gamma}{2\pi r}. \tag{16}$$

Equation 16 states that tangential velocity is inversely proportional to the radius of the vortex. This means that fluid particles within the vortex move faster if they are closer to the center of the vortex. Applying Bernoulli's Principle (which states that fluids have lower pressures at higher velocities) to the situation, it can be said that the pressure of the fluid within the vortex is lowest towards the center of the vortex. In the case of the robot, the pressure is lower in the region

between the wall and the base plate because of the presence of the vortex. This pressure is lower than the pressure of the surrounding environment and the differential creates a force that acts towards the region of lowest pressure.

Appendix B. Tables

Table B-1. Table of information used to generate figure 10. Units are in psi.

Ride Height	Full Shroud	Half Shroud	No Shroud	Ambient
0	14.54	14.54	14.55	14.68
1/64	14.56	14.58	14.56	14.68
1/32	14.57	14.59	14.59	14.68
3/64	14.57	14.63	14.62	14.68
1/16	14.57	14.62	14.63	14.68
5/64	14.57	14.66	14.65	14.68
3/32	14.58	14.66	14.66	14.68
7/64	14.59	14.66	14.66	14.68
1/8	14.59	14.66	14.66	14.68
9/64	14.59	14.66	14.67	14.68

Table B-2. Table of information used to generate figure 11. Units are in psi.

Ride Height	Full Shroud	Half Shroud	No Shroud	Ambient
0	14.56	14.54	14.53	14.68
1/64	14.57	14.55	14.56	14.68
1/32	14.58	14.60	14.64	14.68
3/64	14.59	14.64	14.66	14.68
1/16	14.60	14.66	14.67	14.68
5/64	14.60	14.66	14.67	14.68
3/32	14.61	14.67	14.68	14.68
7/64	14.61	14.67	14.68	14.68
1/8	14.62	14.67	14.68	14.68
9/64	14.62	14.68	14.68	14.68

Table B-3. Table of information used to generate figure 12. Units are in psi.

Ride Height	Full Shroud	Half Shroud	No Shroud	Ambient
0	14.59	14.60	14.59	14.68
1/64	14.59	14.60	14.61	14.68
1/32	14.60	14.62	14.61	14.68
3/64	14.61	14.64	14.61	14.68
1/16	14.64	14.67	14.65	14.68
5/64	14.66	14.67	14.66	14.68
3/32	14.67	14.67	14.67	14.68
7/64	14.67	14.68	14.67	14.68
1/8	14.67	14.68	14.67	14.68
9/64	14.67	14.68	14.67	14.68

Table B-4. Table of information used to generate figure 13. Units are in psi.

Ride Height	Full Shroud	Half Shroud	No Shroud	Ambient
0	14.55	14.55	14.57	14.68
1/64	14.56	14.59	14.60	14.68
1/32	14.58	14.62	14.65	14.68
3/64	14.59	14.66	14.66	14.68
1/16	14.62	14.66	14.67	14.68
5/64	14.63	14.67	14.67	14.68
3/32	14.65	14.67	14.68	14.68
7/64	14.66	14.68	14.68	14.68
1/8	14.67	14.68	14.68	14.68
9/64	14.67	14.68	14.68	14.68

Table B-5. Table of information used to generate figure 14. Units are in psi.

Ride Height	Full Shroud	Half Shroud	No Shroud	Ambient
0	14.53	14.53	14.58	14.68
1/64	14.52	14.53	14.53	14.68
1/32	14.59	14.61	14.56	14.68
3/64	14.63	14.64	14.61	14.68
1/16	14.65	14.65	14.64	14.68
5/64	14.66	14.66	14.66	14.68
3/32	14.66	14.67	14.66	14.68
7/64	14.67	14.67	14.67	14.68
1/8	14.67	14.67	14.67	14.68
9/64	14.67	14.67	14.67	14.68

Table B-6. Table of information used to generate figure 15. Units are in lbs.

Voltage	Normal Force	Dragging Force (floor)	Dragging Force (wall)
0.5	0.00	0.00	0.00
1.0	0.00	0.00	0.00
1.5	0.00	0.00	0.00
2.0	0.00	0.00	0.00
2.5	0.00	0.00	0.00
3.0	0.37	0.00	0.00
3.5	0.44	0.35	0.00
4.0	1.43	1.23	1.10
4.5	2.31	1.52	1.32
5.0	2.56	1.57	1.70
5.5	2.98	1.74	2.03
6.0	3.15	2.05	2.03
6.5	3.95	2.05	2.43
7.0	4.21	2.20	2.54
7.5	4.25	2.32	2.54

Appendix C – Calculations

C-1. Airfoil Calculations

$$\eta_c = -0.51895x^4 + 1.35715x^3 - 1.42645x^2 + 0.58815x - 0.0007$$

$$\eta_c = 0.00135x^3 - 0.322x^2 + 0.3207x$$

These are equations for the chord line of both the primary airfoil design and internal vane design, respectively. They were obtained by inputting the NACA four-digit number into an airfoil generator and returning a set of points. A polynomial regression was then fit to the data to obtain the equations. Taking the derivative with respect to x yields:

$$\frac{d\eta_c}{dx} = -2.0758x^3 + 4.07145x^2 - 2.8529x + 0.58815$$

$$\frac{d\eta_c}{dx} = 0.00405x^2 - 0.644x + 0.3207 \,.$$

Next, substitute equation 5[3] with a c (chord length) value of 1.58 for the first equation and 0.784 for the second. Afterwards, run the new equations through equation 4 to find the values of B_0, B_1, and B_2. For the primary airfoil, B_0= -0.082938, B_1= 0.221547, and B_2= -0.148892. For the internal vanes, B_0= 0.0691855, B_1=0.251203, and B_2=0.00031117. Using the values and the angle of attack of the airfoils in equation 6 will yield values for the coefficient of lift. The primary airfoil has a C_L of 2.23 at 9.27° and the internal vane has a C_L of 2.42 at 18.6°.

C-2. Voltage to Pressure Conversion

$$Pressure = \frac{Voltage + 145.615}{0.3624}$$

The above equation takes voltage inputs and converts them to pressure (measured in inches of water). The equation was derived by using the factory specifications of the low pressure sensor along with the sea level atmospheric pressure. To convert from inches of water to pounds per square inch (psi), multiply the result by 0.0361.

---

[3] Refer to page 2 for equations.

U.S. Army Research Laboratory
SUMMER RESEARCH TECHNICAL REPORT

Filament Wound Composite Helicopter Driveshaft

TODD C. HENRY
MENTOR: DR. JARET C. RIDDICK
VEHICLE TECHNOLOGY DIRECTORATE
ABERDEEN PROVING GROUND, MARYLAND

Contents

List of Figures

List of Tables

Abstract

Filament wound composites have the potential to be used in a single-piece composite driveshaft, replacing current multiple-piece metallic driveshafts, which would reduce weight and maintenance downtime. The undulated fiber architecture related to the filament winding manufacturing technique produces unique challenges in the form of predicting fiber direction modulus and strength using traditional theories. Observing and developing a better understanding of the micromechanics of fiber micro-buckling in a filament wound composite tube in compression is necessary for using these composites in design. A $[\pm\theta/89/\pm\theta]$ tube laminate was devised for the express purpose of evaluating the compressive strength and elastic modulus of the unidirectional composite in the fiber direction—properties which are believed to be strongly affected by fiber undulations. Three-dimensional digital image correlation was used to measure in plane strains as well as radial displacements. When fiber-micro-buckling was directly observed, it was accompanied by a large concentration of negative axial strain, negative hoop strain, and a negative relative radius displacement. Experimental test results will be used in validation of a two-scale model used for predicting specimen modulus and strength for use in composite driveshaft optimization.

Acknowledgements

Student Bio

I am currently attending The Pennsylvania State University, studying aerospace engineering for my upcoming third year of graduate school. I graduated from The Pennsylvania State University in 2010 and 2012, respectively, with B.S. and M.S. degrees in aerospace engineering. My research experience is in the field of composite fabrication and testing. As an undergraduate, I worked in the Composites Manufacturing Technology Center, designing and fabricating flexible matrix filament wound tubes for crash safety applications. My previous graduate work focused on experimentally determining a multitude of composite material properties for use in the optimization and design of a filament wound driveshaft. Dynamic mechanical tests in bending and shear were used to predict shaft self-heating under misalignment; tension and compression tests were conducted to determine ply strengths and stiffnesses; and finally environmental, fatigue, and non-destructive evaluation was done to determine material in field viability. In the future, I want to work for the U.S. Army Research Lab, Vehicle Technology Directorate, through the SMART Fellowship with all of the intelligent-friendly people there developing innovate technology for the Soldier.

1. Introduction/Background

Composite materials are attractive in lightweight structural design because of their elastic malleability. A class of composites known as flexible matrix composites (FMC) consists of high-strength fibers, such as carbon, and an elastomeric matrix, such as polyurethane. A possible application for this material is a one-piece carbon/polyurethane filament wound composite helicopter driveshaft that can accommodate misalignment (soft in bending) while transmitting power (stiff in torsion). In this application, a single composite shaft can replace the typical multi-segmented shaft, reducing complexity and maintenance requirements (figure 1). Optimization codes for the design of FMC shafts that are lighter than conventional drivelines rely on the existence of validated models that can predict the stiffness and strength of shafts of arbitrary stacking sequence and winding pattern.
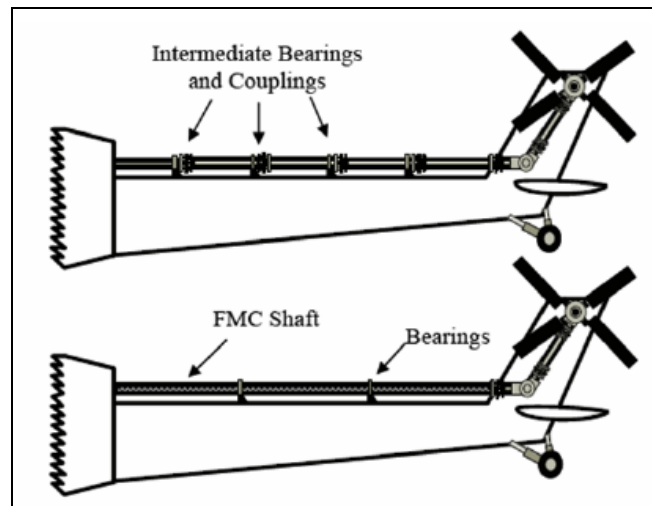

Figure 1. Schematic of traditional driveline (top) and proposed driveline (bottom) (1).

Current methods of predicting the strength and modulus of filament wound tubes based on classical laminated plate theory (CLPT) (2) and measured properties from flat, uni-directionally reinforced fiber have been shown to be highly inaccurate, particularly for tubes made with FMC materials. Models of textile composites address the strength of undulated fibers, as well as the modulus (3), but these models are confined to orthogonally crossing fibers. Approaches for modeling the axial modulus of filament wound FMC tubes have been presented, although they have not been well-vetted with extensive experimental data (4, 5). The key feature of these models is recognition of the modulus-reducing effects of out-of-plane fiber undulations that occur where fibers cross under and over each other in filament winding.

Previous experimental work aimed to back out the in-situ fiber-direction modulus of FMC material in filament wound tubes using an empirical approach (6). Filament wound tubes of varying angle-ply laminate arrangements ranging from ±20° to ±89° were tested to failure. The longitudinal modulus E_1 was backed out with CLPT to match the longitudinal modulus of the experiments E_x (figure 2). The "backed out" fiber-direction compressive modulus of a tube with hypothetical winding angle 0° is around 6.4 Msi (44 GPa) in compression. The predicted value obtained using RoM with known fiber volume fraction and constituent properties is 21 Msi (145 GPa), clearly showing that conventional models cannot be used to model this class of material (6, 7). Measured values of strength were also hypothetically biased to lower values by "barreling" of the tube sample due to high values of Poisson's ratio.
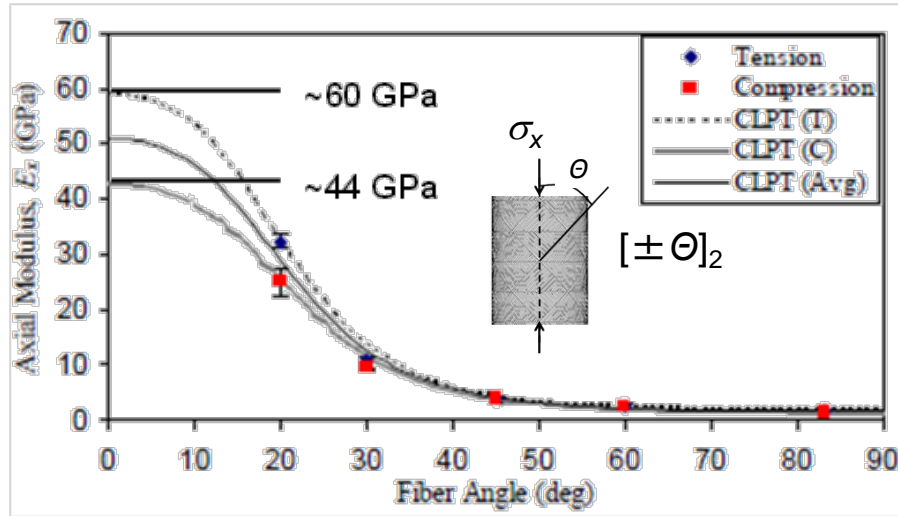

Figure 2. FMC axial modulus versus fiber angle Θ_x —experiments and theory (6).

The filament winding process also creates a weaving architecture known as filament winding pattern (FWP). FWP refers to the integer number of circumferential rhombi (highlighted in red) on the finished part around the circumference (figure 3). FWP can be varied in filament wound tubes without any change to the stacking sequence. Experimental results showed that changing the FWP from 5 to 23 in angle-ply tubes increased the strength by 27 %. Changing the FWP through the thickness—using 10 and 5 in a two-ply laminate—increased the ultimate compression strength by up to 25%, compared to 5 and 5 (8).

Composite cylinders subjected to excessive compressive loading are known to exhibit a rhombic-shaped buckling instability that occurs around the circumference of the sample (9–11). It has been hypothesized that when the FWP is of similar size to the rhombic buckling instability, the sample will have a lower strength (8). The objectives of this investigation are to characterize filament wound tube strain field behavior in compression and to develop a better understanding of the micromechanics of fiber micro-buckling.
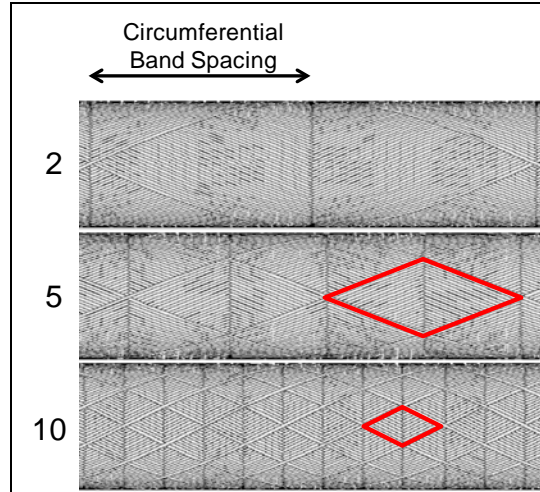
138

Figure 3. Depiction of winding patterns.

2. Experiment/Calculations

The prospective composite materials are all reinforced with about 58% by volume AS4D standard modulus carbon fibers (Hexcel Corp., Stamford, CT). The flexible matrix will be made of DPRN 30917, which is a TDI/PTMEG/PCL prepolymer formulated by Cytec Industries (Olean, NY). The polyurethane prepolymer is cured using a delayed action diamine curative named Duracure C3LF (Chemtura Corp., Middlebury, CT). The high-modulus resin is an epoxide, EPON 862, cured with an aromatic amine curing agent, Curative W (both from Momentive Specialty Chemicals, Columbus, OH). The moduli of DPRN 30917 and EPON 862 are 142 and 428 ksi (976 and 2950 MPa), respectively, in the 1000–2000 $\mu\varepsilon$ strain range.

Standards such as ASTM D 3410 (*12*) for experimentally determining the compressive modulus and strength of a laminated polymer composite are inapplicable here, as a laminated flat plate sample contains neither FWP nor fiber undulation. ASTM D 3410 requires the application of tabs to the ends of the samples because of the large gripping forces for applying compression loading to the sample through shear. An alternative for determining compressive properties of a unidirectional sample is the combined loading compression test, which replaces half of the 0° plies with 90° plies (*13*). The substitution for 90° plies reduces the failure loads, and eliminates both undesirable failures in the grips and the need for sample tabs. The fiber direction modulus and strength can then be "backed out" later using CLPT. In a similar approach, the laminate $[\pm\theta/89/\pm\theta]$ will be tested in this investigation, reducing the Poisson's ratio of the test sample to prevent "barreling" failures.

Samples were machined from a $1.9 \times 0.05 \times 21$ in ($48.3 \times 1.4 \times 533$ mm) (inner diameter, thickness, length) parent specimen to approximately $1.9 \times 0.05 \times 3$ in ($48.3 \times 1.4 \times 76.0$mm)

139

with a water cooled circular diamond saw. Samples were tested with varied FWP through the thickness, as well as orientation angle (table 1). It should be noted that 89° circumferentially wound plies do not have a FWP because they are not woven.

Table 1. Test plan for longitudinal compression of filament wound tubes.

Material System	Stacking Sequence	Winding Pattern				
		[2/2]	[5/5]	[10/10]	[10/5]	[5/10]
Conathane DPRN 30917	[±16/89/±16]	5	5	5	5	5
	[±31/89/±31]	5	5	5	5	5
	[±45/89/±45]	5	5	5	5	5
EPON 862	[±16/89/±16]	5	5	5	5	5
	[±31/89/±31]	5	5	5	5	5
	[±45/89/±45]	5	5	5	5	5
* Tube geometry: 48.3 mm inner diameter, 1.4 mm thickness, 76 mm length						

Samples were tested on a Model 1127 Instron (Norwood, MA) electromechanical universal testing machine, with load voltage acquired and exported by the software Bluehill 2. Samples were tested at a rate of 0.14 in/min (3.5 mm/min). A 50 kip (222 kN) load cell was used to measure applied load. Digital image correlation (DIC) was used in measuring the surface displacement/deformation of the sample under load. DIC is a unique optical approach for tracking pixel displacement by the speckle pattern on the surface of the sample during deformation (*14–16*). The speckle pattern is created using commercially available flat black and white spray paints. If the paint is overly reflective, it will not be possible to correlate the gathered images. Additionally, black and white spray paints provide the largest color/brightness contrast in gray scale. Compared to traditional strain measurement methods, such as strain gages or mechanical extensometers, spray paint application is efficient and does not cause any damage to the surface of the sample. In this investigation, two Point Grey Research (Richmond, B.C. Canada) GRAS-20S4M digital cameras will be used to acquire images simultaneously in a stereo setup, allowing out-of-plane measurements to be made (*17, 18*).

Each sample is potted in end caps to prevent the ends from "brooming" during testing (figure 4). A hemispherical ball-and-socket joint is placed in the load train to compensate for any moment-induced loading to the sample. A florescent lamp is used to provide area illumination to the speckled surface of the sample, with a flexible head lamp used to provide illumination to any dark areas in the area of interest (AOI). Cameras were placed approximately 24 in (61 cm) behind the test sample away from common walkways. Nikon 1.1 in–4.1 in (28 mm–105 mm) focal length lenses were used in focusing the image of the sample.
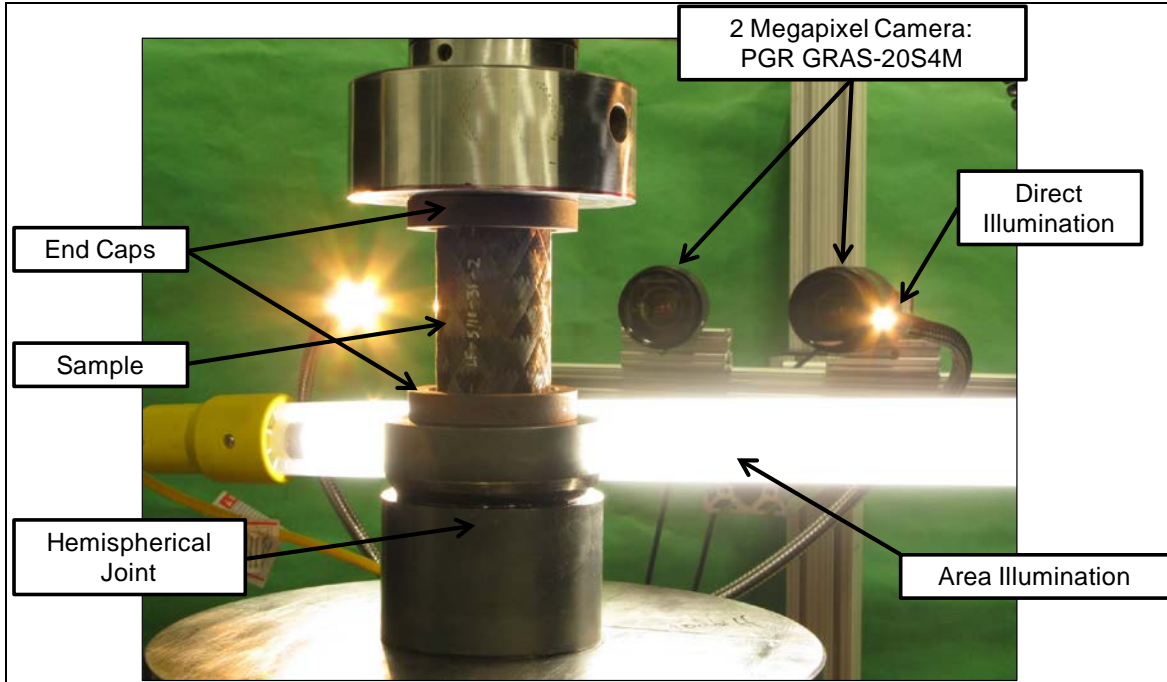
Figure 4. Sample test set-up.

Preliminary results obtained using PGR-GRAS-03K2M cameras suggested that the resolution necessary to observe the effect of the FWP on the strain field, ε_{yy}, is not as great as the resolution needed to observe changes in R or dR. FWP in R and dR was observable but not definitively clear, while FWP was not observable in the strain field. This is most certainly due to the calculated strains being smoothed using a window of minimum size 5 in Vic-3D (*19, 20*). For this investigation, a filter size of 7 and tensor type of Lagrange were used. It is possible that other correlation programs could use a filter as low as one, but it should be noted that neglecting the filter increases noise.

Resolution and noise tradeoffs of the correlated images can be controlled through the use of subset and step size. "The subset size controls the area of the image that is used to track the displacement between images" (*19, 20*). If the subset is too small, Vic-3D may not be able to distinguish each area during correlation due to a coarse speckle pattern or non-ideal lighting. A larger subset, however, decreases resolution, noise, and correlation time. An effort was made to create a fine speckle pattern that allowed for a subset size of 25. "The step size controls the spacing of points that are analyzed during correlation" (*19, 20*). If the subset size is 1, a correlation is performed on every pixel in the AOI. A subset size of 7 was used in this investigation. Increasing the spacial resolution of the testing field is the easiest solution and is possible by using higher resolution cameras, as was ultimately done here. The AOI was nominally 3.8 in (96.5 mm) wide by 2.76 in (70.0 mm) tall. For the GRAS-03K2M (640 x 480 px), the spatial resolution was 168 x 174 px/in (6.6 x 6.9 px/mm), and for the GRAS-20S4M (1624 x 1224 px), the spatial resolution was 426 x 443 px/in (16.8 x 17.5 px/mm).

3. Results and Discussion

Correlated images from just before failure are shown in figures 5 through 8. Individual tow placements and the unit rhombus are easily visible in radius (figure 5). The FWP can easily be seen in the strain fields (figures 5 through 8), with minor exception to figure 6, where failure is initiated by concentrations of negative strain, giving the axial strain field relatively less contrast. The trend of lower amplitude strain around the borders of the rhombus and higher amplitude strain at the center of the rhombus was seen in all samples.
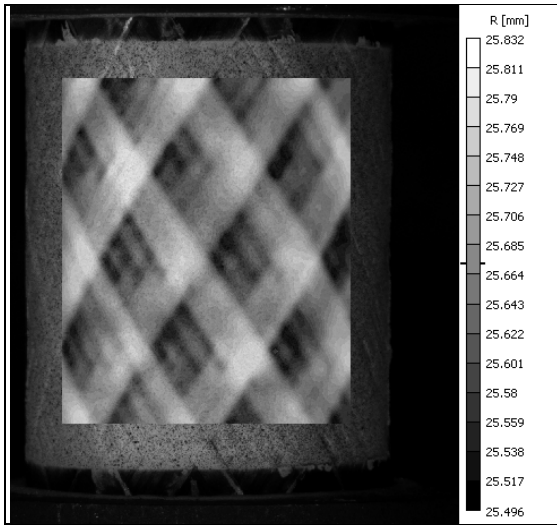
Figure 5. [±31/89/±31] laminate, pattern 10, 30917: radius, R.
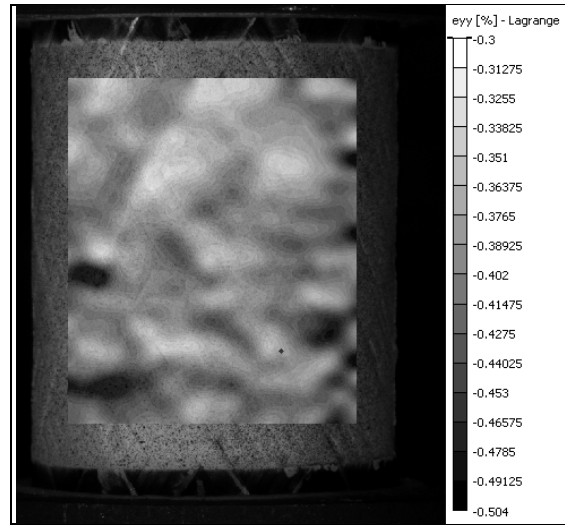
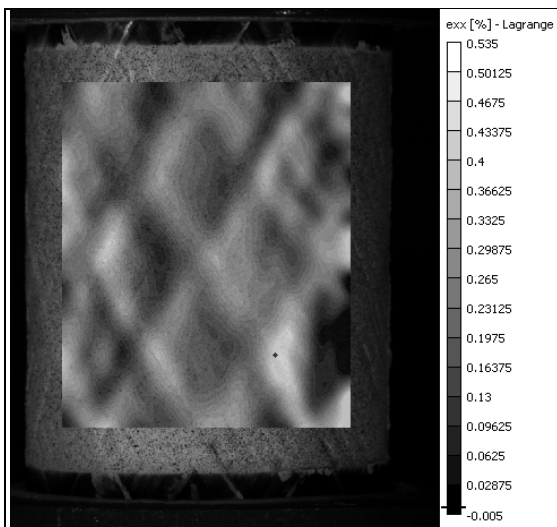Figure 6. [±31/89/±31] laminate, pattern 10, 30917: axial strain, ε_{yy}.

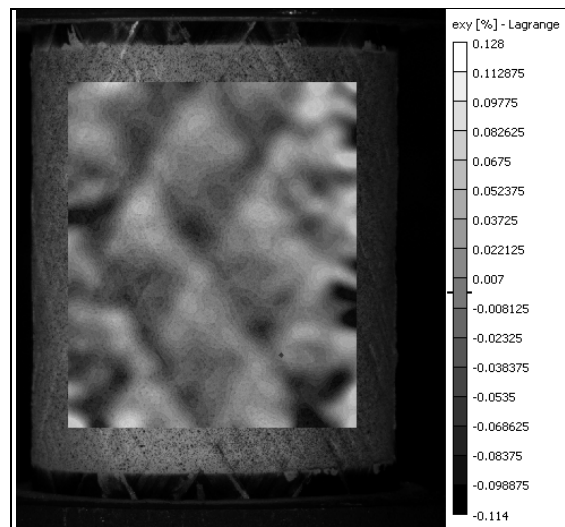Figure 7. [±31/89/±31] laminate, pattern 10, 30917: hoop strain, ε_{xx}.

Figure 8. [±31/89/±31] laminate, pattern 10, 30917: shear strain, ε_{xy}.

In less than 10% of the samples tested, failure initiated in the AOI. That subset of samples all experienced a concentration of negative axial strain near the circumferential undulation band (figure 9). The high amplitude negative axial strain was accompanied by negative hoop strain (figure 10) and a mixture of shear strain (figure 11). Test samples most often exhibited a larger *dR/dt* around the border of the rhombus than at the center of the rhombus. Before failure of the sample occurs, the sample experiences local inward radial movement, likely as a result of excessive local yielding (figure 12).
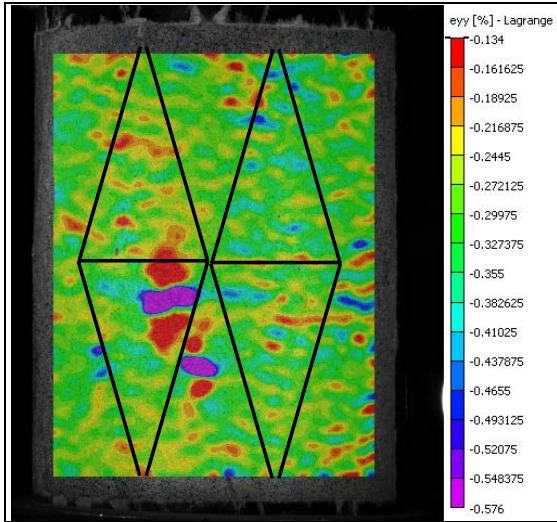

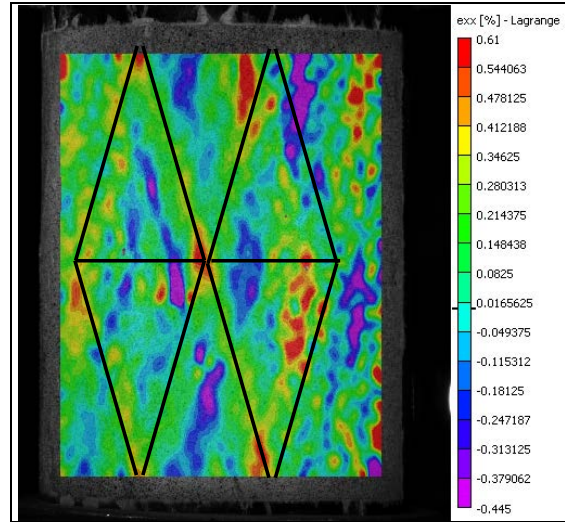Figure 9. [±16/89/±16] laminate, pattern 10, 30917: axial strain, ε_{yy}.

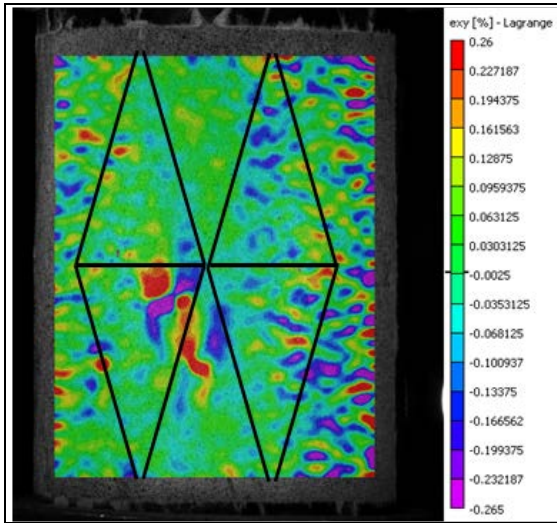Figure 10. [±16/89/±16] laminate, pattern 10, 30917: hoop strain, ε_{xx}.

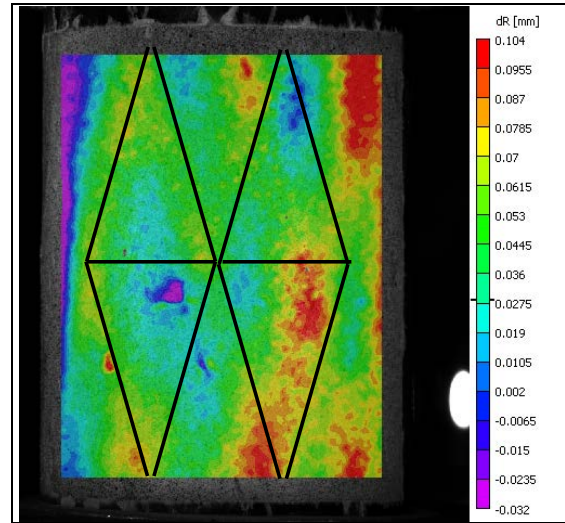Figure 11. [±16/89/±16] laminate, pattern 10, 30917: shear strain, ε_{xy}.

Figure 12. [±16/89/±16] laminate, pattern 10, 30917: change in radius, *dR/dt*.

The negative in-plane stresses and inward radial movement quickly cause a fiber micro-buckling failure (figure 13). Epoxy specimens experienced a similar in mechanism, but more destructive fiber micro-buckling failure.
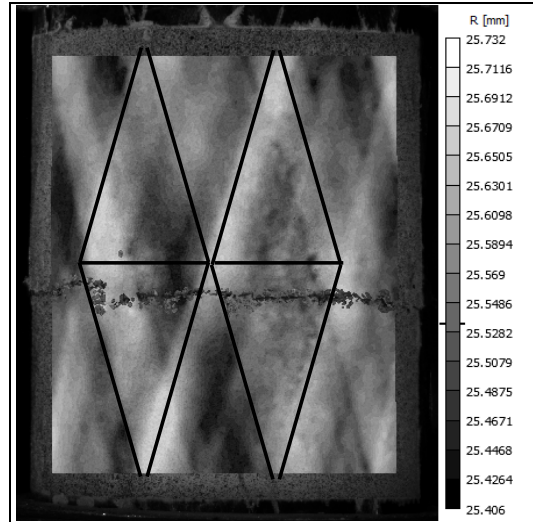

Figure 13. [±16/89/±16] laminate, pattern 10, 30917:
sample micro-buckling failure.

4. Summary and Conclusions

Through extensive experimental testing, we determined that the FWP does have a clear effect on the strain field of the sample. The amplitude of strain along the border of the rhombus, where the fiber architecture is undulated, is lower than the strain at the center of the rhombus, where the material is laminated. This result is somewhat surprising because the circumferential undulation band traveling through the very center of the rhombus is the location where the fiber is most oriented out of plane and should, therefore, be most compliant. The area where the fiber is undulated is also often subject to voids and other defects, which is likely the reason why failure initiates near there.

In experimental cases where fiber micro-buckling initiated directly in the AOI, fiber micro-buckling was accompanied by negative concentrations of axial and hoop strain, as well as a pattern of equal and opposite shear strain. This result is interesting because materials with positive Poisson's ratio should exhibit positive hoop strain with negative axial strain or vice versa. Additionally, *dR/dt* showed that a local negative radial movement occurs immediately before micro-buckling failure. The stress state that causes fiber micro-buckling is likely a combination of axial compression and in-plane shear, which also contributes negative strain in the fiber direction. When attempting to capture composite sample failure, it should also be noted

that materials of softer neat resin modulus exhibit fiber micro-buckling failure more slowly, making observation easier.

5.   References

1.   Mayrides, B.; Wang, K. W.; Smith, E. C. Anaylsis and Synthesis of Highly Flexible Helicopter Drivelines with Flexible Matrix Composite Shafting. *Proc. 61ˢᵗ Forum,* Grapevine, Texas, American Helicopter Society. pg 1–3, June 2005.

2.   Daniel, I.; Ishai, O. *Engineering Mechanics of Composite Materials*, 2ⁿᵈ Edition, New York: Oxford University Press, 2006.

3.   Ishikawa, T.; Chou, T. Stiffness and Strength Behavior of Woven Fabric Composites. *Journal of Materials Science* **1982**, *12*, 3211–3220.

4.   Jensen, D.; Pai, S. Influence of Local Fiber Undulation on the Global Buckling of Filament-Wound Cylinders. *Journal of Reinforced Plastics and Composites* **1993**, *12*, 865–875.

5.   Zindel, D.; Bakis, C. E. Nonlinear Micromechanical Model of Filament-Wound Composites Considering Fiber Undulation. *Mechanics of Composite Materials* **2011**, *47*, 73–94.

6.   Sollenberger, S. Characterization and Modeling of a Flexible Matrix Composite Material for Advanced Rotorcraft Drivelines. MS Thesis, Department of Engineering Science and Mechanics, The Pennsylvania State University, University Park, PA, 2010.

7.   Shan, Y. Flexible Matrix Composites: Dynamic Characterization, Modeling, and Potential for Driveshaft Applications. Ph.D. Thesis, Department of Engineering Science and Mechanics, Penn State. University Park, PA, 2006.

8.   Claus, S. J. Manufacture-Structure-Performance Relationships for Filament-Wound Composite Shells. PhD Dissertation, Department of Engineering Science and Mechanics, The Pennsylvania State University, University Park, PA, 1994.

9.   Card, M. F. *Experiments to Determine the Strength of Filament-Wound Cylinders Loaded in Axial Compression*; NASA Technical Note; Langley Station, Hampton, Virginia, August 1966

10. Hillburger, M. W.; Starnes J. H. Jr. Effects of Imperfections on the Buckling Response of Compression-Loaded Composite Shells. *International Journal of Non-Linear Mechanics* **2002**, *37*, 623–643.

11. Riddick, J. C. Prebuckling, Buckling, and Postbuckling Response of Segmented Circular Composite Cylinders. PhD Dissertation, Department of Engineering Mechanics, Virginia Polytechnic Institute and State University, Blacksburg, VA, 2001.

12. ASTM Standard D3410, "Standard Test Method for Compressive Properties of Polymer Matrix Composite Materials with Unsupported Gage Section by Shear Loading," ASTM International, West Conshohocken, PA, 2003, DOI: 10.1520/D3410_D3410M-03R08, 2003.

13. Adams, D. F.; Welsh, J. S. The Wyoming Combined Loading Compression (CLC) Test Method. *Journal of Composites Technology and Research* **1997**, *19* (3), 123–133.

14. Chu, T. C.; Ranson, W. F.; Sutton, M. A.; Peters, W. H. Applications of Digital-Image-Correlation Techniques to Experimental Mechanics. *Experimental Mechanics* **September 1995**.

15. Sutton, M. A.; Wolters, W. J.; Peters, W. H.; Ranson, W. F.; McNeill, S. R. Determination of Displacements Using an Improved Digital Image Correlation Method. *Computer Vision* **August 1983**.

16. Bruck, H. A.; McNeill, S. R.; Russell, S. S.; Sutton, M. A. Use of Digital Image Correlation for Determination of Displacements and Strains. *Non-Destructive Evaluation for Aerospace Requirements* **1989**.

17. Sutton, M. A.; McNeill, S. R.; Helm, J. D.; Schreier, H. Full-field Non-Contacting Measurement of Surface Deformation on Planar or Curved Surfaces Using Advanced Vision Systems. *Proc. International Conf. Adv. Tech. in Exp. Mechanics*, July 1999.

18. Sutton, M. A.; McNeill, S. R.; Helm, J. D.; Chao, Y. J. Advances in Two-Dimensional and Three-Dimensional Computer Vision. *Photomechanics* **2000**, *77*.

19. Correlated Solutions, "Vic-3D 2010 Reference Manual" www.CorrelatedSolutions.com, 2010.

20. Correlated Solutions. "Vic-3D 2007 Testing Guide" www.CorrelatedSolutions.com, 2007.

INTENTIONALLY LEFT BLANK.

Weapons & Materials Research Directorate (WMRD)

INTENTIONALLY LEFT BLANK.

U.S. Army Research Laboratory
SUMMER RESEARCH TECHNICAL REPORT

Quantum Tunneling Effect in Shape-Controlled Gold Nanoparticles

HAILEY CRAMER
MENTOR: DR. LILY GIRI
WEAPONS AND MATERIALS RESEARCH DIRECTORATE
ABERDEEN PROVING GROUND, MD

Contents

List of Figures

List of Tables

153

Abstract

At the nanoscale, the optical, electrical, and catalytic properties of a material depend on its size and shape. Therefore, synthesis of nanoparticles with controlled size and shape is important when applying them to biosensors, photovoltaics, and other optoelectronic devices. Whereas the effect of "size" on the properties of nanoparticles has been extensively studied in the past two decades, similar studies on the "shape" of nanoparticles have received little attention. The specific goals of this research are to synthesize nanoparticles with desired "shape" and investigate their structure-property relationships focusing on the quantum tunneling phenomenon. Recently, we successfully synthesized colloidal gold (Au), silver (Ag), and mixed Au-Ag nanoparticles using aqueous chemistry. The particles exhibited a mixture of shapes including spheres, rods, and prisms. In this work, we synthesize Au nanorods, nanospheres, and nanotriangles using a wet chemical seed-mediated growth method employing the surfactant cetyltrimethylammonium bromide (CTAB) as a growth-directing micellar template. Precise tuning of thermodynamic and kinetic parameters, and the addition of small concentrations of halide ions, enable us to obtain high yields of these shapes. Characterization of the particles is performed using tunneling electron microscopy, atomic force microscopy, ultraviolet-visible spectroscopy, and x-ray diffraction. Electron tunneling effects are investigated via scanning tunneling microscopy.

Acknowledgments

Student Bio

Hailey Cramer is a rising sophomore at the University of Delaware, where she is studying chemical engineering as a part of the Honors program. She has worked at the ARL Weapons and Materials Research Directorate as a summer student intern for the past four years, where her research focused on the synthesis, characterization, and solar-cell applications of metal and semiconductor nanoparticles. Her previous research resulted in three ARL technical reports and two presentations at the U.S. Military Academy-Army Research Laboratory Technical Symposium. She plans to minor in nanoscale materials and continue research in the future.

1. Introduction/Background

Due to their very small size, nanoparticles obey the laws of quantum mechanics and, therefore, have the ability to participate in quantum tunneling. A recent paper published in "Nature," by Mebrahtu et al. (*1*) has examined this effect by showing that an electron can successfully hop on a carbon nanotube as it travels between two electrical leads. In a similar fashion, our research aims to fundamentally understand and describe the quantum tunneling effect in shape-controlled metal nanoparticles, specifically gold (Au) nanorods, nanoprisms, and nanospheres. Whereas the effect of "size" on the properties of isotropic nanoparticles has been extensively studied in the past two decades, similar studies on the "shape" of nanoparticles have received little or no attention. It is important to note that it is not only the composition and size of nanoparticles that affect their unique optical, chemical, and electrical properties, but also the shape. An increased understanding of the structure-property relationships of shape-controlled nanomaterials will allow for their future integration into advanced materials such as optoelectronics, photonics, biosensors, and drug carriers.

Recently, multiple methods for growth of nanorods (*2–12*), triangular prisms (*5, 13–17*), nanospheres (*18, 19*), and other platonic (*20–22*), branched (*12*), and anisotropic (*12, 23, 24*) morphologies have been explored. Although synthesis can be achieved through photo and electro-chemical methods, colloidal wet-chemistry synthesis has proved to be the most advantageous, as little equipment is necessary and procedures can be scaled up to produce larger quantities of shape-controlled nanoparticles. The majority of literature (*24, 25*) relies on a two-step "seed-mediated" growth method. In the first step, small spherical seed particles, often less than 5 nm in diameter, are created under conditions that allow for rapid growth of all crystal facets. This step involves the use of a metal salt, capping agent, and a strong reducing agent. In the second step, a growth solution containing more metal salt in the presence of a shape-directing molecule or surfactant is used, in addition to a weak reducing agent. The seeds are added to this solution to serve as nucleation sites and to facilitate the reduction of metal ions onto their surface in a seed overgrowth fashion. In opposition to the one-pot homogeneous nucleation we have previously done in our laboratory for synthesis of various nanoparticle shapes (*26*), this heterogeneous seed-mediated growth lowers the activation energy needed for metal reduction and allows for more fine-tuned control over growth conditions using weaker reducing agents and temperatures. This control is favorable, as aqueous shape-controlled crystal growth requires precise tuning of the thermodynamic and kinetic parameters of the reaction including reaction rate, capping agent, reactant concentration, temperature, and pH. The difficulty in controlling these uniquely linked parameters has made it difficult to fully understand the mechanisms behind shape-controlled colloidal synthesis. Thus, focus in literature (*27, 28*) has been placed more recently on developing an explanation for the shape-controlled growth mechanism and less on investigating the unique properties of these materials.

Murphy et al. (*12*) found through a seed-mediated growth method that various shapes, such as rods, wires, cubes, and prisms, can be grown through careful control over the growth step. Gold seeds of about 3–5 nm in diameter were grown through a quick nucleation step, using sodium citrate as a capping agent. They were added to a solution containing gold salt, the surfactant cetyltrimethylammonium bromide (CTAB), and ascorbic acid. In this case, ascorbic acid can only reduce the Au in the presence of the seeds. For the case of nanorods (*7*), it was found that through controlling the ratios of reactants, several different aspect ratios ranging from 4.6 to 18 could be obtained, although multiple centrifugation steps were necessary to separate them from spherical particles. Murphy's group (*3, 4*) also found that employing a surfactant with a longer tail length yielded longer nanorods, and that gold seeds with different sizes and charged surface functionalities resulted in rods with different aspect ratios. In addition, through changing the pH of the growth solution from 2.8 to 3.5, nanorods with a drastically improved yield were produced with minimal centrifugation (*2*).

In a similar chemical process to Murphy's group, Ha et al. (*5*) found that with the addition of trace amounts of halide ions into a growth solution initially designed for the growth of nanorods, Au nanoprisms could be synthesized. Through control over pH and temperature, the size and yield of the nanoprisms were manipulated. There are issues, however, with the degree at which these shaped nanoparticles can be reproduced. Ha's work, in particular, contrasts with Sastry's group (*16*), who reported that iodide ions suppress the formation of nanoprisms. Millstone et al. (*27*) suggests that these conflicting results can be due to the fact that depending on supplier, CTAB may contain iodide contaminates that cause the production of different shapes. This research shows that identical seed particles and growth solutions could be used to form rods, triangular prisms, and spheres simply by controlling the iodide ion concentration and using purified CTAB.

In contrast to the aforementioned research methods, Nikoobakht and El-Sayed (*10*) synthesized Au seeds using CTAB instead of sodium citrate as the capping agent. These CTAB-capped seeds were used in the presence of $AgNO_3$ and produced nanorods in 99% yield, making it the most popular chemical synthesis method for Au nanorods. Through changing the amount of $AgNO_3$ added to the growth solution, nanorods with aspect ratios ranging from 1.5 to 5 were synthesized. Murphy's group (*6*) followed up this research by using their citrate-capped seeds and adding $AgNO_3$ to the growth solution. They found that instead of nanorods, as expected, spheroidal-shaped nanoparticles were produced. Liu and Guyot-Sionnest (*9*) showed through high-resolution TEM that in opposition to the CTAB-capped seeds, which were single crystals with 1.5 nm diameters, citrate-capped seeds have a multiply-twinned structure—thus, explaining the importance of the seed in shape-controlled nanoparticle synthesis. Interestingly, the composition of the seed particle does not have to be the same as the metal chosen for overgrowth (*24*). Seed particles made of a metal with a weaker reduction potential metal have been used to grow hollow shell nanostructures. In addition, shape-specific nanoparticles of one metal have been used as

seeds to allow for overgrowth of another metal, producing various bimetallic anisotropic and polyhedral shapes.

In contrast to the typical CTAB method used by in the literature, Kim et al. (*20*) used a polyol reaction method involving the use of poly(vinylpyrrolidone) (PVP) as a reducing agent to produce various platonic Au nanoparticles. Interestingly, in a very different method, Xie et al. (*14*) synthesized Au nanospheres and triangular nanoplates using bovine serum albumin as the reductant, and found that $AgNO_3$ could be used to control the size of the particles. Shankar et al. (*15*) synthesized gold nanoplates using lemongrass leaf extract as a reducing agent, as well as a shape-directing molecule.

The objective of this research is to synthesize shape-controlled Au nanoparticles and investigate quantum tunneling effects. To date, in this work, we have successfully synthesized Au nanoparticles of cylindrical (nanorods), prismatic (nanoprisms), and spherical (nanospheres) shapes using seed-mediated aqueous methods. Our approach combined previously used approaches (*5, 19*) and differed in using the same seed for all shapes, identifying and using the effect of relative concentration of the starting materials on the yield of the nanoparticles. Transmission electron microscopy (TEM), energy dispersive spectroscopy (EDS), UV-Vis spectroscopy, and dynamic light scattering (DLS) measurements were performed to characterize, respectively, the shape, structure, chemical composition, absorption spectrum, and surface charge of the synthesized nanoparticles. The quantum tunneling effect studies on synthesized shape-controlled nanoparticles are underway and will be reported in our future communications.

2. Experiment/Calculations

2.1 Materials

Hydrogen tetrachloraurate (III) trihydrate ($HAuCl_4 \cdot 3H_2O$), hexadecyltrimethylammonium bromide (CTAB), trisodium citrate dihydrate, sodium borohydride ($NaBH_4$), L-ascorbic acid, and potassium iodide (KI) were purchased from Sigma Aldrich. All chemicals were used as received. Distilled deionized water was used for all solution preparations. All glassware was cleaned in this order: tap water and dish detergent, purified water, ethanol, and nitrogen gas to dry. The growth stock solution was used within 6 h of preparation. If surfactant fell out of the growth solution, it was heated at 50 ºC to re-dissolve the precipitate and then cooled to room temperature. Stock solutions of $NaBH_4$ and L-ascorbic acid were freshly prepared before every synthesis. All other solutions were stable for up to several months.

2.2 Preparation of Gold Seeds

A gold seed solution was prepared by mixing 10 mL of a 5.0 x 10^{-4} M $HAuCl_4$ stock solution with 10 mL of a 5.0 x 10^{-4} M trisodium citrate dihydrate stock solution in a 40 mL vial. To the

vial, 600 µL of ice-cold 0.1 M $NaBH_4$ was added while being vigorously stirred. Upon addition of $NaBH_4$, the solution becomes light pink in color. Stirring continued for 2 min, at which point the solution became red in color. The solution was then aged at room temperature for 3 h and used directly after this. The aging period is necessary to allow the remaining sodium borohydride to react with water, but periods of time longer than 10 h cause the particles to aggregate, which is undesirable for their use in further shape-controlled growth. Through transmission electron microscopy (TEM), the particles averaged to be about 4 nm in diameter. The solution was fairly monodisperse with very few particles of shapes other than spheres. A diagram illustrating this procedure is shown in figure 1.
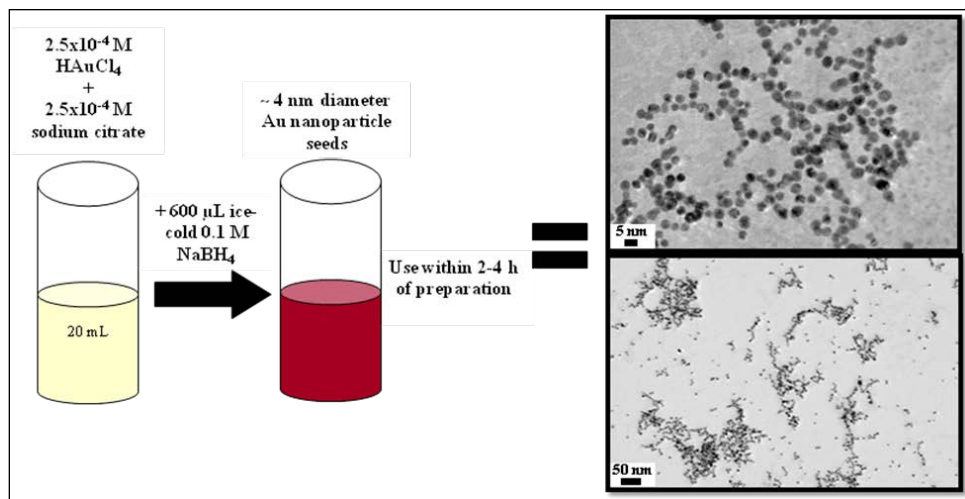

Figure 1. Schematic for gold seed preparation. Average size was confirmed to be about 4 nm through TEM.

2.3   Growth of Gold Nanoparticles

A 200 mL stock growth solution containing $2.5\text{x}10^{-4}$ M $HAuCl_4$ and 0.1 M CTAB was prepared in a beaker. This solution was then heated at 50 ℃, with occasional stirring to dissolve the CTAB. After about 10 min, the solution turned a clear orange color at which point it was removed from the hot plate and allowed to cool to room temperature. The color change indicates the formation of the complex ion $CTA^+AuCl_4^-$. This growth stock solution and the gold seeds were then used to synthesize Au nanorods, nanospheres, and triangular nanoprisms through manipulating reaction parameters, as shown in figure 2.
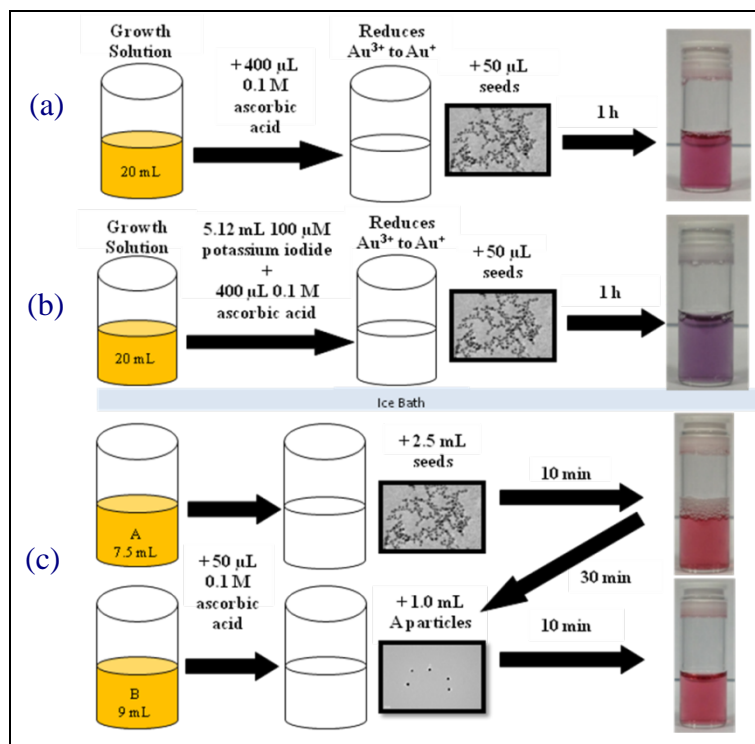
Figure 2. Schematic for Au nanoparticle growth. (a) Nanorod, (b) Nanoprism, and (c) Nanosphere (first two seeding steps are shown. Subsequential seeding can be continued for growth of larger particles).

The synthesis of Au nanorods was achieved by pouring 20 mL of the stock growth solution into a 40 mL vial and mixing in 400 µL of a freshly prepared 0.1 M ascorbic acid solution through inverting the vial three times. The addition of ascorbic acid causes the solution to change from yellow to clear in color, indicating the reduction of the Au^{3+} ions in solution to Au^+. Ascorbic acid is too weak to fully reduce the Au salt without the addition of Au seeds, so 50 µL of the seed solution was added to the vial and the tube was inverted 10 times to mix. The entire reaction was performed at 25–30 ℃. No further mixing was done for the next 5–10 min as the solution became magenta in color, indicating particle growth. After an hour, the solution was red-purple in color.

For the growth of nanoprisms, a similar procedure for the growth of Au nanorods was used; however, KI was mixed with the initial growth solution and the reaction occurred at a lower temperature. In a 40 mL vial, 5.12 mL of a 100 µM solution of KI was mixed with 20 mL of the stock growth solution. The vial was then placed in a water bath maintained at 15 ℃ during the rest of the reaction, as a lower temperature has been found to increase the yield of nanoprisms (5). To the vial, 400 µL of a freshly-prepared 0.1 M ascorbic acid solution was added and the vial was inverted 3 times to mix. To begin nucleation, 50 µL of the seed solution was then added and the vial was inverted 10 times to mix. No further mixing was done for the next 10–20 min as the solution became purple in color, indicating particle growth. It was noted that the addition of KI slowed the reaction rate, and color change occurred after a longer period of time than

observed for nanorod growth. After 2 h, the solution was purple in color. Some of the surfactant precipitated out of solution, so the solution was heated at 50 ℃ to re-dissolve.

A multi-step seeding growth procedure was used to produce increasingly larger nanospheres. Three flasks were labeled A, B, and C, respectively. In flask A, 7.5 mL of growth solution was added, while 9 mL of growth solution was added to B and C. The entire reaction was performed at 25–30 ℃. In each flask, 50 μL of 0.1 M ascorbic acid solution was added while vigorously being stirred with a stir bar. In flask A, 2.5 mL of the seed solution was quickly added and vigorously stirred. Stirring continued for the next 10 min as the solution turned to a deep red color, indicating particle formation. After 30 min, 1.0 mL of the solution A was quickly added to vial B and vigorously stirred for 10 min. Sequentially, after allowing 30 min for particles B to form, 1.0 mL of solution B was quickly added to flask C while being stirred vigorously. Stirring was again continued for 10 min. It was noted that the solutions became increasingly purple in color from A to C.

2.4   Purification

Directly after synthesis, all solutions were placed into 10 mL centrifuge tubes for purification. For nanorods and nanoprisms, centrifugation was performed at 1000 rpm for 10 min. For nanospheres, centrifugation was done at 5600 rpm for 30 min. The light pink supernatant, containing smaller spherical particles and other shaped impurities, was removed from each tube with a pipette and the pellet was redispersed in 10 mL deionized. The solutions were then re-centrifuged at the previously stated speeds and times. This was repeated until bubbles were no longer visible in the tubes after shaking, indicating that the majority of the surfactant was removed. After the last centrifugation step, the pellet for each sample was redispersed in 100 μL distilled deionized water.

3.   Results and Discussion

The particles were characterized through UV-Vis spectroscopy, TEM, EDS, and DLS. For TEM and EDS analysis, the purified solutions were sonicated for 15 min and deposited onto copper grids. Purified solutions were used as-made for UV-Vis spectroscopy and DLS.

Figures 3, 4, and 5 show the TEM images of the shape-controlled nanoparticle solutions, and confirm that nanospheres, nanorods, and nanoprisms were successfully synthesized. The spherical seed particle solution shown in figure 3 was very monodisperse with average particle diameters of about 4 nm and very few impurities of undesired shapes. The nanospheres, shown in figure 4, increased in size through the multiple-seeding growth method, respectively, with the particles in 4a averaging about 5 nm in diameter, and the particles in 4b about 8 nm in diameter. Particles for solution C have yet to be imaged through TEM. These nanosphere solutions were also fairly monodisperse with few impurities of undesired shapes. For nanoprisms, shown in

figure 5b, a majority of particles had an edge length of about 150 nm, although a variety of smaller and larger nanoprisms was seen. It is interesting to note that in the lower image, the crystal lattices of two nanoprisms are overlapping, indicating that these particles have a thickness of only a few nanometers. Lastly, the Au nanorod sample, shown in figure 5a as well, contained very monodisperse nanorods of about 200 nm length and 20 nm width, giving an aspect ratio of 10. However, the yield for these nanorods was low, and large quantities of spherical shaped impurities were seen. These impurities could have been further centrifuged out from the nanorods, although this would not improve the number of rods seen through TEM.
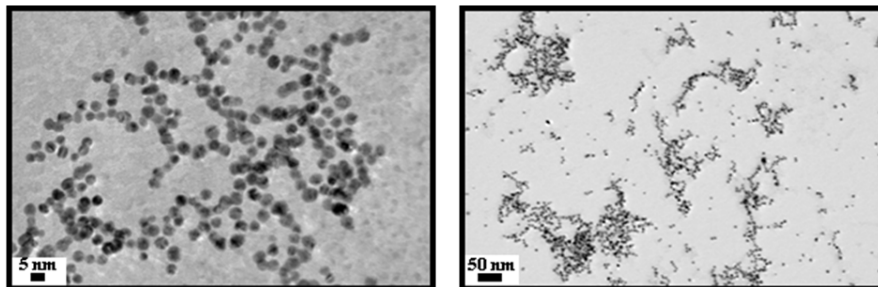
Figure 3. Au seeds (about 4 nm in diameter). Scale bars are 5 nm (top) and 50 nm (bottom).
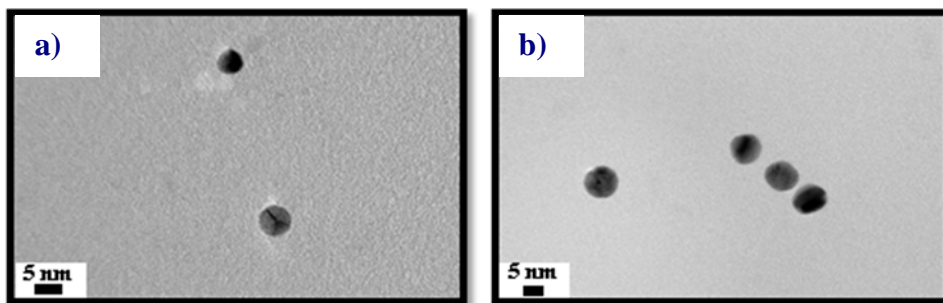

Figure 4. Au nanospheres (a) solution A (about 5 nm in diameter) and (b) solution B (about 8 nm in diameter). Scale bars are 5 nm.
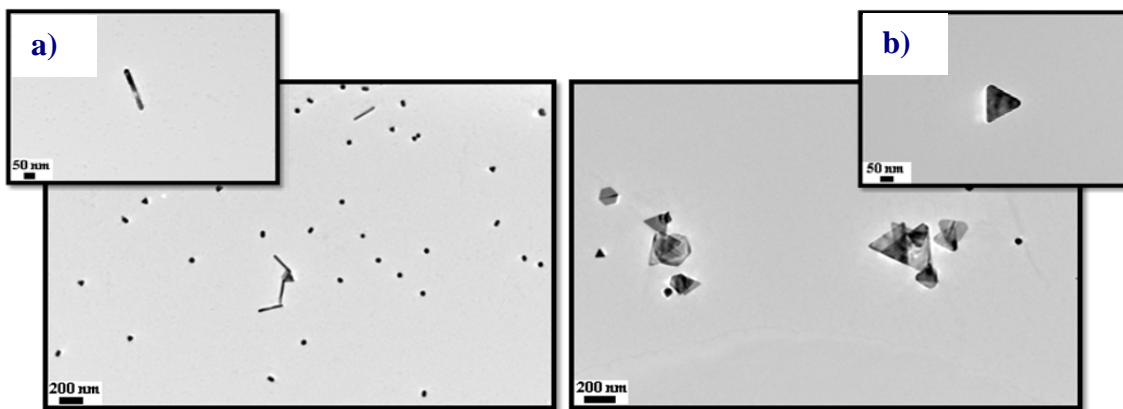

Figure 5. Au (a) nanorods (aspect ratio 10) and (b) nanoprisms (about 150 nm edge length). Scale bars are 50 nm (top) and 200 nm (bottom).

EDS, shown in figure 6, confirms the presence of Au in solution. Peaks indicating copper can be rejected due to the copper grid on which the samples were characterized.
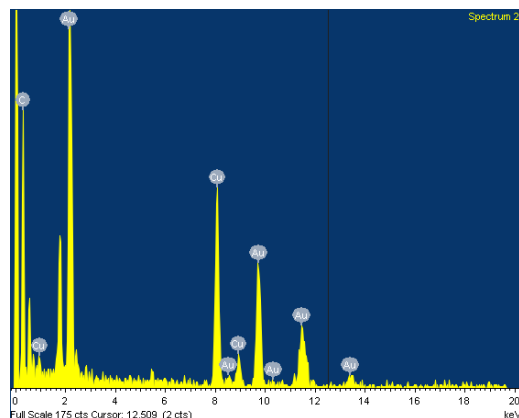

Figure 6. Energy dispersive spectroscopy of Au nanosphere
A sample. EDS for all other samples were similar.

Figure 7 shows the visible absorption spectra of the shape-controlled particles. As expected, a small red-shift in the absorbance peaks was noted as the size of the shape-controlled nanoparticles increased, with seeds being the smallest and nanoprisms the largest. No red-shift was seen from the spheres A to the spheres B solution because the size change of these particles was only a few nanometers. The second extended peak seen on the nanoprism spectra can be attributed to the larger nanoprisms in solution.
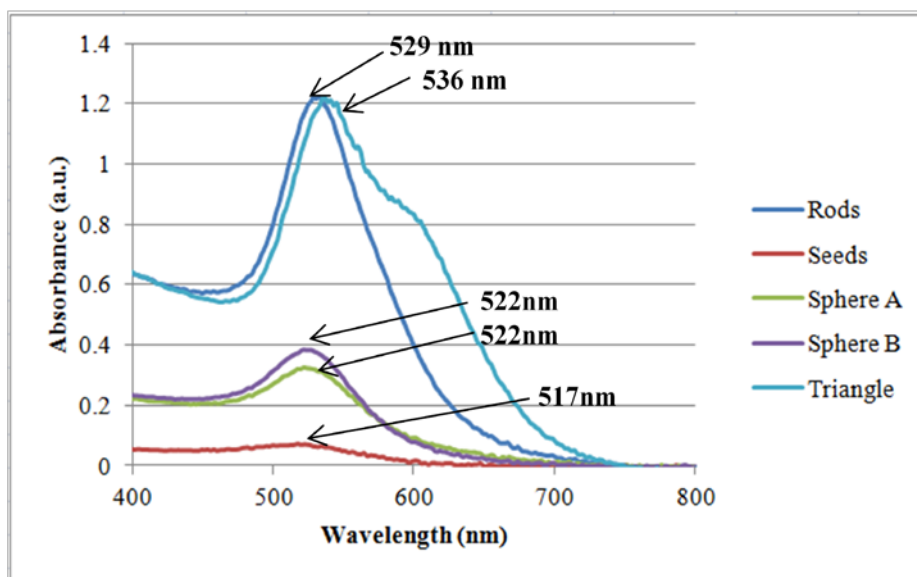

Figure 7. Visible absorption spectra for Au seeds, nanorods, nanoprisms, nanosphere A, and nanosphere B.

Dynamic light scattering was used to determine the zeta potential, or surface charge, of the shape-controlled particles. As is shown in table 1, all particles exhibited a positive surface charge

164

that increased with increasing particle size. The cationic surfactant, CTAB, used in the growth of these particles as a capping agent attributes to the positive charge. This confirms that as the particle size increases, more CTAB will bind to the Au crystal faces. If crystal growth occurs through the binding of CTAB bilayers to certain Au crystal faces, as stated in literature[28], these results suggest that the bilayer elongates as nanoparticle size increases. However, these surface charges are much greater than those usually observed for nanoparticles. Residual surfactant that was not completely purified out could have influenced these results, although centrifugation was repeated multiple times to remove excess surfactant.

Table 1. Zeta potential (surface charge) for shape-controlled
Au nanoparticles.

Sphere A	Sphere B	Rods	Triangles
57.87 mV	65.6 mV	98.46 mV	123.4 mV

4.   Summary and Conclusions

Three different Au nanoparticle (NP) shapes of nanorod, nanoprism, and nanosphere were successfully synthesized through a seed-mediated chemical method. It is interesting to note that that the nanoparticle shape can be completely changed from rod to triangular prism through simple addition of a trace amount of halide ion. It was also possible to control the yields of the NPs by controlling relative concentration of the starting materials. Future work will aim at improving the yield of the shape-controlled nanoparticles. In addition, future work will address removal of the positive surface charge of the particles through a ligand exchange. Finally, the effect of the shape, in addition to the size, on quantum tunneling effect will be investigated. The quantum tunneling effect will be investigated through scanning tunneling microscopy. In addition, nanolithography will be used to position these shape-controlled nanoparticles between two electrical leads to measure tunneling current. The results of the quantum tunneling effect will be reported in a subsequent communication.

5.   References

1. Mebrahtu, H. T.; Borzenets, I. V.; Liu, D. E.; Zheng, H.; Bomze, Y. V.; Smirnov, A. I.; Finkelstein, G. *Nature* **2012**, *488*, 61.

2. Busbee, B. D.; Obare, S. O.; Murphy, C. J. *Adv. Mater.* **2003**, *15* (5), 414.

3. Gao, J.; Bender, C. M.; Murphy, C. J. *Langmuir* **2003**, *19*, 9065–9070.

4. Gole, A.; Murphy, C. J. *Chem. Mater.* **2004**, *16*, 3633–3640.

5. Ha, T. H.; Koo, H.; Chung, B. H. *J. Phys. Chem. C* **2007**, *111*, 1123–1130.

6. Jana, N. R.; Gearheart, L.; Murphy, C. J. *Adv. Mater.* **2001**, *13*, 1389.

7. Jana, N. R.; Gearheart, L.; Murphy, C. J. *J. Phys. Chem. B* **2001**, *105*, 4065–4067.

8. Kim, F.; Song, J.; Yang, P. *J. Am. Chem. Soc.* **2002**, *124*, 14316–14317.

9. Liu, M.; Guyot-Sionnest, P. *J. Phys, Chem. B* **2005**, *109*, 22192–22200.

10. Nikoobakht, B.; El-Sayed, M. A. *Chem. Mater.* **2003**, *15*, 1956–1962.

11. Sau, T. K.; Murphy, C. J. *Langmuir* **2004**, *20*, 6414–6420.

12. Sau, T. K.; Murphy, C. J. *J. Am. Chem. Soc.* **2004**, *126*, 8648.

13. Millstone, J. E.; Métraux, Mirkin, C. A. *Adv. Funct. Mater.*, **16**, 1209–1214, 2006.

14. Millstone, J. E.; Hurst, S. J.; Métraux, G. S.; Cutler, J. I.; Mirkin, C. A. *Small* **2009**, *5* (6), 646–664.

15. Shankar, S. S.; Rai, A.; Ankamwar, B.; Singh, A.; Ahmad, A.; Sastry, M. *Nature Mater.* **2004**, *3*, 482.

16. Shankar, S. S.; Bhargava, S.; Sastry, M. *J. Nanosci. Nanotechnol.* **2005**, *5*, 1721–1727.

17. Xie, J.; Lee. J. Y.; Wang, D.I.C. *J. Phys. Chem. C.* **2007**, *111*, 10226–10232.

18. Jana, N. R.; Gearheart, L.; Murphy, C. J. *Chem. Mater.* **2001**, *13*, 2313–2322.

19. Jana, N. R.; Gearheart, L.; Murphy, C. J. *Langmuir* **2001**, *17*, 6782–6786.

20. Kim, F.; Connor, S.; Song, H.; Kuykendall, T.; Yang, P. Angew. *Chem. Int. Ed.* **2004**, *43*, 3673–3677.

21. Skrabalak, S. E., et al. *Acc. Chem. Res.* **2008**, *41* (12), 1587–1595.

22. Sun, Y., et al. *Science* **2002**, *298*, 2176–2179.

23. Murphy, C. J.; Sau, T. K.; Gole, A. M.; Orendorff, C. J.; Gao, J.; Gou, L.; Hunyadi, S. E.; Li, T. *J. Phys. Chem. B* **2005**, *109*, 13857–13870.

24. Tao, A. R.; Habas, S.; Yang, P. *Small* **2008**, *4* (3), 310–325.

25. Grzelczak, M.; Pérez-Juste, J.; Mulvaney, Liz-Marzán, L. M. *Chem. Soc. Rev.* **2008**, *37*, 1783–1791.

26. Dandekar, V.; Cramer, H.; Lee, E.; Griep, M.; Karna, S. *Chemical vs. Sonochemical Synthesis and Characterization of Silver, Gold, and Hybrid Nanoparticles*; ARL-TR-5764, U.S. Army Research Laboratory: Aberdeen Proving Ground, MD, 2011.

27. Millstone, J. E., Wei, W., Jones, M. R., Yoo, H., Mirkin, C. A., *Nano Letters* **2008**, *8* (8), 2526–2529.

28. Lofton, C., Sigmund, W., *Adv. Funct. Mater.* **2005**, *15*, 1197–1208.

INTENTIONALLY LEFT BLANK.

U.S. Army Research Laboratory
SUMMER RESEARCH TECHNICAL REPORT

Predicting Axonal Injury and Repair in the Brain Post Trauma: A pairing of Finite Element Methods with *in vivo* Imaging Techniques

ASHLEY EIDSMORE
MENTORS: AMY DAGRO AND JUSTIN MCKEE
WEAPONS AND MATERIALS RESEARCH DIRECTORATE
ABERDEEN PROVING GROUND, MD

Contents

List of Figures

List of Tables

Abstract

Finite element (FE) models are widely used in the biomechanics community, yet fail to accurately correlate mechanical loading with tissue response and multi-scale injury mechanisms. State-of-the-art FE models incorporate imaging techniques such as diffusion tensor imaging (DTI) to reconstruct neuronal fiber bundles in the brain. The benefit of incorporating fibers is twofold: first, the fiber directions enhance material models by including anisotropy in constitutive models. Secondly, they provide insight on the structural connectivity of the brain, which is fundamental for cognitive functionality. Current methods at the U.S. Army Research Laboratory (ARL) correlate strain resolved in fiber direction and empirical cellular death models to predict damage. These models lack a validated relationship between strain and cellular injury. Additionally, they do not account for cellular repair. In this study, we investigated relationships between DTI-acquired measurements of pre- and post-blast injured mice and axonal strain. In order to reach this goal, an FE model and a novel process to recreate the structural network of the mouse were created. Using discovered relations, this platform will allow prediction of damage and recovery to be integrated into computational simulations and help validate the corresponding human model.

Acknowledgments

Student Bio

Ashley Eidsmore is entering her senior year in the electrical engineering program at Purdue University. At Purdue, she is involved with the Purdue Neurotrauma Group, studying brain injury in athletes and is a founder for a small start-up specializing in sports telemetry systems. Her history with research laboratories started in early high school when she partook in the Science and Engineering Apprenticeship Program (SEAP) at the U.S. Medical Research Institute of Chemical Defense. There she was involved with research focused on neuronal degeneration due to chemical agents, histopathology studies, and the creation of a cavia porcellus brain atlas. She transitioned to the U.S. Army Research Laboratory (ARL) under the Oak Ridge Institute for Science and Education (ORISE) program in the summer of 2010. At ARL, she has received a pending patent for multimodal mobile methods and software used in the screening of mild Traumatic Brain Injury. After graduation, Ashley plans to attend graduate school for biomedical engineering with a focus in neural networks and signal processing.

1. Introduction/Background

Traumatic Brain Injury (TBI) has become a signature wound in Soldiers. In 2011, there were over 30,000 reported cases of TBI, with 23,633 of these cases being mild (*1*). At the U.S. Army Research Laboratory (ARL), helmets and systems to protect the Soldiers are developed, yet the underlying mechanism of tissue damage in the brain is not fully understood. Even more concerning is the inability to accurately detect mild Traumatic Brain Injury (mTBI) non-invasively, leaving many cases undiagnosed and untreated. Even when severe cases are diagnosed, the extent of the damage is not well-known and the possibility for cellular repair cannot be predicted. Knowing this, two main questions face researchers today: (1) How can mTBI be detected non-invasively? (2) Can the extent of damage be accurately predicted?

In late, much focus in the scientific community has been put towards finding a method to detect mTBI non-invasively. One method in particular includes the use of a magnetic resonance image (MRI)-based imaging technique called diffusion tensor imaging (DTI). This technique allows the direction that water molecules diffuse in the brain due to characteristic Brownian motion to be tracked using magnetic pulse sequences. The diffusion of these water molecules reveals details about tissue architecture, such as where neural fiber tracts (i.e., bundles of axons) reside (*21*). This is because in axon bundles, diffusion is restricted in the radial direction. These fiber tracts can then be reconstructed by analyzing the directional patterns seen in the returned diffusion tensors. The collection of these fiber tracts has been referred to as the tractography (*3*). Recent studies have compared tractography in normal and severely injured brains. A distinct study published in the Journal of Neurotrauma showed an apparent decrease in fiber density in the corpus callosum for afflicted individuals (*2*). Narrowing the focus down to each voxel in the image allows another measure to be obtained from DTIs, known as fractional anisotropy (FA), or the overall measure of diffusivity. FA is a ratio expressed as a value from 0 to 1, with complete isotropic diffusivity being 0 and complete anisotropic diffusivity being 1. This parameter attracts interest due to studies showing an apparent decrease in FA values in mildly injured brains compared to healthy adult brains (*4*). Unfortunately, the relationship between actual cellular death and decreased FA values has not yet been quantified.

In order to design better head protection for Soldiers, improved predictive models for brain injury need to be developed. At ARL, the Computational Injury Biomechanics Laboratory is incorporating DTI-extracted tractography into finite element (FE) simulations of blunt trauma and blast loading. The tractography informs elements of fiber direction to allow for anisotropy to be included in the constitutive model. The network, or connectome, as referred to in reference, is then formed and used to display injury calculations. Injury calculations are constructed from simulated strain resolved in fiber direction paired with cellular death models derived from post-mortem rat grey matter (*11*). The problem here is that since fiber tracts reside in white matter, the

cellular composition and response may differ. Current models also lack injury prediction for grey matter and degrade network edges in accordance to a binary fiber deletion approach. This approach provides a decent representation of current injury level, but lacks insight into the future compromise of intact fibers. Additionally, these studies do not account for cellular repair.

The goal of this work was three-fold: first, to develop a method that combines the mechanical responses seen in finite element simulations with fractional anisotropy values experimentally obtained; second, to develop a computational platform to replace cellular death models with FA measurements; and third, to provide a framework that can predict likely areas of axonal injury or repair in the brain following blast loading.

2. Experiment/Calculations

A combination of medical imaging techniques and software allowed for the construction of distinct finite element mouse models for structurally based network analysis. The central process is visualized in figure 1 and outlined in the following sections.
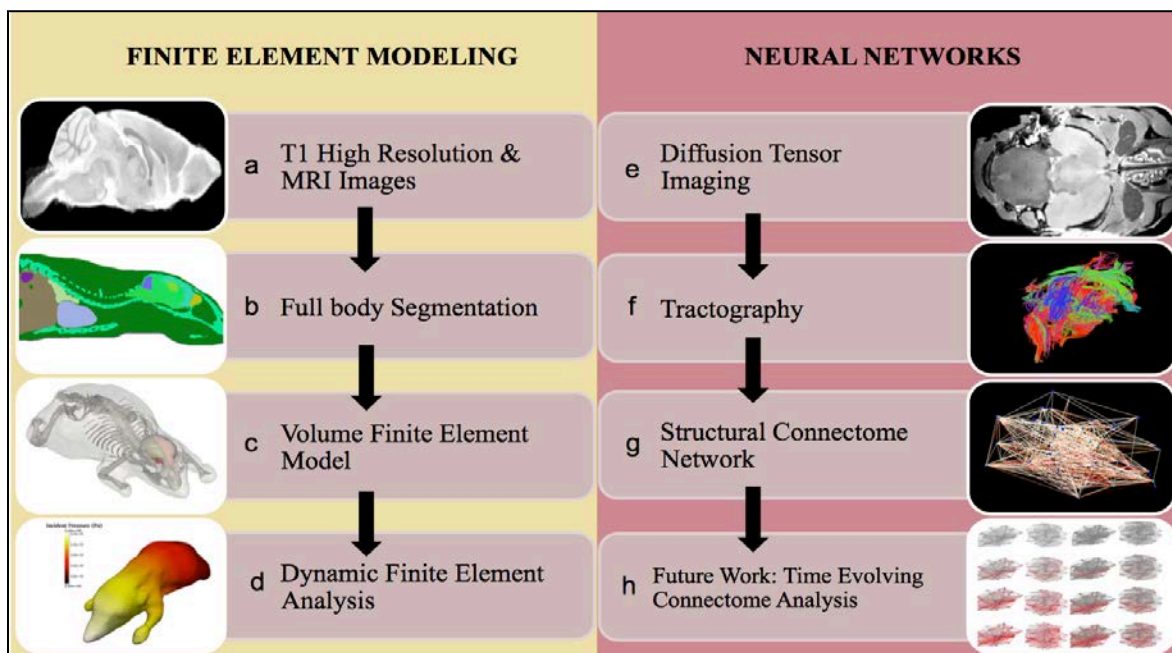

Figure 1. A flowchart of the process for creating the finite element model and structural network. (a) The T1 and MRI images are (b) segmented into different material components. The segmented geometry is then used to create (c) a finite element tetrahedral volume mesh. This volume mesh is used in (d) dynamic finite element simulations. (e) Diffusion tensor images are used to generate (f) fiber tractography used to inform the constitutive model. The tractography is also used to create (g) a network model of the brain that can (h) degrade to show injury.

2.1 Image Acquisition and Reconstruction

Unique mouse brains were obtained through use of medical imaging and software tools. Diffusion and T1-weighted magnetic resonance images were acquired and, with aid from the FMRIB Software Library, co-registered to corresponding b0 images to minimize blurring effects seen from interpolation. Fractional Anisotropy values for each voxel were calculated in Diffusion Toolkit. Axonal bundle fiber tracts were located by assuming the primary eigenvector of the diagonalized diffusion tensor represented the local fiber orientation. Fiber tracking was performed using modified Diffusion Tookit commands based on the Fiber Assignment by Continuous Tracking (FACT) method and brute-force fiber searching (*7, 8*). Fibers were filtered with a probabilistic white matter mask so as to eliminate noise (*10*). The fiber tracts were visualized in TrackVis and exported.

To create the structural network, T1 images were skull-stripped, registered, and parcellated into 78 anatomical regions of interest (ROI) based on a structural mouse brain atlas (*6*). Each fiber was then mapped to a starting and ending ROI. The structural network graph was then assembled and is composed of nodes representing the ROIs, connected by edges representing fiber pathways. The edges were weighted based on the number of fibers between two given ROIs.

2.2 Finite Element Modeling

Finite element simulations of the mouse were designed to mimic experimental conditions for ongoing shock tube blast impact tests at the University of Pennsylvania Molecular Neuroengineering lab. This work is funded through the Army Research Office.

In this study, individual-specific finite element models were generated from high resolution MRIs after overlapping, registering, and extracting geometries from the Digimouse: 3D Mouse Atlas (*9*) using the software Amira ®. The extracted geometries were then imported into meshing software, ANSYS ICEM CFD, to first, create a triangulated surface mesh, and secondly, generate a four-noded tetrahedron element volume mesh. To reduce the overall number of elements and, thus, decrease computational time, a meshing approach was adopted to create finer mesh elements near the rat brain and coarser mesh elements elsewhere. The volume mesh was segmented into five main regions that represent muscle, white matter in the brain, grey matter in the brain, cerebral spinal fluid, and bone.

The grey matter and cerebral spinal fluid are modeled as Mooney-Rivlin hyperelastic materials adopted from literature (*12–16*). The muscle and skull are modeled as linear elastic materials (*12, 13, 16, 17*). A transverse isotropic hyperelastic constitutive model (*12, 13, 15, 18, 19, 20*) is used for the white matter tissue. The material properties are expanded upon and summarized in table 1.

Table 1. Material properties.

(a) Isotropic Elastic material properties

Material	Young's modulus (MPa)	Poisson's Ratio
Skin/Muscles	10 MPa	0.45
Skull	600 MPa	0.229

(b) Hyperelastic Mooney-Rivlin material model properties

Material	Bulk Modulus	C10	C01	Poisson's Ratio
Grey Matter	2.3 GPa	1000 Pa	1000 Pa	0.49
CSF	2.1 GPa	200 Pa	200 Pa	0.5

(c) Transverse isotropic with Mooney-Rivlin matrix material model properties

Material	Bulk Modulus	Density	C10	C01	C3	Poisson's Ratio
White Matter	2.3 GPa	1.04 g/cm^3	1 kPa	1 kPa	5 kPa	0.5

To simulate the mechanical response to blast loading, a Lagrangian explicit dynamics code known as Presto was used. A pressure load resulted from a spherical explosive blast located 0.65 m zenith from the head, resulting in an incident peak pressure of 207 kPa applied to the skin. The pressure boundary conditions were based off of experimentally measured pressure-time curves and are listed in table 2. Displacements of the nodes from the neck down were fixed in all directions to replicate the body of the mouse being constrained. The finite element simulation computed time-evolving stress, and the mechanical strain resolved in the direction of axon fiber bundles. Output parameters were imported into either a python-based environment or MATLAB for post-processing.

Table 2. Pressure load parameters for explosive blast.

Burst Type	Spherical Free-Air
Range to target	0.65 m
Peak incident overpressure	207 kPA
Duration	0.6 ms

2.3 Coupling Simulation Results to Fa Values

Experimental data can be combined with the finite element simulations by mapping fibers to containing tetrahedral elements. Each fiber contains connected fiber points with spatial coordinates. To associate a fiber with elements, each element in the FE model was traversed for each fiber point in a fiber to determine whether or not it contained the given fiber point. The resulting matrix was comprised of rows associated with individual fibers and columns representing the elements the fiber was found in. The fiber points in each fiber also correspond to a voxel containing imaging data. This allowed certain elements to take on experimentally derived data values such as fractional anisotropy.

3. Results and Discussion

A finite element model for a mouse was created. The volume mesh contained 330,852 elements with an average quality of 0.7. The diffusion tensor imaging derived tractography contained 8,842 fiber tracts. Elements contained in parcellated sections of the brain were successfully mapped to structural fibers. Figure 2 shows the fibers crossing through the corpus callosum, and the connecting fibers between the corpus callosum and cerebral cortex.
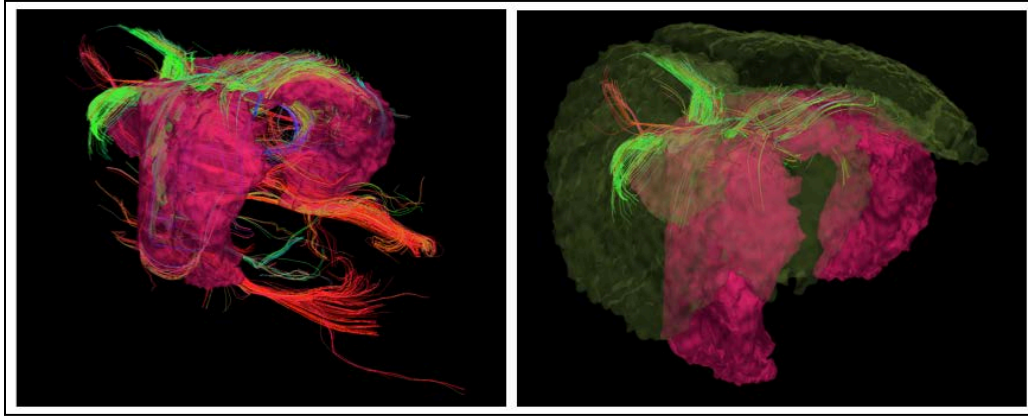

Figure 2. On the left, fibers crossing through the highlighted corpus callosum white matter region are shown. On the right, connecting fibers between the corpus callosum and cerebral cortex are shown.

A network model was created for the same mouse and consisted of 78 nodes and 468 edges. The network is shown in figure 3.
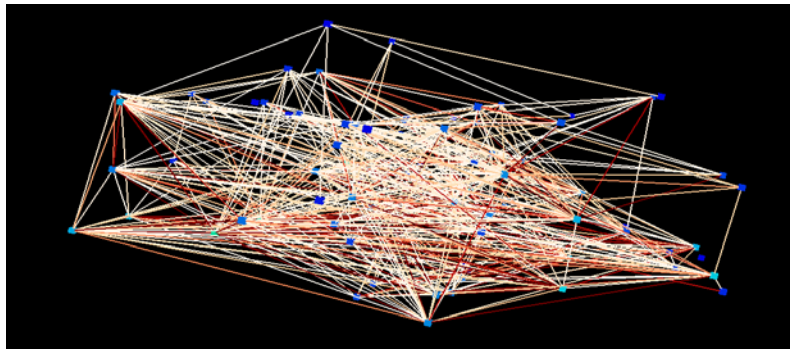
Figure 3. A network for the mouse brain contains nodes representing 78 regions of interest and 468 interconnecting edges. The shown network is weighted and colored according to the number of fibers between connecting regions.

The produced finite element model was tested in the blast simulation and saw a 207.8 kPa surface pressure on the top of the head at approximately 0.2 ms after the blast arrival time of 0.6 ms. Deformation was seen at the top of the head and continued down through the nose. Intracranial pressure was measured at the midbrain, corpus callosum, frontal cortex, and posterior brain. The first largest positive pressure of 164 kPA was reached at the corpus callosum, the closet region to impact, at approximately 0.7 ms. The computed pressure results are shown in figure 4.
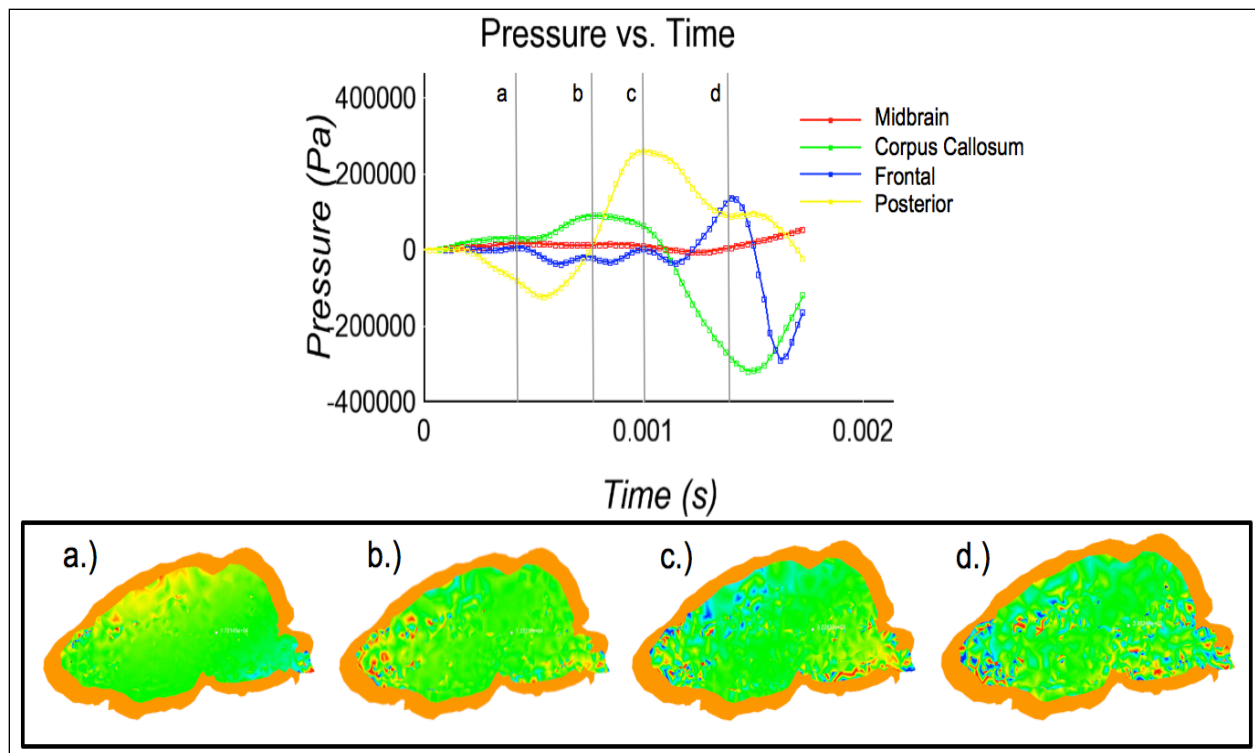
Figure 4. Pressure vs. Time is plotted in various intracranial regions. Cross sections of the brain are shown throughout.

The effective strain and strain rate were also obtained. A maximum strain of 33% was seen at the frontal cortex 2 s into the duration of the simulation. The majority of the strain rates oscillated below 10% effective strain. Figure 5 shows the effective strain measures obtained throughout the simulation.
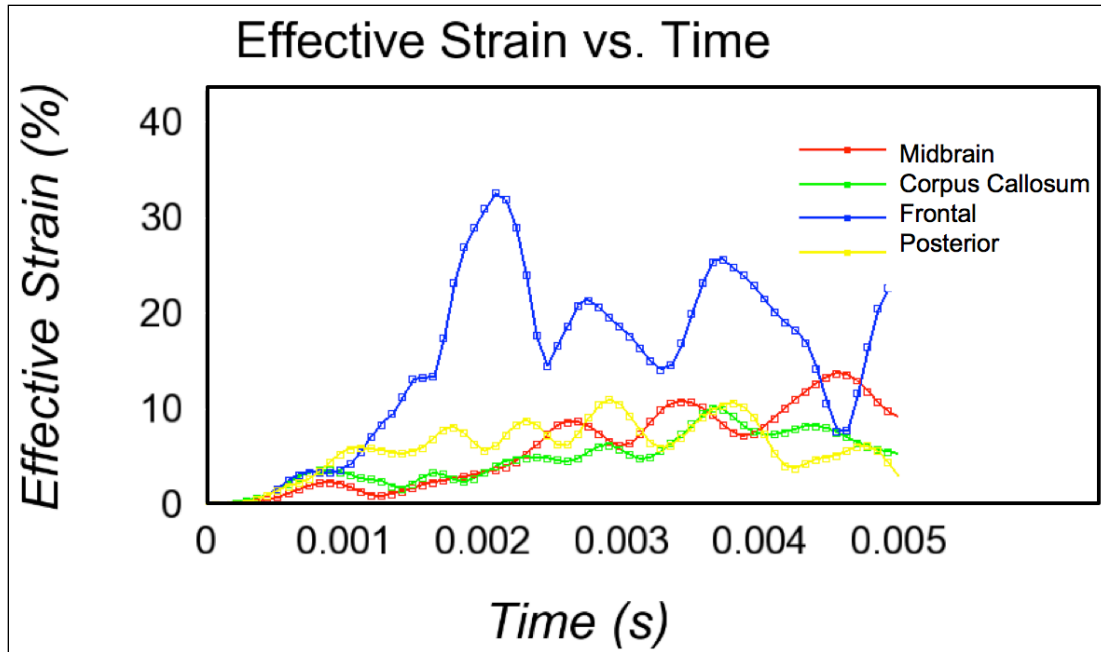
Figure 5. A plot of effective strain seen in brain regions throughout a 5 s blast simulation window.

3.1   Future Work

Experimental blast studies are still ongoing with our collaborators at the University of Pennsylvania. The extended duration of this process delays post-processing of the time-evolving injury networks. The sections following describe the general processing that will be done once experimental data is finalized and obtained.

Results from blast FE simulations will give parameters that we will correlate to fractional anisotropy from the DTI mouse experiments [#]. Once this relationship is discovered, the change in FA of a given fiber can be predicted based on strains and pressure in its containing elements. Note that this method accounts for the length of the fiber and the ratio of afflicted elements by allowing fibers to contain multiple fiber points in the same element.

An injured network model will be created after weighting both nodes and edges. The nodes representing each ROI will be weighted based on the averaged injury weight given to all fibers passing through the current ROI. The edges are weighted based on the averaged injury weight of all fibers passing through both connected ROIs. To incorporate repair into the model, DTIs will be taken post-injury of the mice throughout a one-week period. Clustering algorithms will be used to find relations between regional density, changes in FA, and surrounding fiber tract orientations. Fiber regeneration will favor the hierarchy or most "social" regions of the network. These social regions will correspond to nodes in the network that have low injury ratings. In this model, structural reestablishment would decrease injury weightings, but it should be noted that this repair is only structurally based and does not imply similar changes in functional health.

We hope that these processing methods will yield a more quantifiable and descriptive measure of axonal injury that can be incorporated into future predictive models. Future efforts to link a functional network representation to the structural aspect should also be pursued. By incorporating functional and structural networks, a robust predictive model is developed. This combined network model has the potential of being incorporated into helmet testing being done at ARL.

4. Conclusions

In the first part of the study, a procedure to create individualized finite element models for mice was developed. These FE models used the directionality of fiber bundle tracts reconstructed from diffusion tensor images to add anisotropy to their constitutive white matter material properties. Finite element simulations were then performed based on loading boundary conditions obtained from ongoing collaborative research.

The second part of the study formed a coupled computational method to study the relation of changes in experimentally obtained fractional anisotropy (FA) values to mechanical properties such as strain, strain rate, and pressure. This was achieved through the creation of a structural network obtained from the reconstructed tractography that was then mapped to corresponding elements in the simulation.

The concluding section mentioned ongoing experiments might provide possible data to show blast loading effects and network injury or repair over time. A method to replace cellular death models with an experimentally derived relationship involving changes in FA was proposed. This relationship could only be found with *in vivo* imaging in animal models coupled with structural neural network models. Once the functional relationship is found, axonal injury may be predicted and integrated into computational simulations. Following, a framework to predict likely areas of axonal repair was described. Interestingly, this repair model is based on the newly proposed injury weighting method.

The combination of finite element and network modeling, as well as medical imaging, can help to derive a more quantifiable measure of axonal damage that has the potential of being incorporated into future predictive models. These predictive models have direct application to the Army since they can be integrated into computational helmet tests.

5. References

1. Armed Forces Health Surveillance Center (AFHSC), Defense Medical Surveillance System (DMSS) and Theater Medical Data Store (TMDS), 2011.

2. Xu, J.; Rasmussen, I.; Lagopoulos, J.; Haberg, A. Diffuse Axonal Injury in Severe Traumatic Brain Injury Visualized Using High-Resolution Diffusion Tensor Imaging.

3. Mori, S.; Zhang, J. Principles of Diffusion Tensor Imaging and its Applications to Basic Neuroscience Research. *Neuron* **2006**, 527–39.

4. Davenport, N. D.; Lim, K. O.; Armstrong, M. T.; Sponheim, S. R. Diffuse and Spatially Variable White Matter Disruptions are Associated with Blast-related Mild Traumatic Brain Injury. *NeuroImage* **2011**.

5. Mac Donald, C. L.; Dikranian, K.; Song, S. K.; Bayly, P.V.; Holtzman, D. M.; Brody, D. L Detection of Traumatic Axonal Injury with Diffusion Tensor Imaging.

6. Bai, J.; Trinh, H.; Chuang, K. H.; Qiu, A. Atlas-based Automatic Mouse Brain Image Segmentation Revisited: Improvement Through Image Registration. Submitted to NeuroImage on 20 July 2010.

7. Mori, S.; Crain, B. J.; Chacko, V. P.; van Zijl, P.C.M. Three dimensional Tracking of Axonal Projections in the Brain by Magnetic Resonance Imaging. *Ann Neurol* **1999**, *45*, 265–269.

8. Conturo, T. E.; Lori, N. F.; Cull, T. S.; Akbudak, E.; Snyder, A. Z.; Shimony, J. S.; McKinstry, R. C.; Burton, H.; Raichle, M. E. Tracking Neuronal Fiber Pathways in the living Human Brain. *Proc Natl Acad Sci USA* **1999**, *96*, 10422–10427.

9. Dogdas, B.; Stout, D.; Chatziioannou, A.; Leahy, R. M. Digimouse: A 3D Whole Body Mouse Atlas from CT and Cryosection Data. *Phys. Med. Bio* **2007**, *52*, 577–587.

10. Jiang, Y.; Johnson, G. A. Microscopic Diffusion Tensor Imaging of the Mouse Brain. *Neuroimage* **2009**, *50*, 465–471.

11. Morrison III, B.; Cullen, D. K.; LaPlaca, M. In Vitro Models for Biomechanical Studies of Neural Tissues, In: Bilston LE, editor, Neural Tissue Biomechanics, Springer Berlin Heidelberg, volume 3 of Studies in Mechanobiology. *Tissue Engineering and Biomaterials*, pp. 247–285, 2011.

12. Shafieian, M.; Bao, J.; Darvish, K. Mechanical properties of brain tissue in strain rates of blast injury, In: Bioengineering Conference (NEBEC). *2011 IEEE 37th Annual Northeast*, pp. 1–2, 2011

13. Brands, D.W.A.; Peters, G.W.M.; Bovendeerd, P.H.M. Design and Numerical Implementation of a 3-d Non-linear Viscoelastic Constitutive Model for Brain Tissue During Impact. *Journal of Biomechanics* **2004**, *37*, 127–134.

14. Willinger, R.; Kang, H. S.; Diaw, B. Three-dimensional Human Head Finite-element Model Validation Against Two Experimental Impacts. *Annals of Biomedical Engineering* **1999**, *27*, 403–410.

15. Wright, R. M.; Ramesh, K. T. An Axonal Strain Injury Criterion for Traumatic Brain Injury. *Biomechanics and Modeling in Mechanobiology* **2011**, 1–16.

16. Kleiven, S.; Hardy, W. N. Correlation of an FE Model of the Human Head with Local Brain Motion-consequences for Injury Prediction. *Stapp Car Crash Journal* **2002**, *46*, 123–144.

17. Chen, Y., Ostoja-Starzewski, M., MRI-based Finite Element Modeling of Head Trauma: Spherically Focusing Shear Waves. *Acta Mechanica* **2010**, *213*, 155–167.

18. Horgan, T. J.; Gilchrist, M. D. The Creation of Three-dimensional Finite Element Models for Simulating Head Impact Biomechanics. *International Journal of Crashworthiness* **2003**, *8*, 353–366.

19. Harrigan, T. P.; Roberts, J.; Ward, E. E.; Merkle, A. C. Correlating Tissue Response with Anatomical Location of mTBI Using a Human Head Finite Element Model Under Simulated Blast Conditions, In: Herold K, Vossoughi J, Bentley WE, editors, 26th Southern Biomedical Engineering Conference 2010 April 30 - May 2, 2010 College Park, Maryland, USA. Springer, IFMBE Proceedings, pp. 18–21, 2010.

20. Arbogast, K. B.; Margulies, S. S. A Fiber-reinforced Composite Model of the Viscoelastic Behavior of the Brainstem in Shear. *Journal of Biomechanics* **1999**, *32*, 865–870.

21. Hagmann, P.; Jonasson, L.; Maeder, P.; Thiran, J. P.; Wedeen, V. J., et al. Understanding Diffusion MR Imaging Techniques: From Scalar Diffusion-weighted Imaging to Diffusion Tensor Imaging and Beyond1. *Radiographics* **2006**, *26*, S205–S223.

U.S. Army Research Laboratory
SUMMER RESEARCH TECHNICAL REPORT

Simulation of Steady Plastic Waves with Anisotropic Material Response

JEFFREY T. LLOYD
MENTOR: JOHN D. CLAYTON
WEAPONS AND MATERIALS RESEARCH DIRECTORATE
ABERDEEN PROVING GROUND, MARYLAND

Contents

List of Figures

Abstract

Steady plastic wave formulations have been successfully used to simulate the elastic-plastic response of materials in various loading conditions; however, these formulations all assume an isotropic plastic material response. Because slip system level kinematics govern the viscoplastic shock behavior—but cannot be modeled using an isotropic plastic formulation—an anisotropic plastic formulation is created, which admits the response of individual slip system kinematics, yet retains the computational efficiency inherent in steady plastic wave analyses. A thermodynamically consistent formulation that employs second- and third-order elastic constants is presented, which can be applied to any slip system level constitutive hardening relation. A physically based slip system level constitutive equation is applied to weak shock-loading of single crystal Al, and compared to both experimental and finite element simulations that use the same loading conditions. Individual slip system nucleation, multiplication, trapping, and annihilation rates are extracted, and used to interpret the primary mechanisms that govern the single crystal response at different pressures and orientations. A general formulation for simulation of polycrystals is then presented in the context of single-crystal kinematics, which is to be used in future work to predict the weak shock response of annealed and pre-textured polycrystals.

Acknowledgments

Student Bio

Jeff Lloyd is a fourth-year Ph.D. student in mechanical engineering at Georgia Institute of Technology, the same institution where he earned his Bachelor's degree (2008) and Master's Degree (2010), both in mechanical engineering. Although a Mechanical Engineer in name, Jeff's past and current research has focused on computational mechanics of materials. Under a National Science Foundation (NSF) GRFP fellowship for his first three years of research, Jeff focused on crystal plasticity and multi-scaling modeling of fracture. After receiving the SMART Fellowship in 2010, Jeff entered into the world of high strain rates, and plans to make a career of it. Upon getting married this fall and finishing his Ph.D. next year, Jeff hopes to continue his work on modeling shock behavior of materials at multiple length scales at ARL, and apply the tools he has developed towards the problem of computational materials design.

1. Introduction/Background

The analytical and numerical treatment of wave propagation in solids is a tool that has been widely used in armor design. Accurate prediction of the shock response of different materials is used to optimize armor performance against specific threats. Therefore, it is paramount to understand the shock response of materials to efficiently and rapidly design armor.

The high strain rate and shock response of metals has received widespread attention in the form of both theoretical and experimental development. Kolsky bars have been used to characterize metals' response at large strains, high strain rates, and elevated temperatures, under the action of a homogeneous uniaxial and biaxial stress. The shock response of metals in terms of particle velocity and shockwave relations has been measured for most materials using plate impact experiments (*1*). These experiments can also give shock wave velocities by using Velocity Interferometer System for Any Reflector (VISAR), which gives information about how the shock evolves over time, including the spall response of the material. Information from high strain rate and shock experiments is used to inform, develop, and validate high strain rate constitutive models.

Because of the computational demands associated with modeling high strain rate behavior, constitutive equation development has historically focused on modeling macroscopically observed effects from high strain rate Kolsky bar tests and plate impact shock experiments. Most models implemented into production codes consider the materials response as a state function of macroscopically measurable variables, whose values are known from experiments (*2–6*). Because of their empirical nature, the ability of these models to predict behavior outside of the specific conditions in the experiments used to determine their parameters is an exercise in extrapolation, and not prediction.

Models aimed at predicting material behavior have focused on the physics of the shock front, but have been implemented into finite element codes using artificial viscosity to alleviate numerical instability and make up for a lack of underlying dissipative physics. To get around using this artificial viscosity and model the physics of the shock front without artificial dissipation, a steady plastic wave formulation has been developed, which considers the behavior of a plastic wave moving at constant velocity. First formulated by Taylor (*7*), the steady plastic wave formulation has received attention due to its simplicity and ability to model experimentally observed phenomena. Notable advances include Clifton's use of an elastic-plastic decomposition of the deformation gradient with finite deformation and third-order elastic constants (*8*), as well as physically based constitutive relations for dislocation nucleation rates and dislocation velocity by Austin and McDowell (*9*). These formulations, however, only admit isotropic elastic and plastic material response, and are, therefore, unable to predict the response of single crystals (excluding

191

symmetric orientations) and materials with anisotropic plastic response such as textured polycrystals.

Because the shock response is intimately tied to the material's fracture behavior (*10*), it is of utmost importance to characterize the physics of the shock response in single crystals, annealed polycrystals, and textured polycrystals. In the following sections, a steady plastic wave formulation for finite deformation and anisotropic material response will be derived.

2. Experiment/Calculations

The primary assumption in the steady plastic wave analysis is that the material undergoes uniaxial compression with a deformation gradient tensor of the form

$$
F = \begin{bmatrix} \lambda & 0 & 0 \\ 0 & 1 & 0 \\ 0 & 0 & 1 \end{bmatrix} = \begin{bmatrix} 1+\xi & 0 & 0 \\ 0 & 1 & 0 \\ 0 & 0 & 1 \end{bmatrix},
$$

(1)

where λ is the longitudinal stretch and ξ is the extent of compression. The validity of this assumption is undocumented in this work; however, it holds for highly symmetric crystal structures such as FCC. Quantifying the extent to which the difference between this analysis and general analysis lowers the symmetry BCC and HCP crystals is a goal of future work.

Using the uniaxial compression form of *F* given previously, all of the thermo-mechanical properties can be calculated by considering an energy function of the form

$$
\Psi_0 = \bar{\Psi}_0 + \bar{C}_{\alpha\beta} E^E_{\alpha\beta} + \frac{1}{2!} \bar{C}_{\alpha\beta\gamma\delta} E^E_{\alpha\beta} E^E_{\gamma\delta} + \frac{1}{3!} \bar{C}_{\alpha\beta\gamma\delta\kappa\lambda} E^E_{\alpha\beta} E^E_{\gamma\delta} E^E_{\kappa\lambda} - \bar{\beta}_{\alpha\beta} E^E_{\alpha\beta} \Delta\theta
$$

$$
- \frac{1}{2!} \bar{\beta}_{\alpha\beta\gamma\delta} E^E_{\alpha\beta} E^E_{\gamma\delta} \Delta\theta + y(\theta),
$$

(2)

where a line over a stiffness tensor indicates isothermal constants evaluated about some reference state. For example, the Second Piola Kirchhoff stress measured in the plastically deformed, but unrotated, frame is

$$
\Sigma_{\alpha\beta} = \frac{\partial \Psi_0}{\partial E^E_{\alpha\beta}} = \bar{C}_{\alpha\beta\gamma\delta} E^E_{\gamma\delta} + \frac{1}{2} \bar{C}_{\alpha\beta\gamma\delta\kappa\lambda} E^E_{\gamma\delta} E^E_{\kappa\lambda} - \bar{\beta}_{\alpha\beta} \Delta\theta - \bar{\beta}_{\alpha\beta\gamma\delta} E^E_{\gamma\delta} \Delta\theta .
$$

(3)

Using these definitions, the equations of motion for the steady plastic wave analysis, assuming some constant plastic wave speed *D* can be found, are summarized in figure 1.

As seen in figure 1 under box 4, the wave problem is transformed from a partial differential equation (PDE) in space *X* and time *t* to an ordinary differential equation (ODE) in some new

192

wave coordinates *Y*. The problem is transformed by converting the governing equations for momentum and compatibility, from their space and time form, to the form that depends only on the moving wave coordinates *Y*. This transformation is schematically shown in figure 2. The wave speed *D* is dictated by the peak shock stress, and can be calculated by combining the Rayleigh line equation with the particle-velocity relation from shock literature.

Figure 1. Equations and associated calculation steps for steady plastic wave analysis of anisotropic materials.
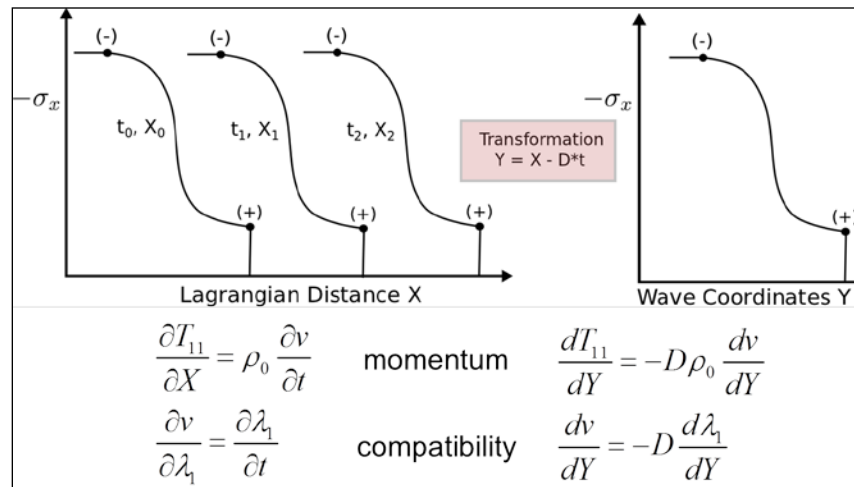

Figure 2. Conversion of PDE to ODE by transformation to moving coordinate system *Y*.

Because most of the anisotropic plane wave calculations are concerned with the thermodynamics and kinematics of the plane wave assumption, the constitutive model only enters through the definition of the average dislocation velocity and the dislocation density evolution rates.

The average dislocation velocity on each slip system is modeled after the thermodynamics of dislocations thermally activating past obstacles and dislocations entering the drag-dominated regime governed by viscous damping, and then, finally, by the relativistic constraints of dislocation motion. This model, which has been used successfully by other authors to describe macroscopic dislocation velocity (*8, 9, 11*), represents the physics of dislocation motion. The average dislocation velocity relation that coincides with this description is given by the following equation, and schematically shown in figure 3.

$$\overline{v}^{\alpha} = \frac{c_S h_c^{\alpha} z_c}{\left\langle h_c^{\alpha} \exp\left\{\Delta G^{\alpha} / k_B \theta\right\} - \alpha_c \right\rangle + z_c} \operatorname{sgn}\left(\tau^{\alpha}\right) \quad \text{if} \quad \left|\tau^{\alpha}\right| > \tau_{\mu}$$

$$\overline{v}^{\alpha} = 0 \qquad\qquad\qquad\qquad\qquad\qquad\qquad \text{otherwise} \tag{4}$$
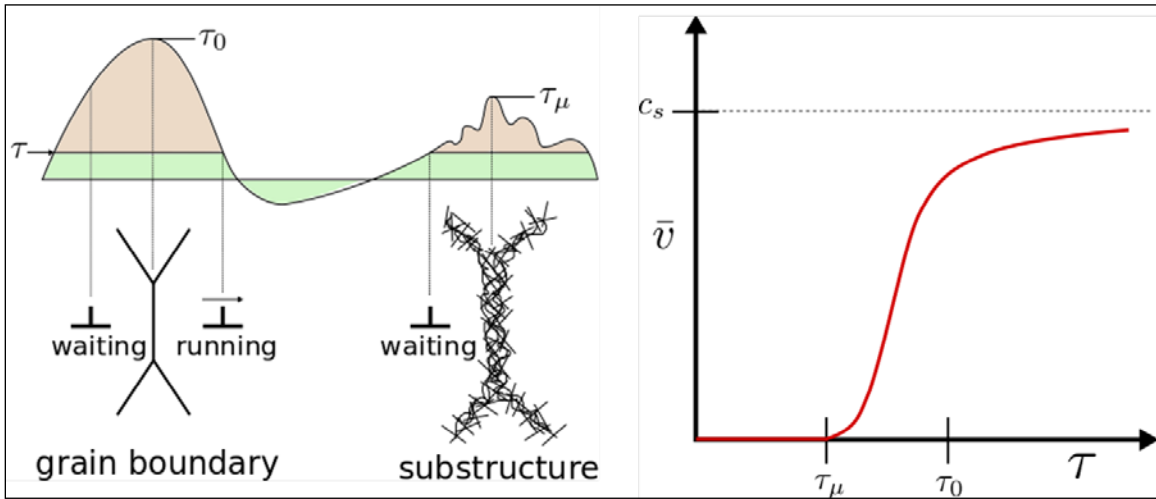
Figure 3. Dislocations thermally activating over obstacles (left), and the associated average velocity as a function of applied resolved shear stress (right). The orange area under the curve is the activation enthalpy associated with the barrier minus the energy associated with the applied stress.

Dislocation density rates are governed by the total contribution to mobile and immobile dislocation populations, which come from the nucleation, multiplication, annihilation, and trapping of dislocations.

$$\dot{N}_m^{\alpha} = \dot{N}_{het}^{\alpha} + \dot{N}_{mult}^{\alpha} - \dot{N}_{ann}^{\alpha} - \dot{N}_{trap}^{\alpha}$$

$$\dot{N}_{im}^{\alpha} = \dot{N}_{trap}^{\alpha} \tag{5}$$

194

The evolution rates for the different dislocation density mechanisms are governed by physical mechanisms that have been identified to contribute to mobile and immobile dislocation densities (*9, 12, 13*), and are schematically shown with their associated equations in figure 4.
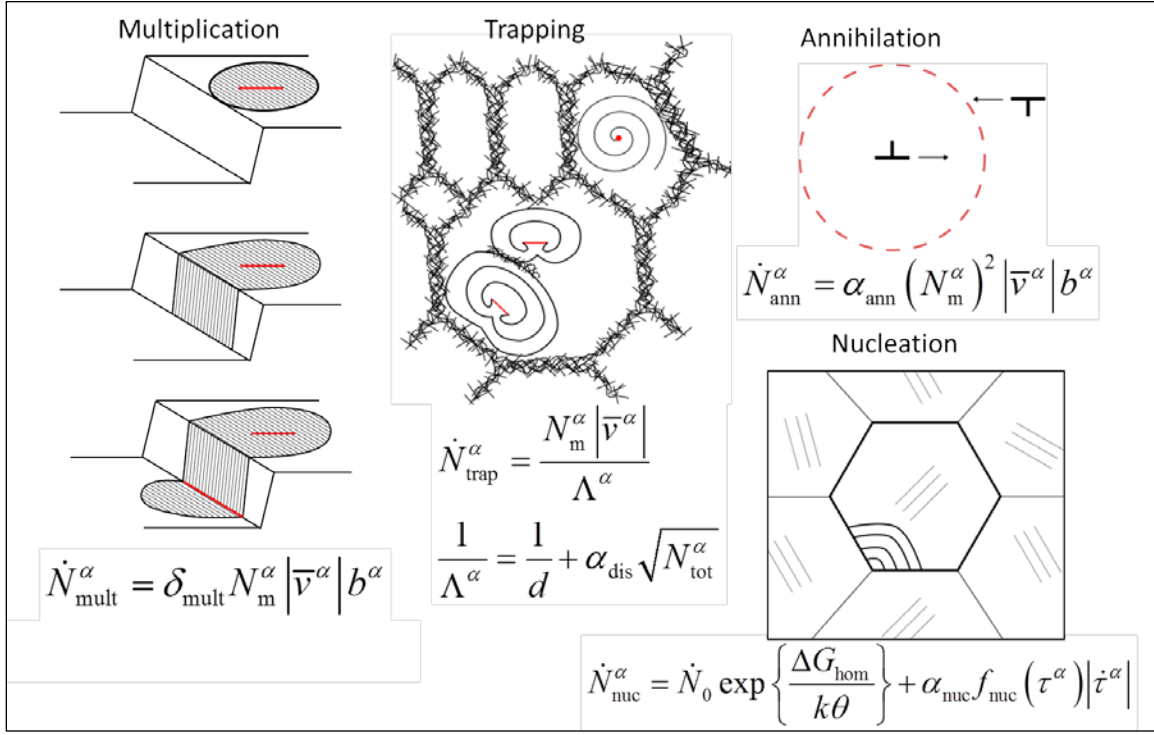

Multiplication

$$\dot{N}^\alpha_{mult} = \delta_{mult} N^\alpha_m \left| \overline{v}^\alpha \right| b^\alpha$$

Trapping

$$\dot{N}^\alpha_{trap} = \frac{N^\alpha_m \left| \overline{v}^\alpha \right|}{\Lambda^\alpha}$$

$$\frac{1}{\Lambda^\alpha} = \frac{1}{d} + \alpha_{dis} \sqrt{N^\alpha_{tot}}$$

Annihilation

$$\dot{N}^\alpha_{ann} = \alpha_{ann} \left(N^\alpha_m \right)^2 \left| \overline{v}^\alpha \right| b^\alpha$$

Nucleation

$$\dot{N}^\alpha_{nuc} = \dot{N}_0 \exp\left\{ \frac{\Delta G_{hom}}{k\theta} \right\} + \alpha_{nuc} f_{nuc} \left(\tau^\alpha \right) \left| \dot{\tau}^\alpha \right|$$

Figure 4. Schematic and associated equations that give dislocation nucleation, multiplication, annihilation, and trapping rates.

3.   Results and Discussion

Using the theoretical development given for the anisotropic plane wave formulation, a code has been developed that solves the plane wave ODE as a function of steady plastic wave coordinates *Y*. These coordinates can also be transformed to coordinates fixed in space *X* (Lagrangian description) or time *t* (temporal description).

Shock simulations were performed in Al single crystals, where the shock was applied in the [100] direction of a [100]-oriented single crystal. Constants for the thermo-mechanical part of the formulation were extracted from literature (*14,15*) and particle-velocity shock wave equations were used from Marsh (*1*). The results are shown in figure 5, where the experimental Hugoniot curve is based on particle-velocity relations, and third-order elastic constants were adjusted for a best fit to the Hugoniot data. As is seen in figure 5, the plane wave formulation sufficiently resolves the rise of the shock for a variety of shock strengths, because it is integrating solely over the shockwave, and not over the entire wave that varies in space and time.
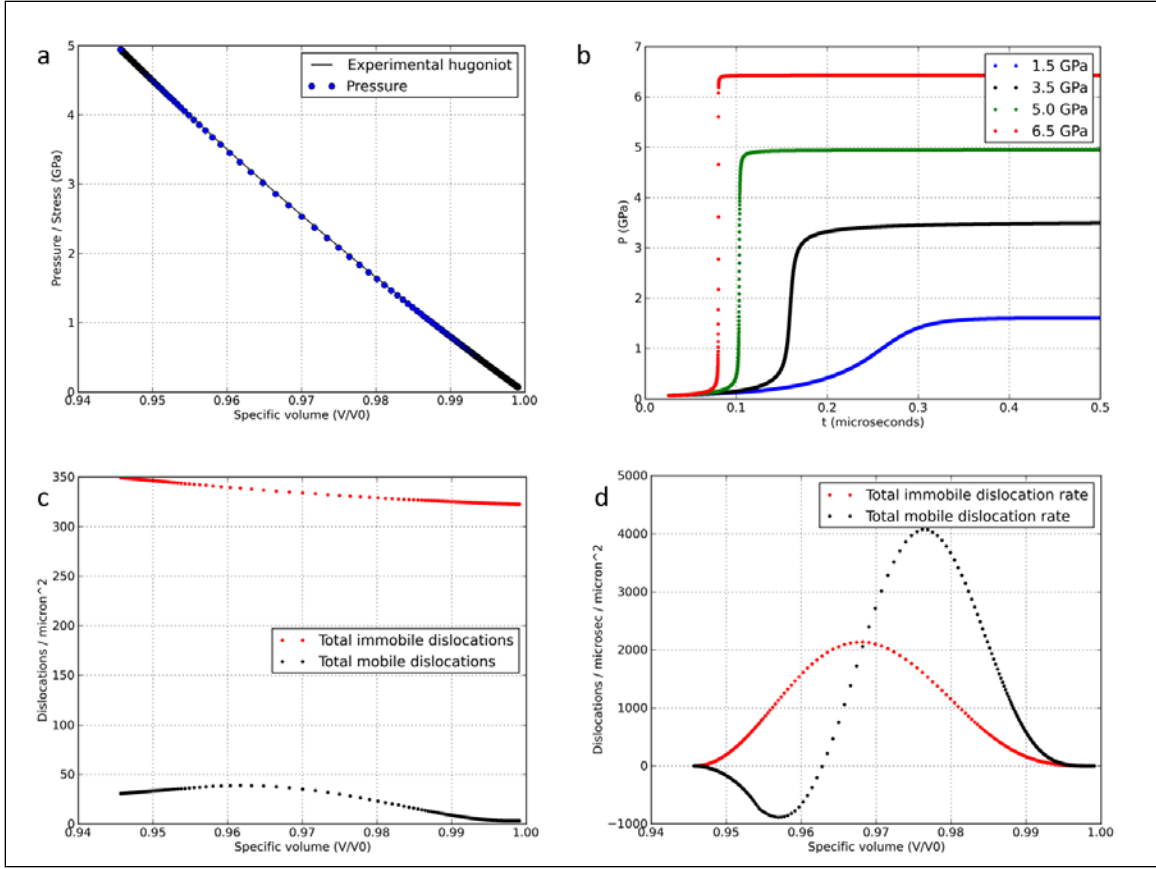
Figure 5. (a) Hugoniot relation compared to formulation for 5 GPa shock, (b) Pressure-time relation for different strength shocks showing shock behavior dependency on peak pressure, (c) total dislocation densities as a function of specific volume for 5 GPa shock, and (d) total dislocation density rates as a function of specific volume for 5 GPa shock.

As seen in figure 5(b), the peak stress influences the rise time and character of the shockwave, as shown by Swegle and Grady (*16*). In this formulation, this dissipation-induced shock width dependence on peak stress is governed by dislocation density rates and dislocation velocity relations, and not by an artificial viscosity. Also apparent from figures 5(c) and 5(d) is that since sufficiently many points are used to resolve the shock width, detailed information can be extracted concerning dislocation densities and dislocation density rates on individual slip systems, which was previously unobtainable in finite element and finite difference formulations due to computational cost, as well as isotropic plane wave formulations due to their isotropic assumptions. Finally, it should be noted that these simulations took approximately 1 min on a 3.0 GHz processor, which is multiple orders of magnitude faster than finite element and finite difference formulations that employ an artificial viscosity.

4. Summary and Conclusions

The steady plastic wave formulation allows for materials with non-symmetric plastic response to be modeled under uniaxial compression at high rates. The computational speedup gained by integrating the wave equation over the wave coordinate Y, instead of space and time, gives significant computational speedup and increased resolution of the viscoplastic deformation that governs the shock process. The constitutive equations developed herein are based on the physics of dislocation glide and dislocation density rates, which gives the model a predictive nature, instead of a prescriptive nature inherent in phenomenological models.

Significant work needs to be done to characterize the effectiveness of this formulation to predict shock behavior and provide insight to the mechanisms governing shock behavior at the single crystal level; however, this work presents a significant step towards this goal.

5. References

1. Marsh, S. P. *LASL Shock Hugoniot Data*; University of California Press, Berkeley, CA, 1980.

2. Johnson, G. R.; Cook, W. H. A Constitutive Model and Data for Metals Subjected to Large Strains, High Strain Rates and High Temperatures. In *Proceedings of the 7th International Symposium on Ballistics*, 541–547, 1983.

3. Johnson, G. R.; Cook, W.H. Fracture Characteristics of Three Metals Subjected to Various Strains, Strain Rates, Temperatures and Pressures. *Engineering Fracture Mechanics* **1985**, *21*, 31–48.

4. Steinberg, D. J.; Cochran, S. G.; Guinan, M. W. A Constitutive Model for Metals Applicable at High-strain Rate. *Journal of Applied Physics* **1980**, *51*, 1498–1504.

5. Steinberg, D. J.; Lund, C. M. A Constitutive Model for Strain Rates from 10^{-4} to 10^{6} s^{-1}. *Journal of Applied Physics* **1989**, *65*, 1528–1533.

6. Preston, D. L.; Tonks, D. L.; Wallace, D. C. Model of Plastic Deformation for Extreme Loading Conditions. *Journal of Applied Physics* **2003**, *93*, 211–220.

7. Taylor, G. The Use of Flat-Ended Projectiles for Determining Dynamic Yield Stress. I. Theoretical Considerations. *Proceedings of the Royal Society of London. Series A, Mathematical and Physical Sciences* **1948**, *194*, 289–299.

8. Clifton, R. J. On the Analysis of Elastic/Visco-Plastic Waves of Finite Uniaxial Strain. In *Shock Waves and the Mechanical Properties of Solids*, Eds. Burke J.J. and Weiss, V., 73-116. Syracuse University Press, Syracture, NY, 1971.

9. Austin, R. A.; McDowell, D. L. A Dislocation-based Constitutive Model for Viscoplastic Deformation of FCC Metals at Very High Strain Rates. *International Journal of Plasticity* **2011**, *27*, 1–24.

10. Williams, C.; Ramesh, K. T.; Dandekar, D. P. Spall Response of 1100-O Aluminum. *Journal of Applied Physics* **2012**, *111*, 123528.

11. Kocks, U. F.; Argon, A. S.; Ashby, M. F. Thermodynamics and Kinetics of Slip. *Progress in Materials Science* **1975**, *19*, 1–281.

12. Hirth, J. P.; Lothe, J. *Theory of Dislocations*; Wiley Press, New York, NY, 1982.

13. Hull, D.; Bacon, D. J. *Introduction to Dislocations*; Butterworth-Heinemann, Kidlington, Oxford, 2001.

14. Thomas, J. F. Third-Order Elastic Constants of Aluminum. *Physical Review* **1968**, *175*, 955–962.

15. Wang, K.; Reeber, R. The Perfect Crystal, Thermal Vacancies, and the Thermal Expansion Coefficient of Aluminum. *Philosophical Magazine A* **2000**, *80*, 1629-1643.

INTENTIONALLY LEFT BLANK.

INTENTIONALLY LEFT BLANK.